LBL-31541

Lawrence Berkeley Laboratory

UNIVERSITY OF CALIFORNIA

Materials & Chemical Sciences Division

A Surface Science Investigation of Silicon Carbide: Oxidation, Crystal Growth and Surface Structural Analysis

J.M. Powers
(Ph.D. Thesis)

November 1991

U. C. Lawrence Berkeley Laboratory
Library, Berkeley

FOR REFERENCE

Not to be taken from this room

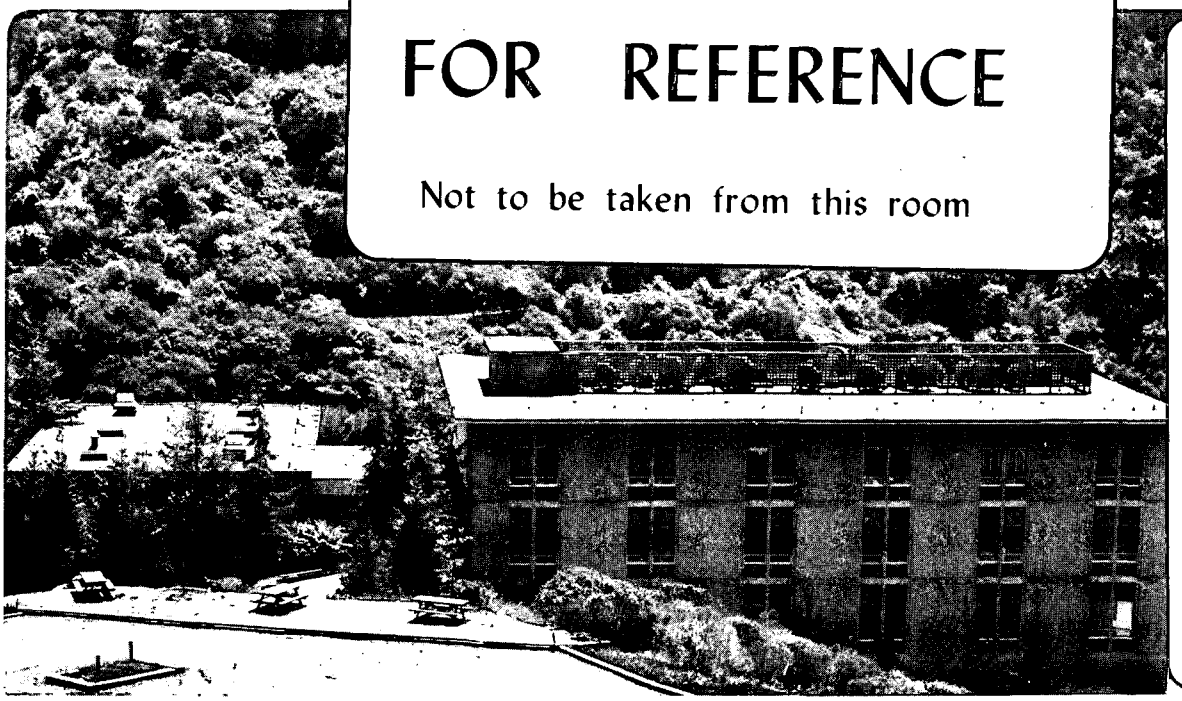

LBL-31541
Copy 1
Bldg. 50 Library.

Prepared for the U.S. Department of Energy under Contract Number DE-AC03-76SF00098

DISCLAIMER

This document was prepared as an account of work sponsored by the United States Government. Neither the United States Government nor any agency thereof, nor The Regents of the University of California, nor any of their employees, makes any warranty, express or implied, or assumes any legal liability or responsibility for the accuracy, completeness, or usefulness of any information, apparatus, product, or process disclosed, or represents that its use would not infringe privately owned rights. Reference herein to any specific commercial product, process, or service by its trade name, trademark, manufacturer, or otherwise, does not necessarily constitute or imply its endorsement, recommendation, or favoring by the United States Government or any agency thereof, or The Regents of the University of California. The views and opinions of authors expressed herein do not necessarily state or reflect those of the United States Government or any agency thereof or The Regents of the University of California and shall not be used for advertising or product endorsement purposes.

Lawrence Berkeley Laboratory is an equal opportunity employer.

DISCLAIMER

This document was prepared as an account of work sponsored by the United States Government. While this document is believed to contain correct information, neither the United States Government nor any agency thereof, nor the Regents of the University of California, nor any of their employees, makes any warranty, express or implied, or assumes any legal responsibility for the accuracy, completeness, or usefulness of any information, apparatus, product, or process disclosed, or represents that its use would not infringe privately owned rights. Reference herein to any specific commercial product, process, or service by its trade name, trademark, manufacturer, or otherwise, does not necessarily constitute or imply its endorsement, recommendation, or favoring by the United States Government or any agency thereof, or the Regents of the University of California. The views and opinions of authors expressed herein do not necessarily state or reflect those of the United States Government or any agency thereof or the Regents of the University of California.

LBL-31541

A Surface Science Investigation of Silicon Carbide: Oxidation, Crystal Growth and Surface Structural Analysis

James Michael Powers
Ph.D. Thesis

Department of Chemistry
University of California

and

Materials Sciences Division
Lawrence Berkeley Laboratory
University of California
Berkeley, CA 94720

November 1991

This work was supported by the Director, Office of Energy Research, Office of Basic Energy Sciences, Materials Sciences Division, of the U.S. Department of Energy under Contract No. DE-AC03-76SF00098.

Table of Contents

1 Silicon Carbide
- 1.1 The Crystal Structure ____ 1
- 1.2 Mechanical and Chemical Properties ____ 3
- 1.3 Electronic Properties ____ 4
- 1.4 Why Study the SiC Surface? ____ 5

2 Experimental
- 2.1 Introduction ____ 7
- 2.2 Ultra High Vacuum ____ 7
- 2.3 Electron Guns ____ 10
- 2.4 Electron Multipliers ____ 13
- 2.5 Experimental Techniques
  - 2.5.1 Auger Electron Spectroscopy ____ 15
  - 2.5.2 X-Ray Photoelectron Spectroscopy ____ 21
  - 2.5.3 Low Energy Electron Diffraction ____ 25
  - 2.5.4 Mass Spectrometry ____ 32
- 2.6 SiC Surface Preparation ____ 36

3 The Surface Oxidation of α-SiC by O_2
- 3.1 Introduction ____ 38
- 3.2 Experimental ____ 41
- 3.3 Results
  - 3.3.1 Surface Composition of α-SiC as a Function of Temperature and O_2 Pressure ____ 46
  - 3.3.2 The Role of Surface Defects in the Oxidation of α-SiC by O_2 ____ 56
- 3.4 Discussion
  - 3.4.1 Surface Composition of α-SiC as a Function of Temperature and O_2 Pressure ____ 58
  - 3.4.2 The Role of Surface Defects in the Oxidation of α-SiC by O_2 ____ 63
- 3.5 Conclusions ____ 64

4 The Preparation and Characterization of $Si_xC_yH_z$ Films by Plasma Enhanced Chemical Vapor Deposition
4.1 Introduction 67
4.2 Plasma Enhanced Chemical Vapor Deposition 68
4.3 Experimental 71
4.4 Mass Spectrometric Analysis of a CH_3SiH_3 Plasma
4.4.1 Neutral Species 78
4.4.2 Positive Ion Species 80
4.5 $Si_xC_yH_z$ Film Composition and Structure
4.5.1 Influence of the Substrate Temperature 83
4.5.2 Influence of the R.F. Power 89
4.5.3 Film Density and Stress 89
4.5.4 Film Structure 91
4.6 Conclusions 96

5 Surface Crystallography of β-SiC by LEED
5.1 Introduction 98
5.2 Dynamic LEED Theory
5.2.1 Calculational Overview 100
5.2.2 The Muffin-Tin Model 101
5.2.3 Intra- and Interlayer Electron Scattering 104
5.2.4 R-Factors 105
5.3 Experimental 107
5.4 The β-SiC (100)-c(2x2) Surface
5.4.1 Introduction 108
5.4.2 Surface Preparation 112
5.4.3 LEED Analysis and Structural Models Examined 114
5.4.4 Results and Discussion 118
5.5 The β-SiC (100)-(2x1) Surface
5.5.1 Introduction 127
5.5.2 LEED Analysis and Structural Models Examined 130
5.5.3 Results and Discussion 133
5.6 Conclusions 136

List of Figures

1.1 Ideal SiC single crystal structure 2

2.1 Schematic diagram of an on-axis electron gun 12
2.2 A discrete dynode electron multiplier 14
2.3 A Channeltron electron multiplier 14
2.4 The Auger electron emission process 16
2.5 Universal curve of electron escape depth 18
2.6 A cylindrical mirror analyzer 20
2.7 XPS with a concentric hemispherical analyzer 24
2.8 The low energy electron diffraction process 26
2.9 LEED with a retarding field analyzer 27
2.10 The Rh (100)-($\sqrt{2}$x$\sqrt{2}$)R45°-O system 31
2.11 The quadrupole mass spectrometer 33
2.12 Typical mass spectrum of an UHV system 35

3.1 The ideal α-SiC {0001} surfaces 39
3.2 Varian UHV chamber used for LEED 42
3.3 Na_2CO_3 etch patterns for the α-SiC {0001} surfaces 45
3.4 The α-SiC (000$\bar{1}$) surface composition vs. temperature 47
3.5 AES intensities of α-SiC vs. O_2 exposure at 300K 49
3.6 AES spectra of clean α-SiC, O_2 exposed α-SiC and clean SiO_2 50
3.7 The Si 2p BE peak of air exposed α-SiC 52
3.8 The α-SiC (0001) surface composition after exposure to 1 atm O_2 at various temperatures 54
3.9 The I(O)/I(Si) AES ratio of α-SiC vs. O_2 exposure at 773K 57
3.10 AES intensities of α-SiC (000$\bar{1}$)-(1x1) vs. O_2 exposure at 973K 59

4.1 Schematic diagram of the R.F. plasma deposition system 70
4.2 Plasma potential as it varies between the two electrodes 72
4.3 Self-bias voltage vs. R.F. power 73

4.4 Schematic of the plasma deposition and mass analysis system 74
4.5 Photo of the plasma deposition and mass analysis system 75
4.6 Mass spectra of CH_3SiH_3 in the presence and absence of a R.F. plasma 79
4.7 Mass spectra of the cations collected at the grounded and powered electrode. 82
4.8 The C 1s BE peak of a $Si_xC_yH_z$ film deposited at 723K on the powered electrode 87
4.9 The Si 2p BE peak of a $Si_xC_yH_z$ film deposited at 723K on the powered electrode 88
4.10 The FTIR spectra of $Si_xC_yH_z$ films deposited under various conditions 92

5.1 Sketch of the muffin-tin potential at a surface 102
5.2 Diagram of the renormalized forward scattering scheme 106
5.3 Silicon-terminated models for the β-SiC (100)-(1x1) and c(2x2) surfaces 110
5.4 Schematic of the β-SiC (100)-c(2x2) LEED pattern 113
5.5 The I-V curves of the (0,1) and (1,1) beams of the c(2x2) surfaces produced by Si sublimation and C_2H_4 exposure 115
5.6 The I-V curves of the ($^1/_2$,$^1/_2$) and ($^1/_2$,$^3/_2$) beams of the c(2x2) surfaces produced by Si sublimation and C_2H_4 exposure 116
5.7 Carbon-terminated models for the β-SiC (100)-c(2x2) surface 119
5.8 AES spectra of the β-SiC (100)-(2x1) and c(2x2) surfaces 121
5.9 The best-fit structure for the c(2x2) produced by C_2H_4 exposure and Si sublimation 125
5.10 Symmetric dimer model of the β-SiC (100)-(2x1) surface 128
5.11 Asymmetric dimer model of the β-SiC (100)-(2x1) and c(4x2) surfaces 129
5.12 The β-SiC (100)-(2x1) predicted by total energy calculations 131
5.13 Schematic of the β-SiC (100)-(2x1) LEED pattern 132
5.14 (2x1) reference structures for the TLEED analysis of the β-SiC (100)-(2x1) reconstruction 134
5.15 The best-fit structure for the β-SiC (100)-(2x1) 135

List of Tables

1.1 Common SiC crystal structures 3
2.1 Monolayer adsorption time as a function of pressure 8
3.1 Oxidation of α-SiC with 1 atm O_2 at 1323K for 60 min. 55
4.1 Rates of $Si_xC_yH_z$ film deposition as a function of temperature 84
4.2 $Si_xC_yH_z$ film composition as a function of temperature and electrode 85
4.3 $Si_xC_yH_z$ film density as a function of temperature and electrode 90
4.4 Assignment of the IR absorption bands in the 400-1100 cm^{-1} range 95
5.1 Models of the β-SiC (100)-c(2x2) examined using conventional dynamical LEED 122
5.2 Models of the β-SiC (100)-c(2x2) examined using tensor LEED 124

Acknowledgements

In the spring of 1987 I had narrowed my choice of graduate schools to U.C. Berkeley and Cal. Tech., both of which offer top-notch faculty and research facilities. The diversity of the people and research at U.C. Berkeley was for me the deciding factor. Berkeley is a challenging and rewarding place that allows one to see all the different facets of science. I have learned a great deal during my four years here, and yet I know I have only scratched the surface of what Berkeley has to offer. As I prepare to leave I would like to express my gratitude to some of the many people who have made my time here so happy and productive.

First and foremost, I would like to thank my research advisor Professor Gabor Somorjai for his patience and efforts. His passion for surface science is infectious, and his insistence that I look at the "Big Pictures" of science has opened my eyes and mind to many new areas. I would also like to thank Drs. Miquel Salmeron and Michel Van Hove for helping me plan my research as well as deal with the day to day experimental problems. Together, these three have produced a learning environment that is exciting, challenging and supportive.

Lawrence Berkeley Laboratory is staffed by a talented and diverse collection of people from virtually every corner of the globe. Several of them have been instrumental in my studies and have earned my respect and appreciation. Gerard Vurens, my first teacher, taught me many of the tricks of the trade of surface science. Marie-Paule Delplancke contributed substantially towards the $Si_xC_yH_z$ thin film project and also taught me the joys of French cuisine. Michael Rubin and Joel Ager provided the FTIR and Raman analysis of our $Si_xC_yH_z$ thin films. Adrian Wander performed

the structural analysis of my experimental LEED data and patiently explained the concepts behind the calculations.

Experimental work always involves mistakes, missteps and damaged equipment. The support staff of LBL deserves considerable credit for helping me maintain my systems one step ahead of disaster. I would like to thank Dan Colomb and Bob Wright of the machine shop for keeping me under vacuum and Jim Severns and Bob Ybarra of the electronics shop for replacing blown components.

Many people made the four years more pleasurable: Gil Vandentop, who always beat me badly in foozball; Michael Quinlan, with his unique perspective on life; Sabrina Fu and Colette Knight for verbal sparring; and Kazuhisa Kobayashi who taught me to drink sake and enjoy life a bit more.

Finally, I would like to acknowledge AT&T for the award of a Ph.D. Fellowship during my stay at U.C. Berkeley. This work was supported by the Director, Office of Energy Research, Office of Basic Energy Sciences, Materials Sciences, Materials Sciences Division, U.S. Department of Energy under Contract No. DE-AC03--76SF00098. Supercomputer time for the dynamical LEED calculations was made available by the University of California Berkeley Computer Center.

Chapter 1

Silicon Carbide

1.1 The Crystal Structure

Silicon carbide (SiC) has received considerable attention in recent years as research has been directed towards understanding semiconductors capable of withstanding high temperatures and harsh environments.[1-3] Single crystal SiC consists of a 1:1 silicon to carbon atomic ratio. Like diamond or silicon, the atoms in SiC are sp^3 hybridized with each atom surrounded by four next-nearest neighbors, but in this case of the opposite type. The crystal structure can be thought of being composed of silicon and carbon "bi-layers" stacked atop of each other. (fig. 1.1) There are three possible positions, referred to as A, B, and C, in the stacking of these silicon and carbon bi-layers. The order in which these bi-layers are stacked relative to each other dictates whether the crystal is alpha- or beta-silicon carbide (α-SiC vs. β-SiC). Beta-silicon carbide consists of bi-layers stacked in the sequence ABCABC..., meaning it is a face-centered cubic (fcc) lattice with a two atom basis set. More than 170 polytypes of α-SiC have been discovered.[4] Polytypism in crystals is characterized by a stacking sequence with a long repeat unit along the crystal stacking axis. To conveniently specify the various polytypes, Ramsdell proposed labeling each crystal structure by the number of bi-layers in the unit cell and the unit cells symmetry (C: cubic, H: hexagonal, and R: rhombohedral).[5]

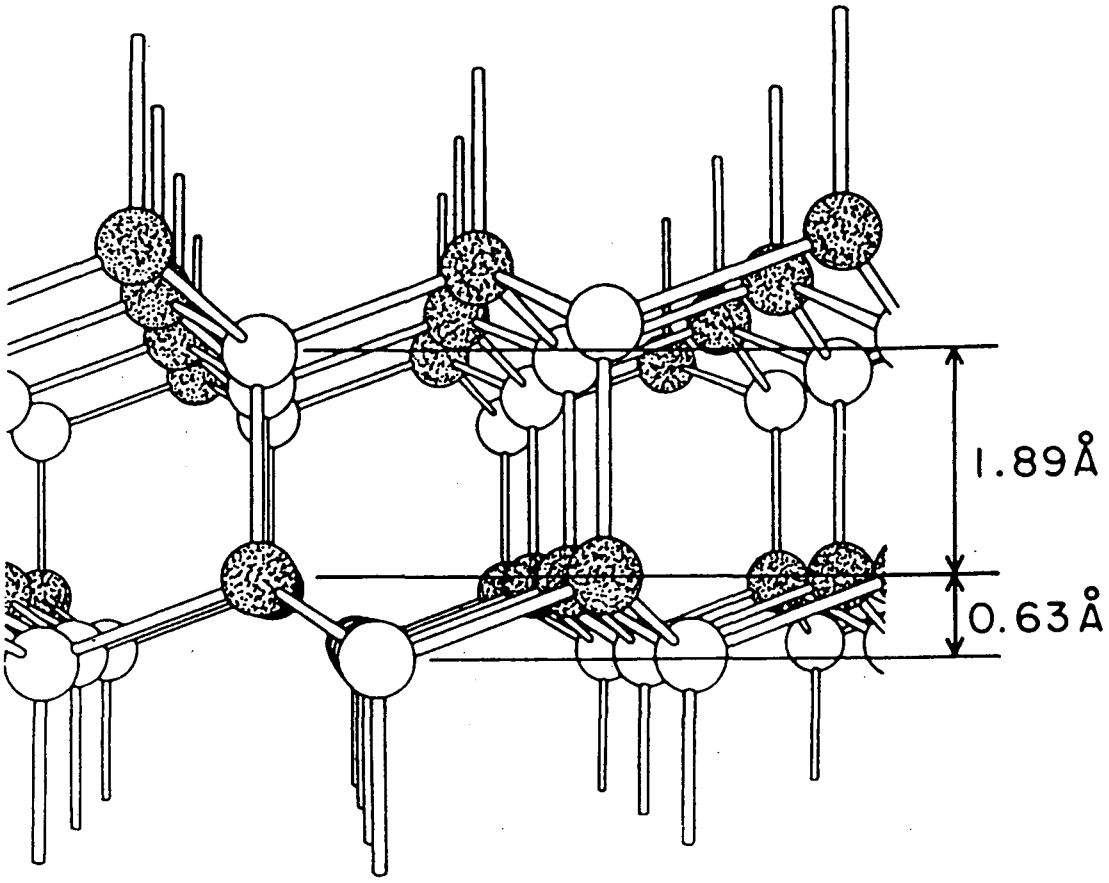

Fig. 1.1: Ideal SiC single crystal structure (L. Muehlhoff et. al., *J. Appl. Phys.*, **60(8)**, 2842 (1986))

The most common SiC crystal structures are shown in table 1.1.

Table 1.1: Common SiC Crystal Structures

	Stacking Sequence	Ramsdell Notation	Unit Cell Dimensions
β-SiC	ABC	3C	a=4.35 Å *
α-SiC	ABAC	4H	a=3.08 Å, c=10.25 Å [6]
	ABCACB	6H	a=3.08 Å, c=15.12 Å [6]
	ABCBACABACBCACB	15 R	a=3.07 Å, c=37.30 Å [7]

* Refers to a conventional cubic unit cell

The SiC polytype 393R has a primitive cell with a=3.08 Å and c=989.6 Å.[8] The mechanism responsible for this long range crystallographic order is believed to be associated with the presence of spiral steps caused by dislocations in the growth nucleus.[8] Thermodynamically, β-SiC is the more stable phase below approximately 2,300 K, at which point an irreversible β-SiC to α-SiC transformation occurs.[9]

1.2 Mechanical and Chemical Properties

Silicon carbide is a brittle ceramic known for its high decomposition temperature (3,100 K) and extreme hardness (9.3 on the Mohs Hardness Scale of 1 to 10). It possesses a relatively high thermal conductivity (0.41 W/cm °C for α-SiC at 300 K) and is resistant to high energy radiation damage due to its low Z number. Chemically, it is resistant to attack by

aqueous acids, alkalis and oxidation. However, it is vigorously reactive towards certain metals (Ti, V, Cr, Mn, Fe, Co) and metal oxides.

The 1970 Minerals Yearbook placed the annual U.S. and Canadian production of SiC at 1.5×10^8 kg. The majority of commercially produced SiC (metalurgical-grade: 90% purity) is utilized for deoxidizing ferrous alloys so that they are easily machinable. Higher purity (95-99%) SiC is utilized as an abrasive and also as a refractory material for high temperature shielding applications.

1.3 Electronic Properties

In terms of profits and volume, the majority of SiC production is directed towards metallurgy, abrasives and refractories. However, in recent years the most exciting work with SiC has been directed towards utilizing its semiconductor properties. Both α- and β-SiC are large bandgap semiconductors that can be doped both p- and n-type. Beta-silicon carbide possesses a bandgap energy of 2.3 eV, while the various α-SiC polytypes generally possess larger bandgap energies.[10] Polytype 6H, the most common α-SiC structure, possesses a bandgap energy of 2.86 eV.[11] This variation in bandgap energies among the various polytypes of α-SiC has caused considerable difficulties in exploring the electronic properties of the material. Recent advancements in high temperature chemical vapor deposition of β-SiC have made it the most desirable crystal form for electronic uses.[12-14]

Large bandgap energies allow semiconductors to be used in high temperature electronic applications since thermal excitation of electrons from the valence band to the conduction band is not a problem. Silicon,

with a bandgap energy of only 1.1 eV, is unreliable for electronic applications above 473 K.[15] In contrast, SiC metal/oxide/semiconductor field effect transistors (MOSFETs) have been shown to operate up to 925 K.[15] With a saturated drift velocity considerably higher than silicon (2.5×10^7 vs. 1×10^7 cm/sec), β-SiC may be used for high frequency electronic applications.[15] Lastly, unlike GaAs or diamond, stable insulating layers of SiO_2 can be produced on SiC with many of the same techniques used already in commercial silicon fabrication.

1.4 Why Study the SiC Surface?

Silicon carbide is often thought of as a hybrid of diamond and silicon. Like diamond, it is resistant to oxidation and chemical attack by aqueous acids and alkalis. Like silicon, it is a semiconductor capable of supporting a stable insulating oxide layer. With its large bandgap energy and high thermal conductivity, SiC is a promising candidate for high temperature or high frequency electronic applications. However, several problems associated with the production of SiC and its surface reactivity have limited its applications. We have addressed three of these problems in this work.

The fabrication of uniform surface oxide layers on SiC is not a well understood process, although considerable research has been performed in order to model it. For example, Suzuki et al. found that exposure of the α-SiC {0001} surfaces at 1,273 K to H_2O saturated O_2 (P= 1 atm) for two hours produced 152 Å of SiO_2 on the (0001) surface and 908 Å of SiO_2 on the $(000\bar{1})$ surface.[16] While other researchers have reported similar differences in the oxidative behavior of the {0001} surfaces, the cause of

the phenomena is unknown.[17-19] This question led us to examine the oxidation of α-SiC by O_2 over a wide pressure and temperature range in hopes of explaining the previous results.

Chemical vapor deposition (CVD) is currently the preferred method for production of high quality single crystal films of SiC on silicon substrates. Unfortunately, the deposition process is slow, prone to contamination and requires substrate temperatures in excess of 1,373 K. The high temperature, required in part for the thermal dissociation of the gas phase molecules, limits the applicability of the CVD process. We have attempted to produce SiC thin films at lower temperatures utilizing plasma enhanced CVD. The plasma, created by a radio frequency electrical discharge between two parallel plates, effectively dissociates gas phase molecules, allowing lower substrate temperatures to be utilized. We have studied the composition, density and morphology of the deposited SiC films as a function of substrate temperature, plasma power and ion flux bombardment of the surface during deposition.

Lastly, compositional changes of the SiC surface at high temperature complicate the fabrication of metal to SiC junctions, which are crucial for electronic applications. We have utilized low energy electron diffraction (LEED) to examine the β-SiC (100) surface structure and composition as a function of temperature. High temperature annealing of the SiC surface in vacuum results in the removal of surface silicon, which causes several distinct surface reconstructions. These surface reconstructions exhibit several unique chemical characteristics.

Chapter 2

Experimental

2.1 Introduction

Rarely does any one experimental technique give all the desired information. This is particularly true in surface science studies, where a variety of experimental techniques must often be employed in order to "piece together" the answer. This chapter does not attempt the daunting task of describing the large number of surface science tools available to the scientist of today. Instead, it attempts to provide a concise summary of the analytical techniques and instrumentation used in these experiments at a level suitable for a beginning chemistry graduate student.

The reasons for working in ultrahigh vacuum (UHV) are discussed, as well as how it is produced and maintained. Electron guns and multipliers, used throughout this work, are described in detail. Surface compositional analysis by Auger electron spectroscopy (AES) and x-ray photoelectron spectroscopy (XPS) is described, as is surface structural analysis by low energy electron diffraction (LEED). The identification of gas phase species by mass spectrometry is discussed briefly. Lastly, the techniques used to clean and order SiC surfaces are explained.

2.2 Ultrahigh Vacuum (UHV)

Ultrahigh vacuum is generally considered to be a pressure of 10^{-8} Torr or less. Pressures this low are required by most surface science

experimental techniques for two reasons. First, the majority of techniques involve the bombardment and/or ejection of charged particles from the surface of the sample. The background gas pressure must be low enough so that a significant fraction of the charged particles are not altered by collisions with gas phase molecules while traveling to or from the surface. To meet this requirement, chamber pressures must typically be less than 10^{-4} Torr. A more stringent requirement placed on the quality of the vacuum is the need to minimize contamination of the sample's surface during the course of an experiment. Using the kinetic theory of gases, one can calculate the time needed for a surface to adsorb one monolayer of gas.[20]

Table 2.1: Air at 20° C

	Pressure (Torr)	Mean Free Path (cm)	Times for Monolayer Formation (sec)*
One atmosphere	760	7×10^{-6}	3.3×10^{-9}
Rough Vacuum	10^{-3}	5	2.5×10^{-3}
High Vacuum	10^{-6}	5×10^{3}	2.5
Ultrahigh Vacuum	10^{-9}	5×10^{6}	2.5×10^{3}

*Assumes unit adhesion efficiency and a molecular diameter of 3 Å

As table 2.1 shows, the monolayer adsorption time increases dramatically with decreasing pressure. Hence, to maintain the surface cleanliness of the sample over the timescale of an experiment (10^3-10^4 sec) requires a chamber pressure of 10^{-9} to 10^{-10} Torr.

The pumping of a vacuum system from atmospheric pressure to 10^{-10} Torr typically involves several steps. For these experiments, the three UHV chambers utilized were first rough pumped from 760 Torr to approximately 100 mTorr using oil-sealed rotary vacuum pumps. Once

completed, the mechanical pumps were valved off from the vacuum chamber and the system was further pumped to 10^{-6} Torr using either a vapor diffusion pump or a turbomolecular pump. In a diffusion pump gas molecules are driven from the pump inlet to the outlet by momentum transfer from a directed stream of oil vapor. The oil vapor jet is produced by heating a high molecular weight oil at the bottom of the pump and directing the resulting vapor downward through a series of nozzles. The oil jets drive gas molecules from the vacuum system towards the outlet where they are pumped away by a rotary vacuum pump.

Turbomolecular pumps also utilize momentum transfer to direct gas from the pump inlet towards the exhaust. Like a turbine, a turbomolecular pump has a series of rotors with oblique radial slots turning at 20,000 to 50,000 rpm. When a gas molecule strikes a rotor at this speed, a significant component of momentum is transferred to the molecule in the direction of rotation. This drives the molecule to the exhaust of the turbo pump, where it is pumped away by a rotary vacuum pump.

Ion pumps were utilized to bring the UHV chambers to their base pressure of 10^{-9} to 10^{-10} Torr. These pumps use an electrical discharge magnetically confined between a stainless steel anode and a titanium cathode. The discharge is maintained by placing a potential difference of 5 kV across the electrodes. Gas molecules are ionized in the discharge and accelerated by the potential gradient into the titanium cathode. Due to their high kinetic energy, the ions are permanently buried in the cathode. This ion bombardment also results in the deposition of titanium on the anode. Active gases such as N_2, CO, H_2O and O_2 are chemisorbed by this deposited titanium, effectively removing them from the vacuum system.

An excellent review of these pumping methods and others may be found in *Building Scientific Apparatus*.[21]

The rate of gas evacuation from a vacuum chamber at pressures below 10^{-6} Torr is not limited by the pumping speed of the system. Rather, the limiting factor is the slow desorption of water and hydrocarbon gases from the walls of the chamber. In order to attain 10^{-10} Torr in a reasonable timescale, the entire vacuum system should be baked at 100°-200° C for several hours in order to remove these gases from the chamber walls. The chambers in these experiments were baked by mounting strip heaters on the chambers and then surrounding the chamber with insulation to facilitate uniform heating.

2.3 Electron Guns

Electron guns are found in virtually all surface analytical chambers and are used for a variety of purposes such as AES and LEED. Although they can vary considerably in complexity, all electron guns consist of an electron source and a series of lenses to collimate and focus the beam. The production of electrons may be done by several methods; thermionic emission, field emission, photoelectron emission or electron impact ionization. Thermionic emission, the most common method, was utilized for these studies. Thermionic emission may be thought of as heating a material to such a high temperature that electrons "boil-off" from the surface into the vacuum. The Richardson-Dushman equation for thermionic emission states the rate of electron emission (E) from a metal depends exponentially on the work function (Φ) of the metal.[22]

$$E \propto \exp(-\Phi/kT) \qquad (2.1)$$

Due to this exponential dependence, metals with high work functions are often used so that small differences in temperature do not cause extreme changes in emission. In these experiments a thoriated tungsten filament at approximately 2,000 K was used to produce electron for AES and LEED.

A schematic of the electron gun used for AES and LEED is shown in fig. 2.1 along with some typical applied voltages for a primary beam energy (E_p) of 1500 eV. The hot tungsten filament emits electrons with only a few tenths of an electron volt. These very low energy electrons are accelerated away from the filament and are slightly focused by the repeller. The repeller, which surrounds the filament, is simply a metal can with a 1 mm diameter hole in the top for the electrons to escape through. Further focusing of the electron beam is performed by a pair of stacked concentric tubes in front of the repeller/filament package. The focus is typically maintained at 70% of E_p while the anode is grounded so that the region between the electron gun and the grounded sample is free of strong electric fields. Strong electric fields, as well as strong magnetic fields, are to be avoided in the UHV chamber since they can significantly distort the paths of low energy electrons.

Simple electron guns like the one described above are capable of delivering several microamperes of current to the sample in a spot size of approximately 1 mm^2. More sophisticated guns are capable of delivering nanoamperes of current in a spot size less than 10^3 nm^2. These bright, highly focused guns are usually equipped with sets of mutually perpendicular deflector plates along the central axis of the gun. These deflector plates permit the electron beam to be swept over the surface of the sample, allowing spatially resolved compositional and topological analysis via scanning AES (SAES) and scanning electron microscopy

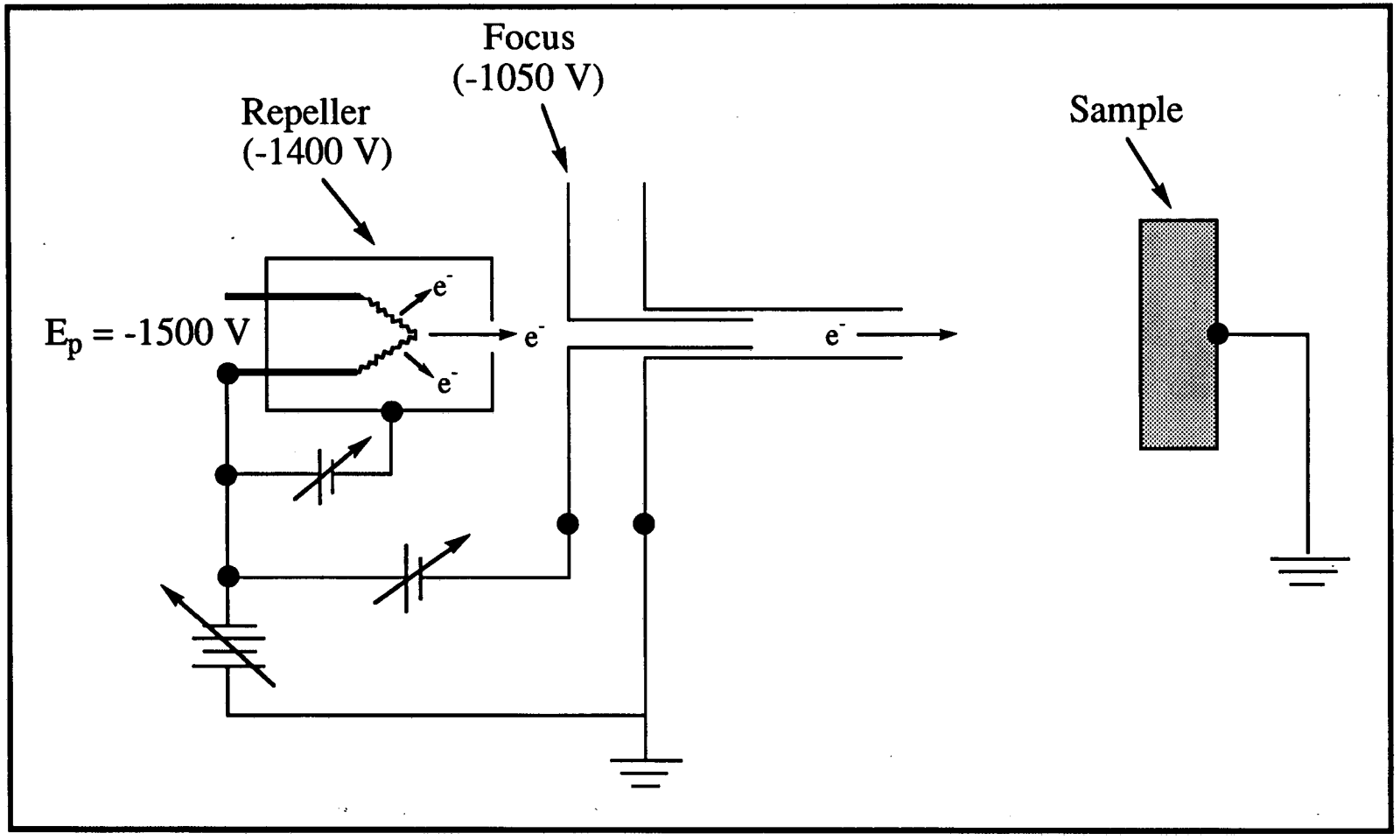

Fig. 2.1: Schematic diagram of the on-axis electron gun utilized for AES and LEED studies.

(SEM). Scanning electron microscopy measures surface topography by sweeping an electron beam over the surface of a sample and measuring the yield of secondary electrons emitted from the sample. Due to the strong dependence of the secondary yield on the incident illumination angle, surface features as small as 100 nm may be imaged.

2.4 Electron Multipliers

Electron multipliers are signal amplifiers that utilize secondary electron emission to produce their gain. As shown in fig. 2.2, these devices consist of a series of electrodes known as dynodes. These dynodes are typically fabricated from a high work function Be-Cu alloy that has been "activated" by some proprietary process. Secondary electrons are produced when the first dynode of the multiplier is struck by an ion, electron or photon of sufficient energy. These secondary electrons are accelerated towards the last dynode of the multiplier (the output terminal) by voltage differences applied between the dynodes. As the electrons move towards the output terminal they generate additional secondary electrons, creating an avalanche effect. Depending on the voltage applied and the number of dynodes, gains ranging from 1 to 10^9 are possible.

Unlike the electron multiplier described above, Channeltron(R) multipliers do not have separate dynodes. (fig. 2.3) Instead, they are continuous strip multipliers. They utilize a funnel shaped PbO doped glass tube with a semiconducting inner surface which acts as the secondary electron emitter. Due to their small size, ruggedness and resistance to oxidation, Channeltrons(R) are currently replacing discrete dynode

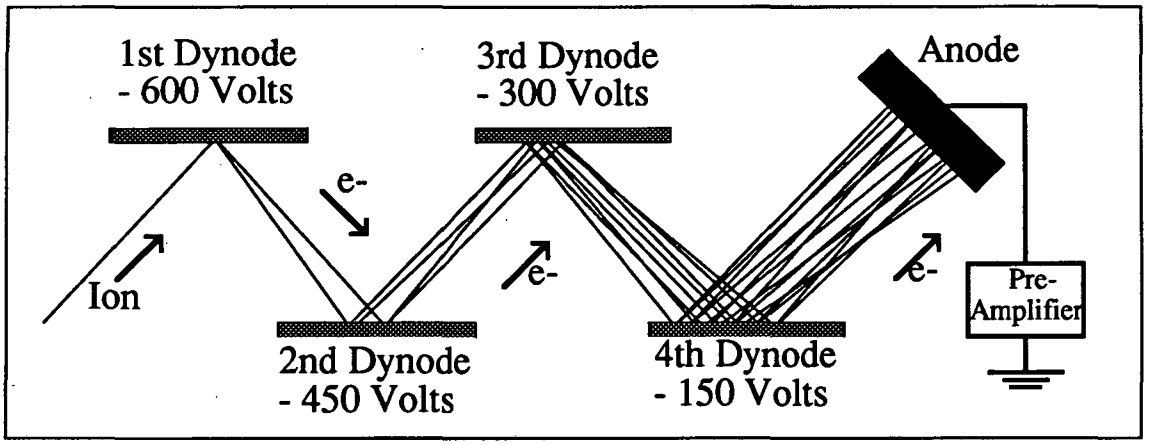

Fig. 2.2: An electron multiplier. The electrical connections shown are appropriate for detecting positive ions.

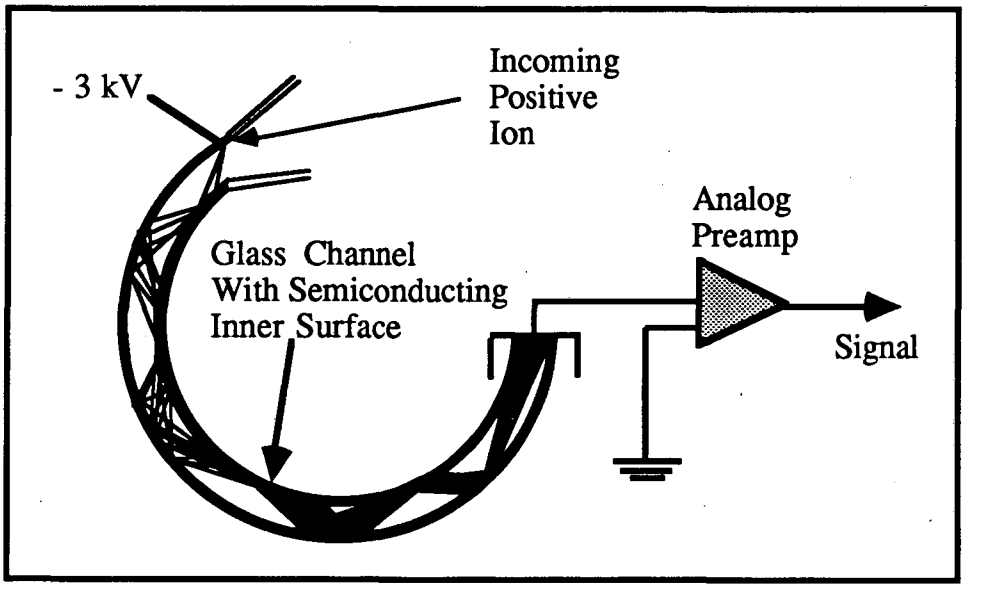

Fig. 2.3: A Channeltron electron multiplier.

multipliers in most surface science applications. Both types of multipliers have been used in these experiments.

2.5 Experimental Techniques

Three UHV analytical systems were utilized for these experiments. A Varian chamber was used for the AES, LEED and mass spectrometric analysis , while a PHI 5300 ESCA system was used for XPS studies. A PHI 660 Scanning Auger Multiprobe system was utilized for SAES, SEM and Ar^+ ion depth profiling. Each of these experimental techniques are discussed in this chapter, while the actual analytical hardware is described in Chapter 3.

2.5.1 Auger Electron Spectroscopy

Auger electron spectroscopy (AES) yields surface compositional analysis by utilizing the fact that all atoms, except for hydrogen and helium, eject Auger electrons with specific kinetic energies. By energy analyzing the Auger electrons ejected from a sample one can determine the identity of the atom of origin. Compositional analysis is performed in AES by measuring the number of electrons emitted from a sample as a function of energy (N(E)). The sensitivity of AES is limited in most cases to approximately 1% of a surface monolayer.[23]

The ejection of an Auger electron can be thought of as a two step process. The process is initiated by the creation of an excited state ion created by the ejection of a core level electron. (fig. 2.4a) This may be done by exposing the sample to bombardment by energetic x-rays or

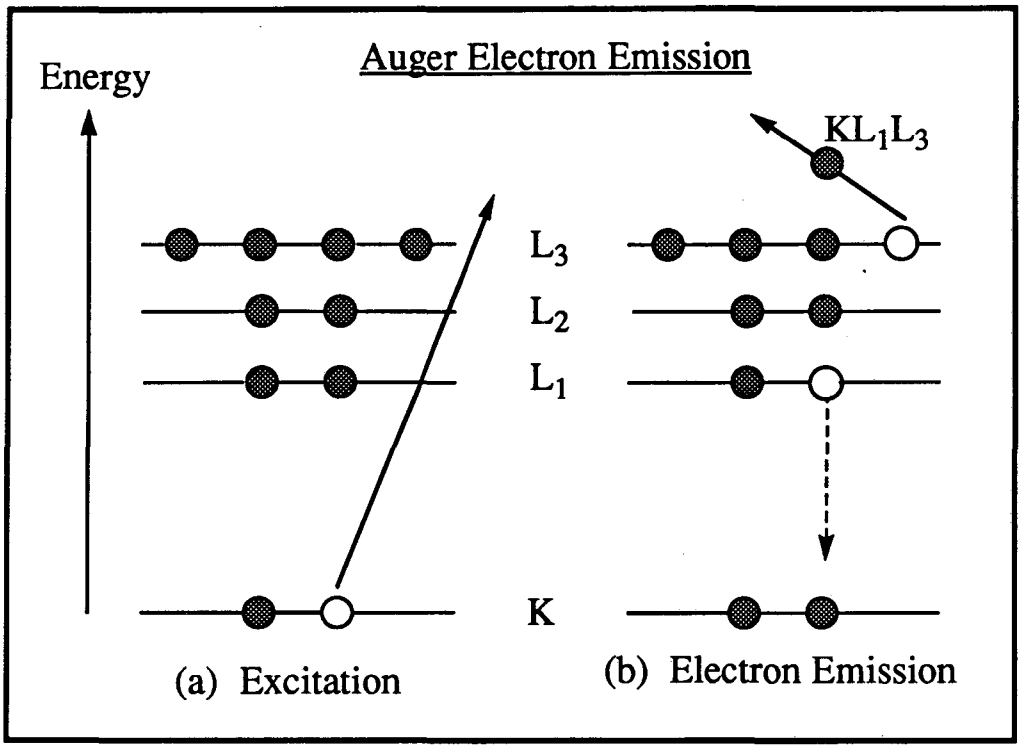

Fig. 2.4: The Auger electron emission process.

electrons (1-5 keV). Once the excited state ion is created, it can spontaneously decay into a lower energy state by the deexcitation of an electron from a higher energy electron level. (fig. 2.4b) The energy released by this deexcitation process is given to still another electron (the Auger electron), which is ejected from the ion with a energy that depends primarily of the energy level separations of the atom. It is important to note that the kinetic energy of the Auger electron is independent of the excitation method of the ion. This is chiefly because the initial ionization process occurs in less than 10^{-16} sec., whereas the lifetime of the excited state ion is typically an order of magnitude longer.

Auger electrons are typically ejected with relatively low kinetic energy (0-1000 eV) and hence are ideally suited for surface analysis. Fig. 2.5 shows the mean free path for inelastic scattering of an electron in a solid as a function of its kinetic energy.[24] Fig. 2.5 is referred to as the "Universal Curve" since the mean free path of the electron shows little dependence on the identity of the atoms in the solid. Due to their limited mean free path, electrons ejected elastically from a solid in this energy range must originate from the first few atomic layers. This phenomenon holds for all experimental techniques involving the emission of low energy electrons from a solid.

Several types of electron ejection processes can occur when a sample is bombarded with high energy electrons from an electron gun. In addition to the Auger electrons there are secondary, elastically scattered and inelastically scattered electrons ejected into the vacuum. To identify the atomic species present on the surface of the sample one must energy analyze the emitted electrons. In general, three basic methods exist for measuring the kinetic energy of charged particles. Measuring the time of

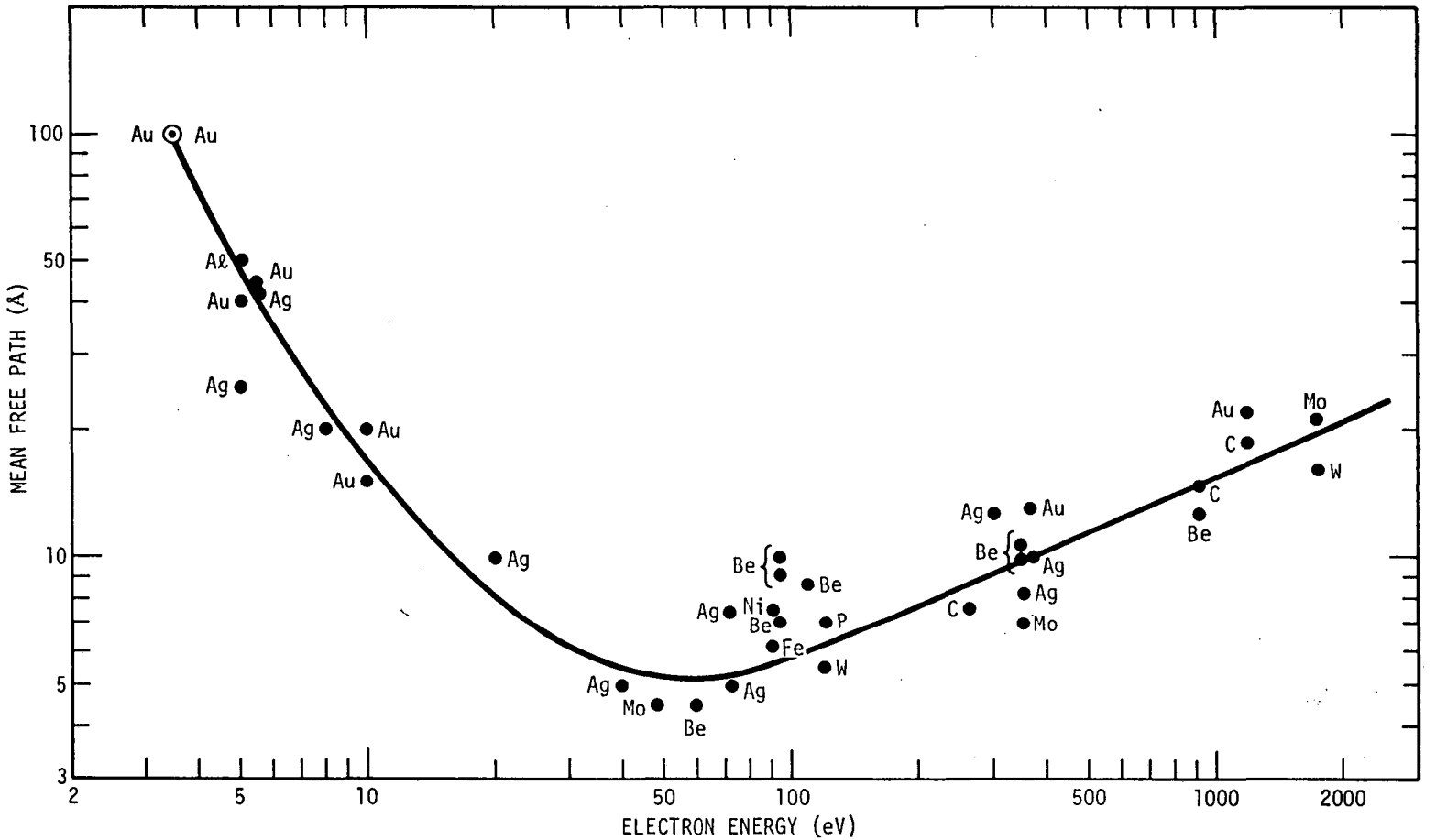

XBL 733-5917

Fig. 2.5: The mean free path of an electron in a solid as a function of electron kinetic energy. (G.A. Somorjai, *Chemistry in Two Dimensions: Surfaces*, Cornell University Press, (Ithaca and London), p. 41)

flight of a particle over a known distance is popular for ions but not for high energy electrons, since their velocities are prohibitively high. For electrons the preferred method of energy analysis usually involves either measuring the electric field required to stop the electron or the extent of path deflection in an electric or magnetic field. These concepts are behind the two most common energy analyzers for AES; the retarding field analyzer (RFA) and the cylindrical mirror analyzer (CMA). For this work, a CMA was utilized for all AES and SAES studies.

A cylindrical mirror analyzer is an electrostatic analyzer that uses coaxial cylinders as deflection plates. (fig. 2.6) For AES the inner cylinder is grounded while a negative voltage (V_{out}) is applied to the outer cylinder. Electrons emitted from the sample pass through an annular slot in the inner cylinder and are then deflected by V_{out}. For the electrons to pass through the exit slot their kinetic energy (E) must equal the pass energy of the CMA, defined by $E_{pass} = 1.7\ V_{out}$. Here, E_{pass} is in electron volts while V_{out} is in volts. Electrons with $E > E_{pass}$ strike the outer cylinder while those with $E < E_{pass}$ strike the inner cylinder. Thus by ramping V_{out} from 0 V to (E_p /1.7) one may obtain the electron energy distribution, N(E) vs E. This configuration is known as constant $\Delta E/E$ operation, since the energy resolution of the CMA (ΔE) depends linearly on the kinetic energy of the electron. For a properly operating CMA in constant $\Delta E/E$ mode, $\Delta E/E$ equals approximately 0.007. This is quite sufficient for AES where peak widths are typically 10 to 20 eV.

Typically, differentiating N(E) vs. E allows one to better distinguish the small Auger electron signal from the large, slowly varying background of secondary electrons. Electronic differentiation is performed by modulating the deflecting potential and utilizing a lock-in amplifier, which

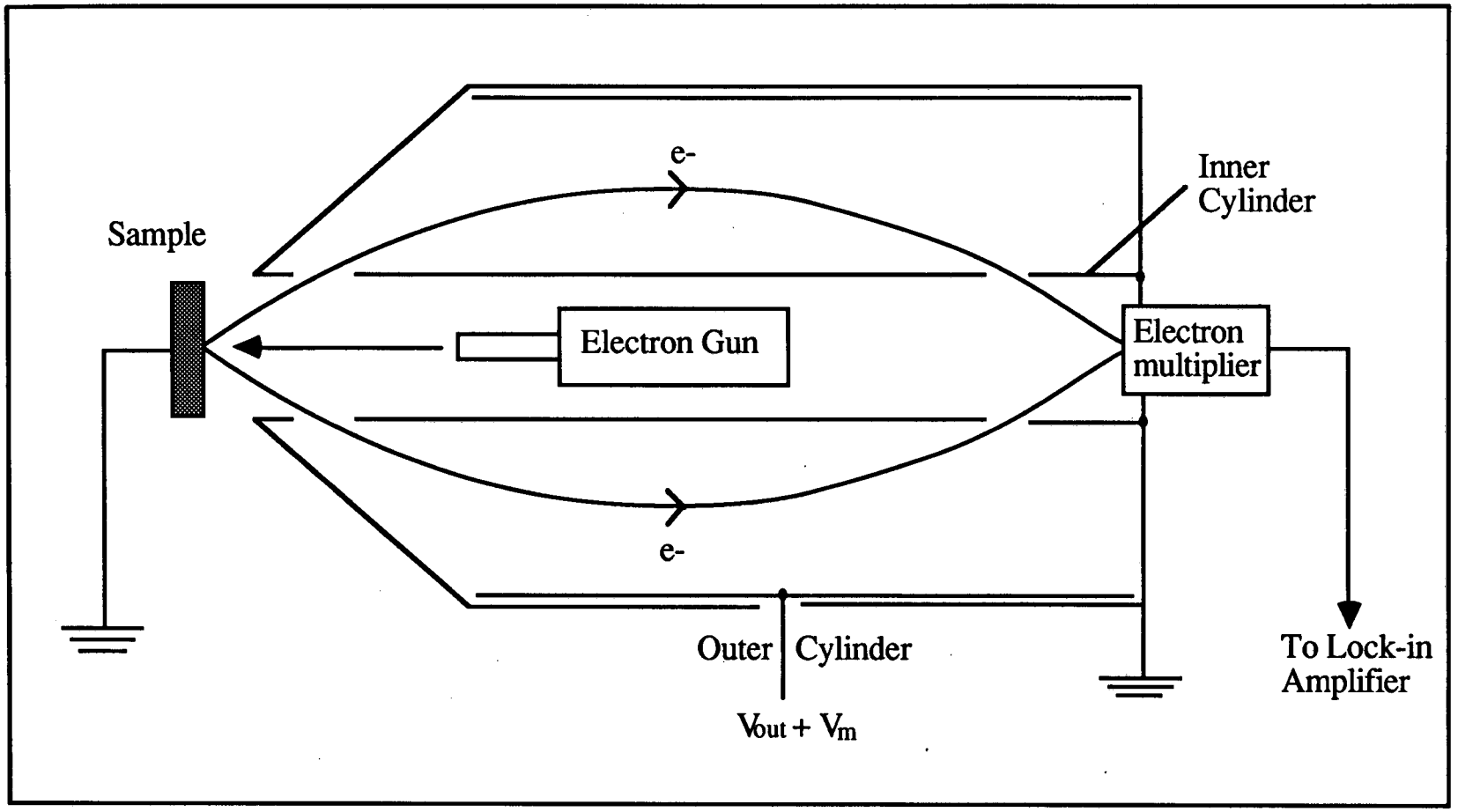

Fig. 2.6: A cylindrical mirror analyzer configured for AES.

is a phase sensitive detector. A 1-5 V A.C. modulation ($V_m \sin\omega t$) is placed on the outer cylinder of the CMA in addition to the D.C. voltage V_{out}. The current collected at the back of the CMA by the electron multiplier may be described by the Taylor series

$$I(V_{out} + V_m \sin\omega t) = I(V_{out}) + (dI(V_{out})/dV_{out})\, V_m \sin\omega t + (d^2I(V_{out})/d^2V_{out})\, (V_m)^2 \sin^2\omega t + \ldots \qquad (2.2)$$

The lock-in amplifier selects only the component of the signal with frequency ω since its amplitude is proportional to ($^{dN(E)}/_{dE}$).

2.5.2 X-Ray Photoelectron Spectroscopy

X-ray photoelectron spectroscopy is utilized to obtain quantitative surface compositional analysis as well as information concerning the chemical state of the surface atoms. This is done by irradiating the sample with soft x-rays and energy analyzing the electrons emitted into the vacuum. The kinetic energy (K.E.) of these photoelectrons is given by

$$K.E. = h\nu - B.E. - \Phi s \qquad (2.3)$$

where $h\nu$ is the photon energy, B.E. is the binding energy of the atomic orbital from which the electron originated and Φs is the work function of the energy analyzer. Typically, either Mg Kα x-rays (1253.6 eV) or Al Kα x-rays (1486.6 eV) are utilized. These photons penetrate 1-10 μm into the solid sample.[25] X-rays in this energy range are capable of creating photoelectrons from inner core atomic levels. These core level photoelectrons, with their relatively low kinetic energies (typically less than 1 keV), possess limited mean free paths in the solid. Hence, the

electrons that escape the solid to be detected come from only the first few atomic layers.

Qualitative compositional analysis of a mixed sample may be performed by comparing the peak area or height of each element present in the XPS spectrum of the sample. Quantitative compositional analysis using peak areas or heights requires the use of sensitivity factors for each peak. These factors account for such things as the photoelectric cross section of the atomic orbital, the mean free path of the photoelectron and the detection efficiency for electrons emitted from the sample.

In addition, the chemical state of each element can often be determined by measuring its peak positions and comparing them to that of known standards. A general rule of thumb is that the withdrawal of electron density from an element (i.e. oxidation) increases the binding energy of the core electrons. For example, the Si 2p B.E. in pure silicon is 99.2 eV and in SiO_2 is 103.4 eV.[26]

In most XPS studies the x-ray source is a Mg or Al anode that is bombarded by 10-15 keV electrons emitted from the cathode. The Mg anode is normally used since its x-ray intensity is higher and its line width is narrower. The Al anode is usually used either for comparison with Mg spectra to distinguish Auger peaks or when the higher Al x-ray energy is required. Auger electrons, unlike photoelectrons, have kinetic energies that are independent of the photon energy and hence appear to have different binding energies with different x-ray sources.

Electron bombardment of the Mg or Al anode results not only in the emission of the characteristic x-ray line discussed previously but also several other minor x-ray lines at higher photon energy. Thus, for each main photoelectron peak in the spectra there exists a family of smaller

peaks at lower binding energy. These satellite peaks have the spacing and intensity characteristics of the anode material.

The energy distribution of the ejected electrons in XPS is usually measured using a CMA or a concentric hemisphere analyzer (CHA). The CHA, like the CMA, is a narrow bandpass electrostatic energy analyzer. As fig. 2.7 shows, electrons with energy U_e passing through the entrance slit of the CHA are focused onto the exit slit only if the following relation holds

$$U_k = U_e (R_1/R_2 - R_2/R_1) \tag{2.4}$$

In this equation R_1 and R_2 are the radii of the two hemispheres while U_k is the potential difference between them. In comparison with the CMA, the CHA has the advantage of requiring lower potentials on the electrodes, which are closer together than the cylinders of a CMA. This results in less fringing of the electric fields inside of a CHA, allowing for better focusing and energy resolution.

The accurate determination of binding energy peak positions requires the CMA or CHA analyzer be configured for constant ΔE operation during XPS. This mode requires the energy of the electrons emitted from the sample to first be reduced by a variable electric field in front of the analyzer. Once reduced, the electron energy is accurately measured with the analyzer using a constant pass energy of about 20 eV. This results in a low, constant ΔE regardless of the initial energy of the electron. However, this increase in resolution significantly reduces the signal intensity and often necessitates the use of pulse-counting electron multipliers coupled with digital averaging of multiple consecutive N(E) vs. E scans.

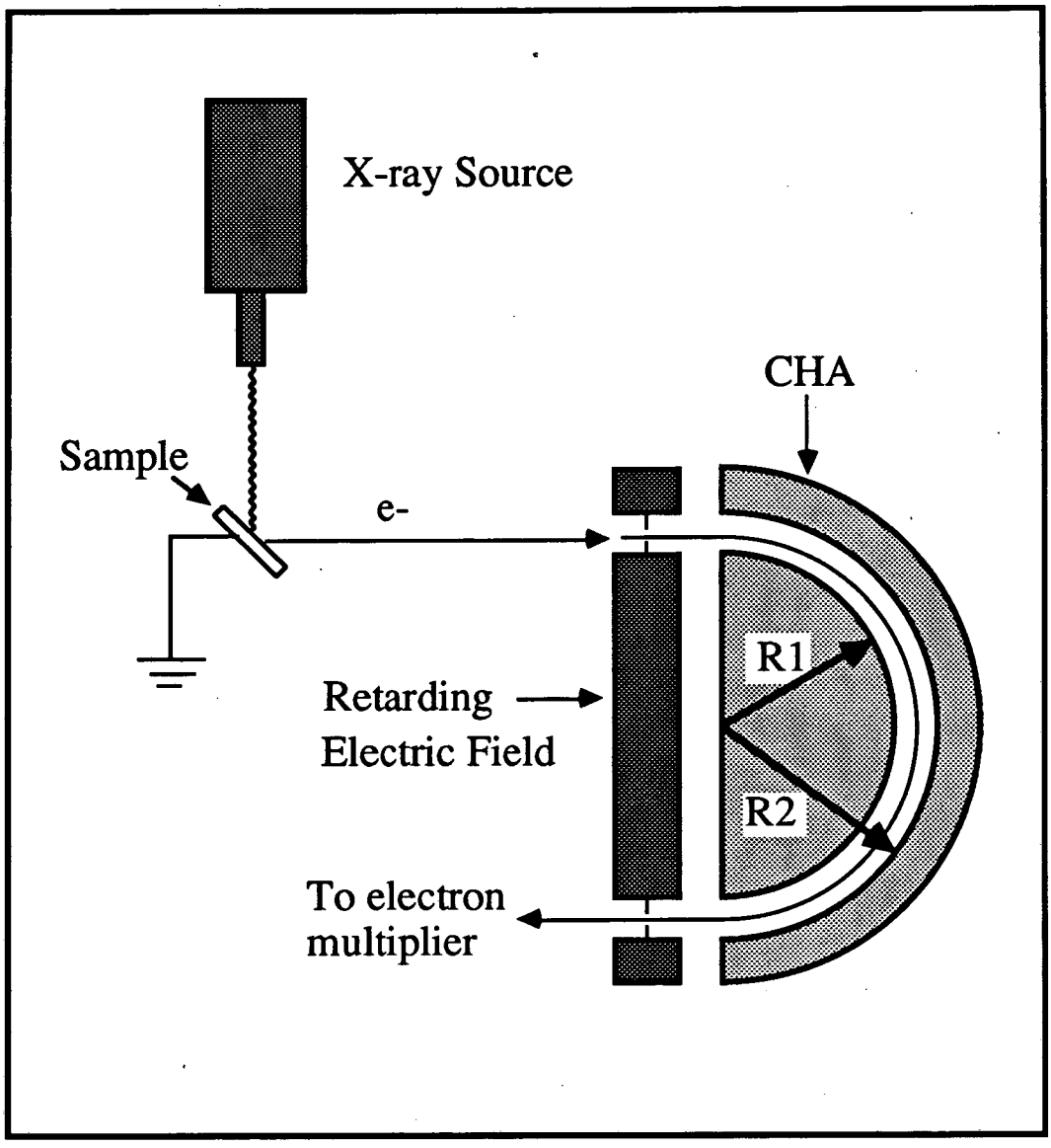

Fig. 2.7: XPS with a concentric hemispherical analyzer. The variable retarding electric field allows the CHA to operate in constant ΔE mode.

2.5.3 Low Energy Electron Diffraction

Low energy electron diffraction is utilized in order to gain information concerning the atomic structure of a crystalline surface. The technique is performed by allowing electrons of well-defined kinetic energy to diffract elastically from an ordered crystal surface. The diffracted electrons are then allowed to strike a fluorescent screen, as shown in fig. 2.8. The spots in the diffraction pattern correspond to points in a reciprocal net belonging to the repetitive crystalline surface structure. The incident electron beam may be thought of as an electron wave with a corresponding wavelength λ given by $\lambda = h/mv$. This relationship, postulated by de Broglie in 1924, defines the wavelength of a moving particle in terms of its mass (m), velocity (v), and Planck's constant (h). An electron with kinetic energy in the range 10 to 500 eV has a corresponding wavelength of 3.9 to 0.6 Å, which is comparable to interatomic distances found on solid surfaces. Hence, low energy electrons, like x-rays, can be expected to diffract from a periodic crystal lattice. However, these diffracted electrons have limited mean free paths in the solid due to their low kinetic energies. Therefore, LEED is only capable of providing structural information concerning the top 3-5 atomic layers of a solid.

A retarding field analyzer (RFA), shown schematically in fig. 2.9, is typically utilized to record the LEED pattern. The RFA consists of an on-axis electron gun surrounded by four concentric hemispherical grids and a collector plate. For LEED, the 1st grid and the sample are grounded so that there is a field-free region between the sample and the RFA. Grids 2 and 3 are connected together and are collectively referred to as the

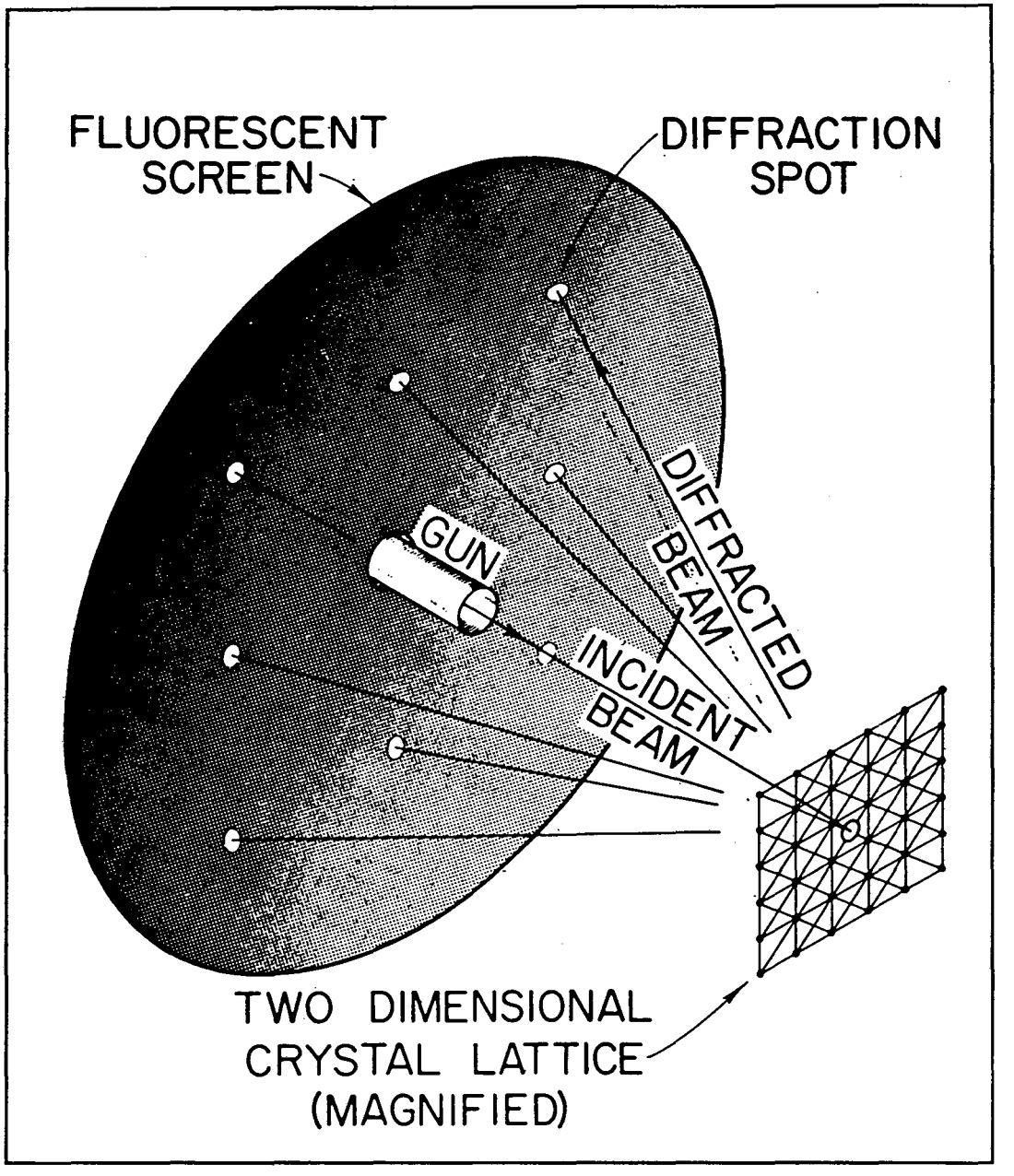

Fig. 2.8: Scheme of the low energy electron diffraction process. (G.A. Somorjai, *Chemistry in Two Dimensions: Surfaces*, Cornell University Press, p. 46)

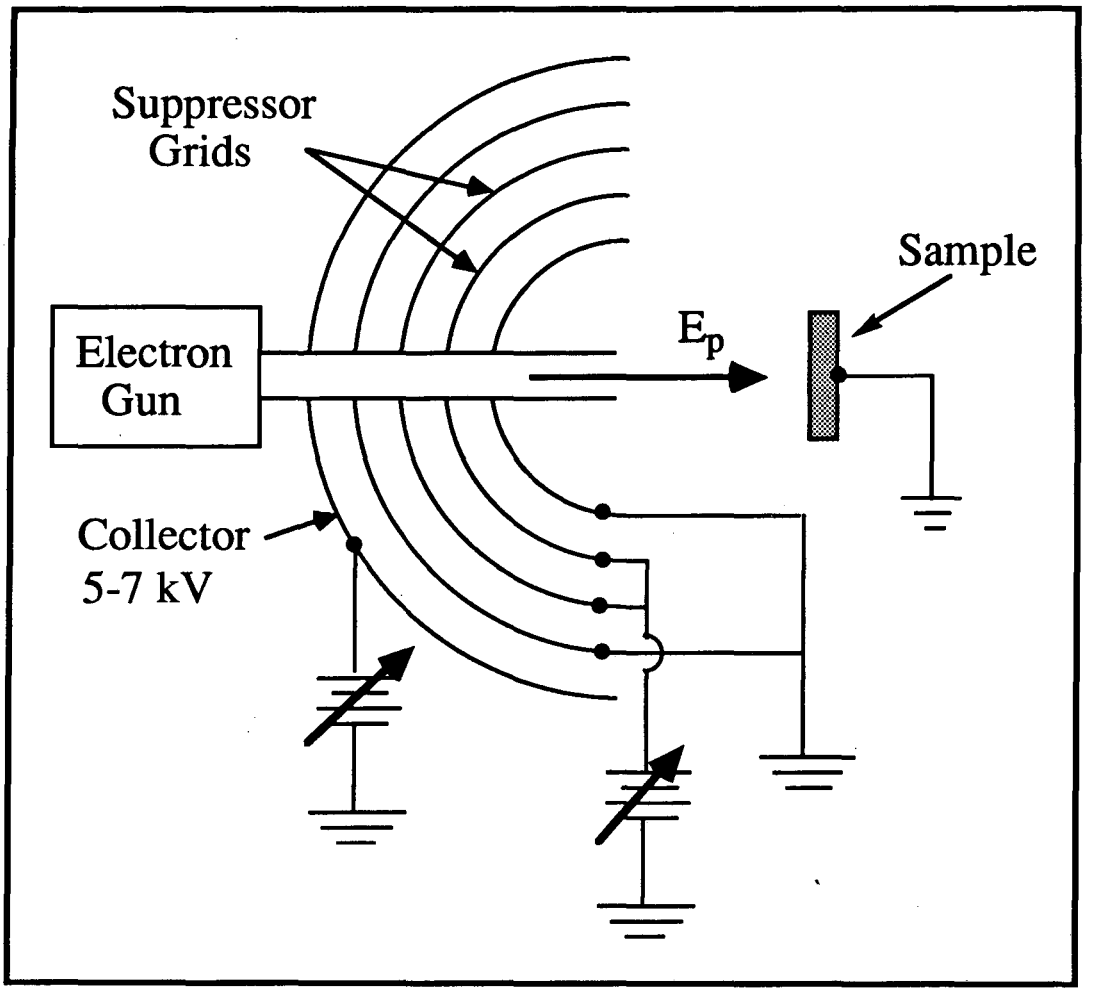

Fig. 2.9: Schematic of a LEED display system using a retarding field analyzer.

suppressor. The suppressor voltage V_s is allowed to float a few volts below E_p so that only elastically scattered electrons can pass through to the collector. Typically, only 1-5% of the electrons incident upon the sample scatter elastically. The 4th grid is grounded while the fluorescent collector is biased 3-7 kV positive. The collector exhibits "diffraction spots" at the positions of the electron interference maxima. The diffraction pattern is usually observed through a window in the UHV system and permanently recorded using still photography.

A visual examination of the LEED pattern yields considerable information concerning the surface bonding of the sample. The shape, size and symmetry of the diffraction pattern gives information concerning the size and orientation of the surface unit cell. In addition, the sharpness and overall intensity of the diffraction spots is related to the degree of order on the surface. As a surface becomes disordered, the diffraction spots broaden and become less intense as the diffuse background intensity increases.

A determination of the internal geometry of a surface unit cell cannot be performed simply by examination of the LEED pattern at one electron energy. This determination requires the intensity (I) of the diffraction spots to be measured as a function of incident electron energy (V). These I-V curves consist not only of single scattering Bragg diffraction peaks but also contain peaks created by multiple scattering of electrons in the surface region. Multiple scattering occurs because low energy electrons possess large collision cross sections, which are approximately 10^6 times larger than x-rays of similar wavelength. This large collision cross section results in a significant probability that an electron will scatter elastically from more than one atom core before it

exits the solid to be detected. This multiple scattering often does not allow the use of simple kinematical theory to determine the surface structure. A more detailed explanation of modern dynamical LEED theory can be found in Chapter 5.

A LEED pattern is a representation of the reciprocal space lattice of the surface structure. To determine the real space periodicity of the surface, one must understand the relationship between reciprocal and real space. The reciprocal space lattice is defined by two fundamental unit cell vectors **a*** and **b***. These unit cell vectors are related to the two fundamental real space vectors, **a** and **b**, by the following equations

$$\mathbf{a}^* = \frac{(\mathbf{b} \times \mathbf{z})}{\mathbf{a} \cdot (\mathbf{b} \times \mathbf{z})} \qquad \mathbf{b}^* = \frac{(\mathbf{z} \times \mathbf{a})}{\mathbf{a} \cdot (\mathbf{b} \times \mathbf{z})} \tag{2.5}$$

where **z** is the surface normal vector.

The reconstruction of a clean surface or the adsorption of a gas often results in a new surface periodicity referred to as the superlattice. The periodicity of the superlattice is referenced to the substrate lattice, ie. the periodicity of an ideal bulk-terminated surface. The relationship between the superlattice and the substrate lattice in reciprocal space is given by the following equations

$$\begin{aligned} \mathbf{a}^* &= m^*_{11}\, \mathbf{a}^{*\prime} + m^*_{12}\, \mathbf{b}^{*\prime} \\ \mathbf{b}^* &= m^*_{21}\, \mathbf{a}^{*\prime} + m^*_{22}\, \mathbf{b}^{*\prime} \end{aligned} \tag{2.6}$$

Here, $\mathbf{a}^{*\prime}$ and $\mathbf{b}^{*\prime}$ are the reciprocal unit cell vectors of the superlattice. In real space the following relationships apply

$$\begin{aligned} \mathbf{a}' &= m_{11}\, \mathbf{a} + m_{12}\, \mathbf{b} \\ \mathbf{b}' &= m_{21}\, \mathbf{a} + m_{22}\, \mathbf{b} \end{aligned} \tag{2.7}$$

where **a'** and **b'** are the real space unit cell vectors of the superlattice. The coefficients m^*_{ij} define the reciprocal space matrix of the superlattice, given by

$$M^* = \begin{pmatrix} m^*_{11} & m^*_{12} \\ m^*_{21} & m^*_{22} \end{pmatrix} \tag{2.8}$$

The real space matrix is defined by

$$M = \begin{pmatrix} m_{11} & m_{12} \\ m_{21} & m_{22} \end{pmatrix} \tag{2.9}$$

The elements of M and M* are related by the following equations:

$$m_{11} = m^*_{11} \qquad m_{21} = m^*_{12} \tag{2.10}$$
$$m_{12} = m^*_{21} \qquad m_{22} = m^*_{22}$$

An examination of a LEED pattern yields the elements of M*. Using the relationships discussed previously, one may obtain M, which defines the real space surface symmetry. An example of this transformation is shown in fig. 2.10 for the case of oxygen adsorbed on Rh (100), labeled Rh (100)-$\begin{pmatrix} 1 & 1 \\ -1 & 1 \end{pmatrix}$-O.

Although matrix notation is applicable to all cases, a simpler system is often utilized when the angle between the superlattice unit vectors **a'** and **b'** is the same as the angle between the substrate lattice unit vectors **a** and **b**. When this is the case, the surface structure is labeled using the general form p(nxm)RΦ° or c(nxm)RΦ°, depending on whether the unit cell is primitive or centered. As shown in fig. 2.10, the Rh (100)-$\begin{pmatrix} 1 & 1 \\ -1 & 1 \end{pmatrix}$-O system may also be referred to as Rh (100)-c(2x2)-O or Rh (100)-

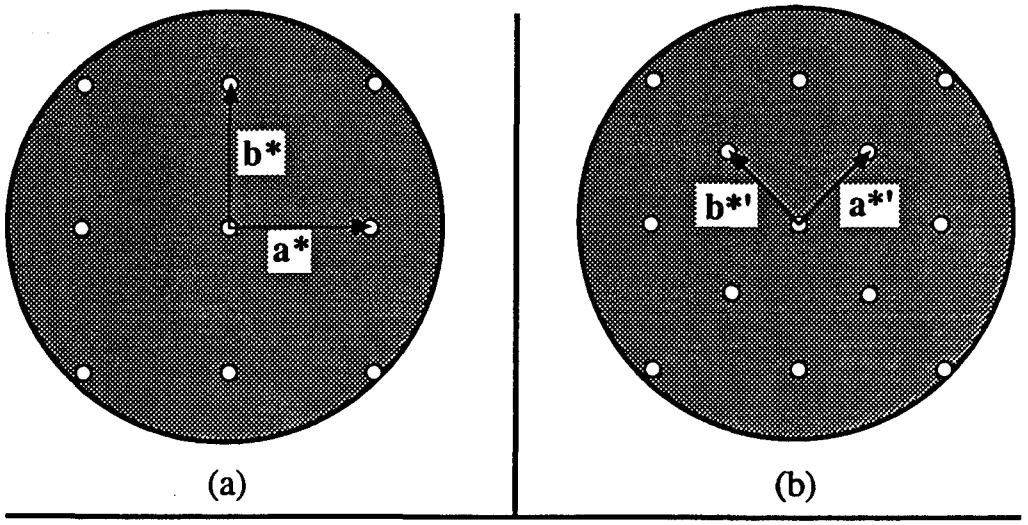

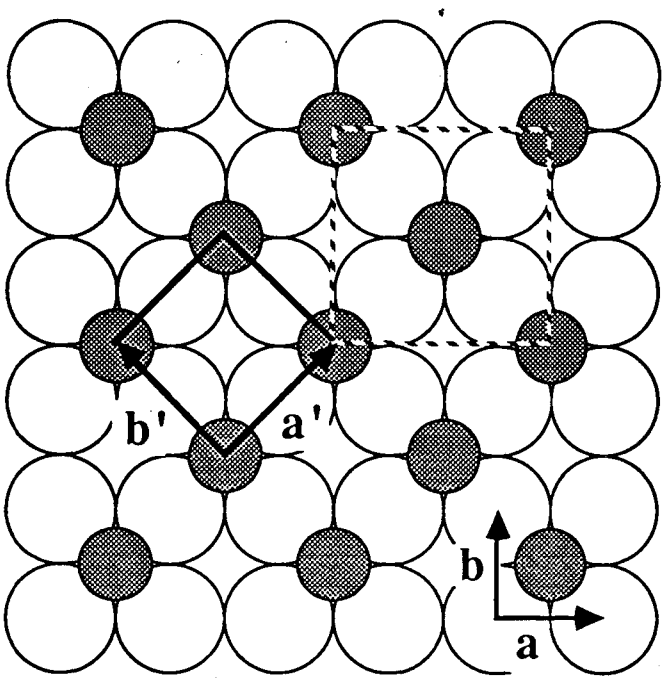

(c)

Inspection of the LEED patterns reveals

$$a^* = a^{*\prime} - b^{*\prime}$$

$$b^* = a^{*\prime} + b^{*\prime}$$

Therefore

$$M^* = \begin{pmatrix} 1 & -1 \\ 1 & 1 \end{pmatrix}$$

$$M = \begin{pmatrix} 1 & 1 \\ -1 & 1 \end{pmatrix}$$

In Real Space

$$a' = a + b$$

$$b' = -a + b$$

Fig. 2.10: Schematic of the clean Rh (100) LEED pattern (a) and with 0.5 mL of adsorbed oxygen (b). The real space unit cells for the two notations ($\sqrt{2}$x-$\sqrt{2}$)R45° (solid lines) and c(2x2) (dashed lines) are shown in (c).

$(\sqrt{2}x\text{-}\sqrt{2})R45°\text{-}O$. The values of n and m are dictated by the following relationships between the superlattice and the substrate lattice unit vectors

$$|\mathbf{a}'| = n\,|\mathbf{a}| \qquad\qquad |\mathbf{b}'| = m\,|\mathbf{b}| \tag{2.11}$$

The label $R\Phi°$ refers to the rotation of the superlattice relative to the substrate lattice.

2.5.4 Mass Spectrometry

Mass spectrometry is utilized to determine the identity of gas phase species in a vacuum system by measuring their atomic mass. Although a considerable range of mass analyzers have been developed, most of them involve either time of flight measurements or the deflection of ions by magnetic and/or electric fields. Currently, the quadrupole mass spectrometer is the most popular mass analyzer for UHV surface science studies.

The quadrupole mass spectrometer consists of three main components as shown in fig. 2.11. The front most component is the ionizer, which typically uses electron bombardment to create ions from the gas phase molecules or atoms. Once created, the ions are injected into the quadrupole mass filter, which uses a varying electric quadrupole field to disperse the ions according to their mass to charge ratio ($^{m}/_{z}$). The final component is the electron multiplier detector, which can be used to detect positive or negative ions, depending on its configuration. Under optimum conditions, gas phase species at partial pressures as low as 5×10^{-13} Torr can

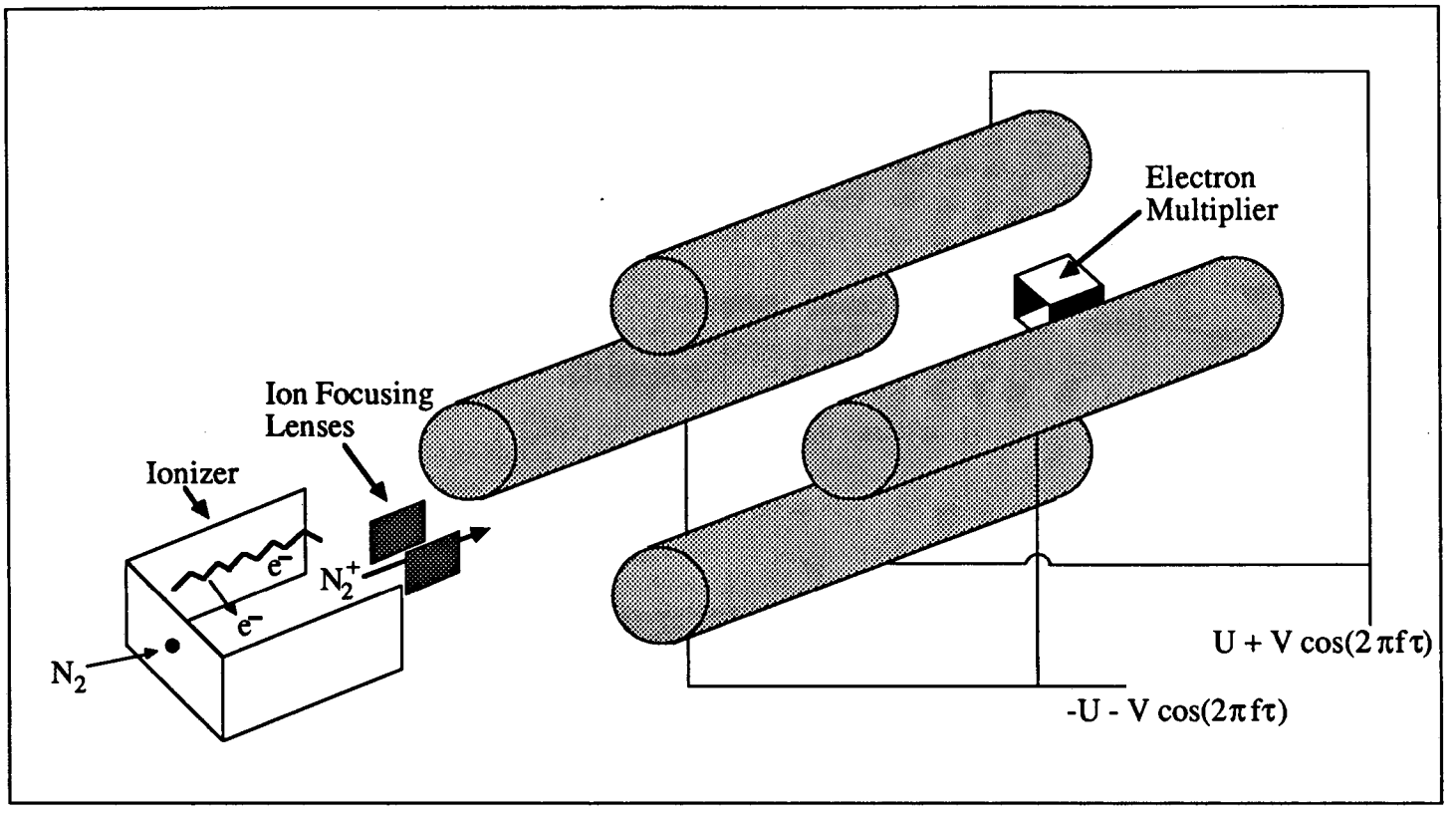

Fig. 2.11: The quadrapole mass spectrometer

be detected with a quadrupole mass spectrometer. A typical mass spectrum of an ion pumped UHV chamber is shown in fig. 2.12.

The ionizers used in these experiments create ions by electron bombardment. The electrons are created by a hot tungsten filament with the emission ranging from 1-50 mA, depending on the gas pressure and mass spectrometer operating parameters. The electrons are typically emitted with a kinetic energy of 70-100 eV in order to maximize their ionizing efficiency. This energy range also minimizes the formation of doubly and triply charge cations and anions. The ionizers are also equipped with a series of electrostatic lenses to focus and inject the ions into the quadrupole assembly.

The quadrupole mass filter employs a time varying electric field produced by a square array of four cylindrical electrodes parallel to the ion injection axis. Opposite electrodes of the assembly are connected together electrically. To one pair of electrodes a potential $f(\tau) = U + V\cos(2\pi f\tau)$ is applied, where U is a D.C. voltage and $V\cos(2\pi f\tau)$ is a radio frequency (R.F.) voltage at frequency f. The same potential is applied to the other pair of electrodes, but with opposite polarity. Under these conditions the equipotential surfaces are symmetric, nearly hyperbolic cylinders with zero potential along the z axis. When an ion is injected into the quadrupole assembly with a motion nearly parallel to the z axis, the R.F. and D.C. electric fields cause it to undergo transverse motion. With the proper selection of U and V, ions of a given (m/z) ratio will have stable trajectories and will emerge from the quadrupole assembly to be detected by the electron multiplier. Ions with other values of (m/z) will have unstable trajectories and will be removed by impact with the electrodes or chamber walls.

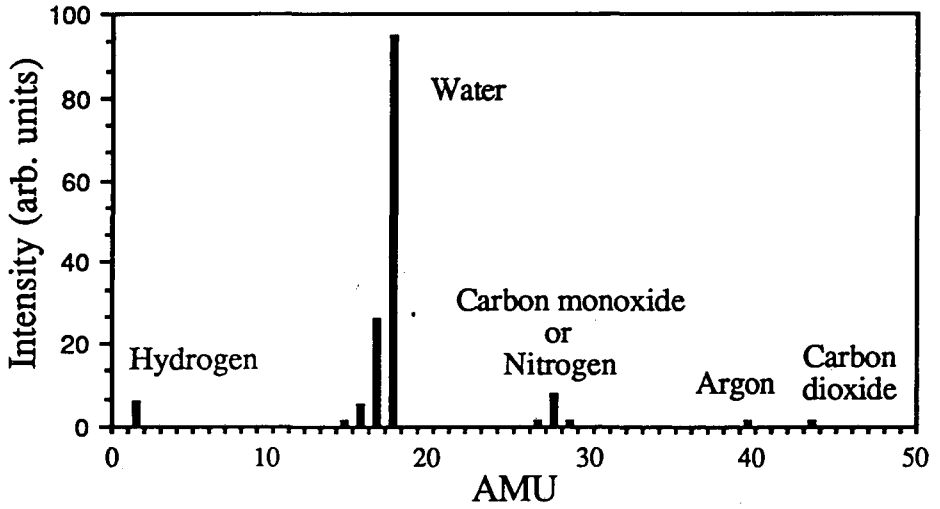

Fig. 2.12: Typical mass spectrum of an ion pumped UHV chamber at 10^{-9} Torr.

2.6 SiC Surface Preparation

The limited chemical reactivity of SiC allows for the relatively easy removal of surface impurities. Before mounting in UHV, the SiC samples used in these experiments were first washed with distilled water, followed by methanol, acetone, and 49% HF to remove the native surface oxide. This treatment usually resulted in a SiC surface with only one or two monolayers of oxide along with submonolayer amounts of other surface contaminates, such as nitrogen, phosphorous, graphite, sodium, chlorine, sulphur and iron. Nitrogen and phosphorous usually appeared only when the SiC was heavily doped. Graphite, sulphur and iron were commonly found in crystals produced by the Acheson process, which is discussed in Section 4.1.

These experiments utilized one of three different methods to produce clean SiC surfaces. The simplest was to heat the SiC sample in UHV to temperatures in the vicinity of 1,300 K, which efficiently removed oxygen, sodium, chlorine and sulphur from the surface. Unfortunately, the process also resulted in the removal of surface silicon via sublimation, which left an amorphous carbon film on the surface of the sample.

The production of clean, well ordered stoichiometric SiC surfaces by Ar^+ ion bombardment,, either at glancing angle or at elevated temperatures, has been only moderately successful. Jørgensen and Morgen found that 3 kV Ar^+ bombardment gave a nearly stoichiometric surface with significant amounts of embedded argon.[27] The embedded argon could only be removed by heating to 1,473 K, which also removed surface silicon, leaving behind graphite. To avoid these problems, Muehlhoff et al. utilized room temperature 500 eV Ar^+ sputtering at 80° off-normal to

clean their α-SiC {0001} surfaces.[3] This method resulted in only small amounts of embedded argon and appeared to restore the stoichiometry of the surface. Although the method removed the long range surface order (i.e. no LEED patterns were obtainable), the tetrahedral sp^3 coordination of the surface atoms remained. Long range surface order may be regained after Ar^+ bombardment, but the process requires extensive post-sputtering annealing in UHV.

The preferred method of SiC surface cleaning now utilized was originally developed by Kaplan.[28] He discovered that surface oxide layers on SiC could be removed easily as low as 1,123 K by exposing the surface to a gallium flux. Kaplan postulates that the oxygen is removed from the surface as Ga_2O. The use of an arsenic molecular beam was found to be equally effective.

For our LEED I-V experiments, the removal of oxide from the β-SiC (100) surface was performed in situ by heating the sample to 1,175 K and placing it in front of a resistively heated silicon wafer at approximately 1,300 K. The flux of silicon atoms obtained from the silicon wafer removed the oxide from the β-SiC surface and also allowed the surface silicon/carbon ratio to be controlled. This allowed us to produce the full range of β-SiC (100) surface reconstructions.

Chapter 3

The Surface Oxidation of α-SiC by O_2

3.1 Introduction

For SiC to fulfill its potential as an electronic material, methods must be developed to produce insulating oxide layers on SiC surfaces in a reproducible fashion. The study of the surface oxidation process should take into account the crystallographic polarity of SiC, since both the surface symmetry and atomic composition depend on the orientation of the surface examined. For α-SiC, the ideal $(000\bar{1})$ basal surface is terminated in carbon atoms, while the (0001) basal surface is terminated in silicon atoms. (fig. 3.1) A method for determining the identity of these two surfaces via chemical etching was developed by Brack using x-ray dispersion effects.[29]

Studies of the high temperature oxidation of the {0001} surfaces by O_2 have shown the two surfaces have significantly different oxidation rates. Harris and Call found that exposing a single crystal of α-SiC to one atmosphere of O_2 for 70 hours at 1,333 K produced 900 Å of SiO_2 on one basal surface, and 6,500 Å on the other.[30] Suzuki et al. found very similar results for the oxidation of α-SiC.[16] Exposure of α-SiC at 1,273 K to H_2O saturated O_2 (P= 1 atm) for two hours produced 152 Å SiO_2 on the (0001) surface, 908 Å SiO_2 on the $(000\bar{1})$ surface, and for comparison, 1949 Å SiO_2 on a Si (111) surface.

Fig. 3.1: Ideal SiC single crystal structure.

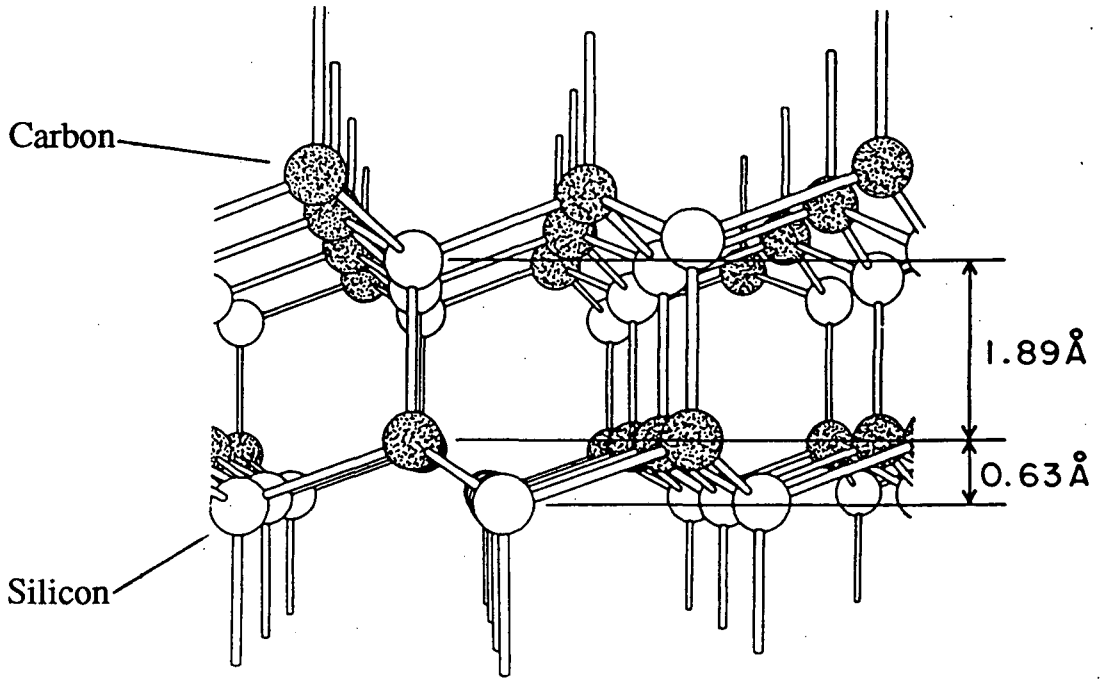

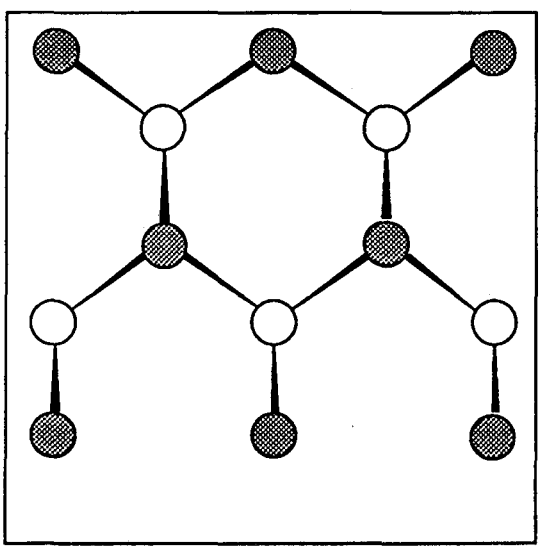

The ideal alpha-SiC ($000\bar{1}$) surface.
Topmost layer: carbon

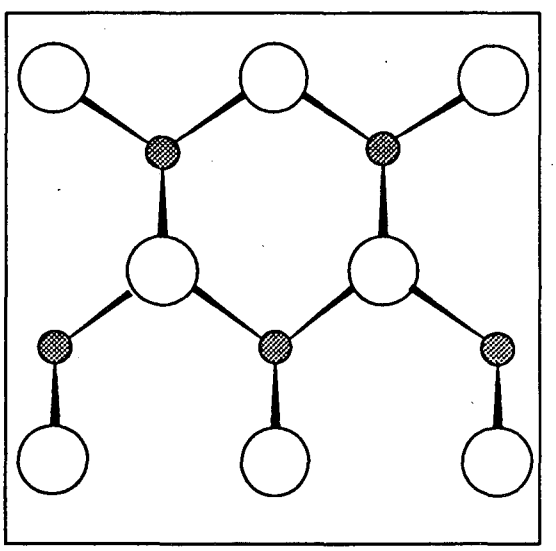

The ideal alpha-SiC (0001) surface.
Topmost layer: silicon

While these studies provide valuable information on the macroscopic oxidation of α-SiC, they are unable to address the questions of surface composition and structure during the initial stages of oxidation. Muehlhoff and coworkers utilized a combination of XPS, AES, and energy-loss spectroscopy (ELS) to analyze the {0001} surfaces of α-SiC as a function of temperature and O_2 exposure.[3,31] In UHV both {0001} surfaces showed carbon enrichment of the surface region at elevated temperatures. The $(000\bar{1})$ surface showed enrichment as low as 900 K, while the (0001) surface composition was stable up to 1,300 K, at which point surface graphitization took place. This graphitization process at 1,300 K occurred on both surfaces and was attributed to silicon sublimation from the surface region. Surface carbon enrichment appeared to be an important factor in the oxidation of the {0001} surfaces by O_2. Utilizing an O_2 exposure pressure of 54 mTorr, Muehlhoff et al. compared the oxidation rates of both surfaces at 995 K and 1,345 K. At both temperatures, the $(000\bar{1})$ surface oxidized at a faster rate than the (0001) surface. However, for short O_2 exposure times the extent of oxidation on both surfaces was less at 1,345 K than at 995 K. At 1,345 K, graphite from the thermal decomposition of α-SiC covered both {0001} surfaces. The authors proposed that once this graphite was removed by a sufficient exposure to O_2, a second oxidation process took over with a much higher rate than that was seen at 995 K. For both {0001} surfaces, no evidence of C-O surface bonding was observed.

This chapter details our study of the surface oxidation process of single crystal α-SiC by O_2 from the initial stages of oxide growth to the production of thick oxide layers. Utilizing AES, XPS and LEED, we explored the α-SiC surface composition in UHV as a function of

temperature. The interaction of the basal surfaces of α-SiC with O_2 at 10^{-8} Torr was explored, and surface graphitization due to SiO and Si sublimation is discussed. The effect of surface roughness on the rate of oxidation was also examined. The relatively slow oxidation of an ordered $(000\bar{1})$ surface at elevated temperatures is attributed to the crystallographic orientation of the surface and a lack of sites suitable for oxygen bonding.

The production of thick SiO_2 layers obtained at high O_2 partial pressures was examined using SAES and SEM. To study the effect of surface polarity on the production of thick SiO_2 overlayers, multiple α-SiC samples at 1,323 K were exposed to 1 atm of flowing O_2 for one hour. For all the crystals utilized, the $(000\bar{1})$ surface produced thicker oxide layers than the (0001) surface under identical conditions. However, the difference between the two surfaces was considerably less than previously reported and also appeared to be sample dependent. In addition, the thickness of the SiO_2 layer on each basal surface varied over the exposed surface area of the crystal.

3.2 Experimental

Three UHV chambers were used for the α-SiC surface analysis. The Varian chamber utilized for AES, LEED, and mass spectroscopic analysis is shown in fig. 3.2. The α-SiC crystals were mounted on an off-axis manipulator and were heated either resistively or by electron bombardment. Surface cleaning was performed with glancing angle 400 eV Ar^+ bombardment with simultaneous annealing, yielding clean surfaces with the exception of small amounts of embedded argon. After cleaning, the surfaces were exposed to O_2 by backfilling the entire chamber with a

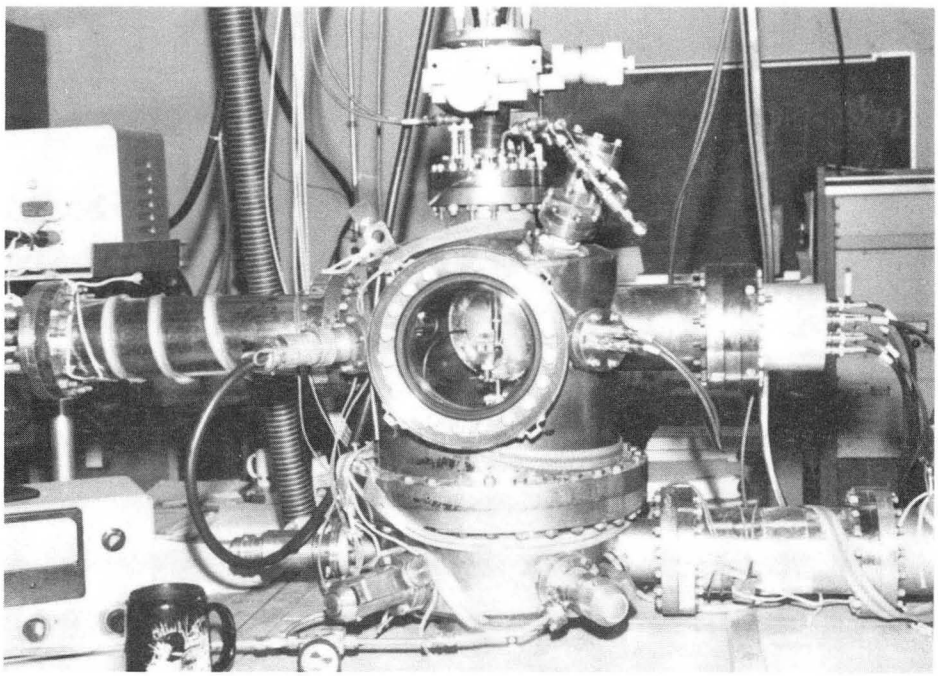

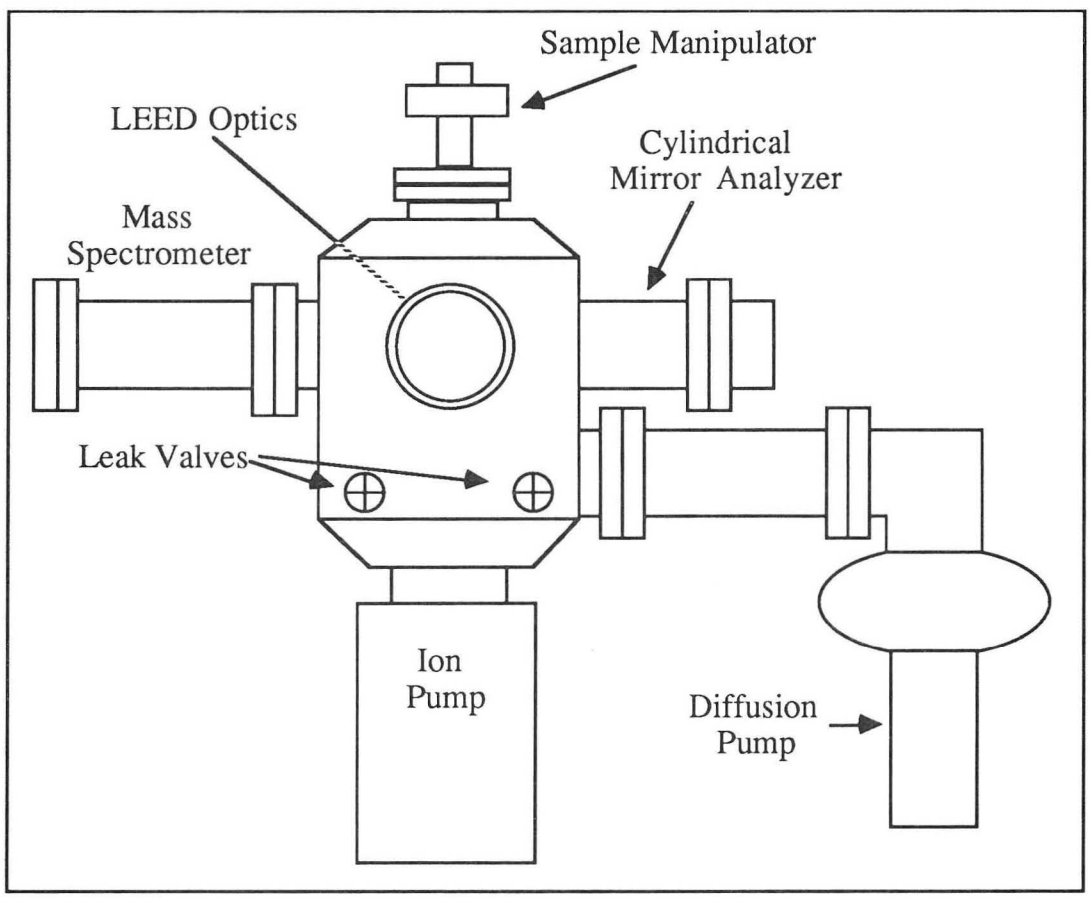

Fig. 3.2: Photo and Schematic of the Varian UHV chamber used for AES, LEED and mass spectrometric analysis.

Varian leak valve. The O_2 exposure was measured in Langmuirs (1 Langmuir = 10^{-6} Torr·sec) with the chamber pressure being read with an uncorrected ion gauge. A PHI single pass cylindrical mirror analyzer was used for AES with a primary beam energy of 1500 eV. Consecutive AES scans yielded peak to peak intensities that were reproducible within 3%. A PHI 4-grid LEED/Auger optics system was utilized for LEED studies, and the residual gas load of the chamber was analyzed with an Extrel quadrupole mass spectrometer.

The second chamber utilized was a PHI 5300 ESCA system, which was used for XPS studies. The system is equipped with a hemispherical energy analyzer (37.75 eV pass energy) and both Mg and Al x-ray sources. Sample cleaning was performed by 3 kV Ar^+ bombardment at room temperature.

To produce thick oxide layers on the α-SiC crystals, they were exposed to 1 atm of flowing O_2 in a quartz tube furnace. The crystals were placed into the preheated tube, the tube was pumped to 10^{-4} Torr with a turbomolecular pump, and then O_2 was flowed into the system at approximately 200 cm^3/minute.

A PHI 660 Scanning Auger Multiprobe was utilized for the SAES and SEM studies of the oxide layers on α-SiC produced via O_2 exposure at 1 atm. The electron beam (Ep = 3 kV) was focused to a spot size of approximately 1 μm^2 for the AES and SEM analysis. Images of the oxide layer with a magnification of greater than 400x were unattainable via SEM due to charging in the oxide layer. Argon ion depth profiling was performed at 5 kV over a rastered 3 mm x 3 mm area. Both basal surfaces of each crystal were analyzed with each surface being analyzed in 3 separate areas. Multiple analysis areas were utilized to check the

uniformity of the surface oxide layer. The average of these values is reported as the oxide thickness. It was assumed the SiO_2/SiC interface had been reached when the oxygen AES intensity decreased to one half its value in the SiO_2 bulk. The Ar^+ ion sputter rate was calibrated by measuring the time required to remove a known thickness of SiO_2 from a polished Si (111) wafer. The SiO_2 thickness on the Si (111) wafer was first determined by ellipsometry and interferometry. After the experiments the orientation of the α-SiC basal surfaces [$(000\bar{1})$ vs. (0001)] was determined by etching the crystals for 10 minutes in molten Na_2CO_3 at 1,220 K. After etching, an examination of the (0001) surface with an optical microscope revealed numerous distorted hexagonal etch pits, while the $(000\bar{1})$ surface appeared worm-eaten, as shown in fig. 3.3.

For the AES/LEED studies the crystals were rinsed with distilled water, methanol, acetone, and 49% HF before mounting in UHV. To avoid charging during electron or Ar^+ bombardment the crystals were usually attached to tantalum using a 90% Au/10% Ta alloy. A 0.1 mm foil of the alloy was placed between the α-SiC crystal and the tantalum substrate, and then the entire arrangement was heated to approximately 1,600 K in vacuum for 5 minutes. This melted the alloy and provided an ohmic contact between the α-SiC and tantalum substrate. The temperature of the crystal was determined with a chromel-alumel thermocouple. The thermocouple was spotwelded to a piece of 0.1 mm tantalum foil. The thermocouple and foil were either mechanically held against the crystal surface or were bonded to the crystal surface using the Au/Ta alloy.

Two types of single crystal α-SiC samples were utilized in the experiments. Crystals prepared in commercial furnaces used for the manufacturing of SiC abrasive were obtained from Atomergic Chemetals

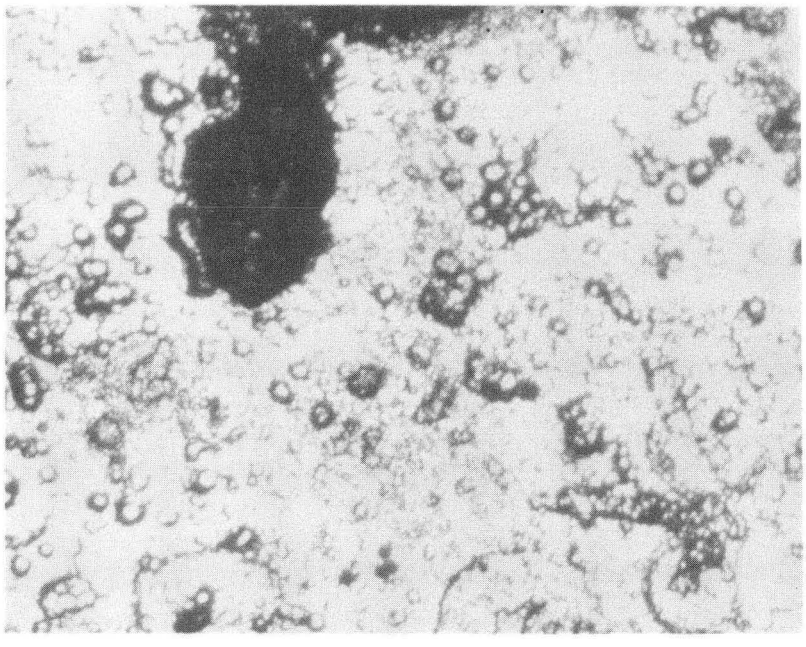

The (0001) Surface

The $(000\bar{1})$ surface

Fig. 3.3

Company. These crystals will be referred to as the "commercial" samples. Due to the poor crystallinity of these samples, no LEED diffraction patterns were obtainable. Higher quality α-SiC crystals provided by W. J. Choyke were also utilized in these experiments.[a] Produced by the Lely method, these crystals were n-type semiconductors and the basal surfaces provided LEED patterns without any mechanical polishing.

The extent of surface oxidation was determined by measuring the peak to peak heights (I(X)) of the differentiated Si(LVV), C(KLL), and O(KLL) AES signals. The Si(LVV) transition was chosen since it is most sensitive to the presence of surface oxygen. In SiC, the Si(LVV) AES transition produces an intense peak at 89 eV. As oxygen bonds to the SiC surface, I(Si) declines monotonically. In SiO_2, this 89 eV peak is reduced to just a shoulder on the main LVV peak at 76 eV. Information about the carbon bonding environment (graphitic vs. carbidic) can be obtained from analysis of the C (KLL) AES lineshape. Carbon in graphite exhibits a peak at 240 eV, while carbon in α-SiC exhibits peaks at 247 and 253 eV.

3.3 Results

3.3.1 Surface Composition of α-SiC as a Function of Temperature and O_2 Pressure

A) Ultrahigh vacuum

The α-SiC $(000\bar{1})$ surface composition was examined as a function of temperature from 300 K to 1,273 K. (fig. 3.4) Room temperature 400

---

[a] Dept. of Physics, University of Pittsburgh, PA.

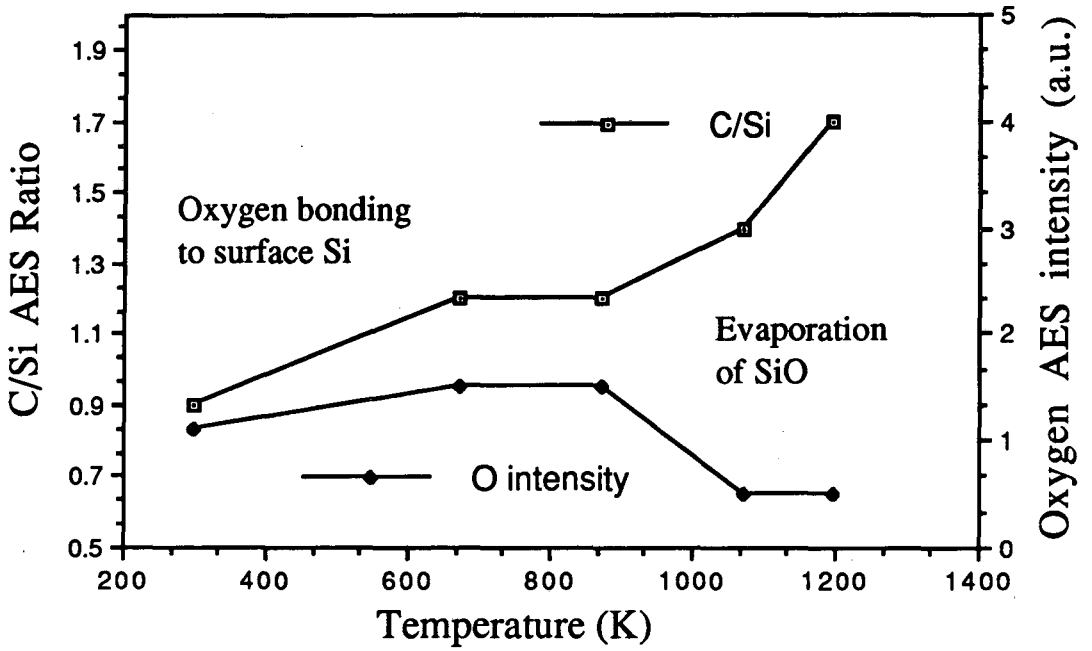

Fig. 3.4: The α-SiC (000$\bar{1}$) surface composition in UHV as a function of temperature

eV Ar^+ bombardment produced a disordered surface with an I(C)/I(Si) AES ratio of 0.90 and trace amounts of surface oxide. Heating to 673 K for 5 minutes increased the ratio to 1.20 due to adsorption of oxygen on the surface, which caused a decrease in the silicon 89 eV AES intensity. The source of this surface oxygen appeared to be background H_2O and/or O_2 in the UHV system. Five minutes of heating at 1,073 K increased the I(C)/I(Si) ratio to 1.40 and removed most of the surface oxide, suggesting SiO_x sublimation from the surface. Mass spectral analysis showed an increase in the 44 amu signal, which was attributed to SiO. Heating to 1,198 K for two minutes increased the I(C)/I(Si) ratio to 1.70 with no increase in the oxygen AES intensity. At both 1,073 K and 1,198 K AES showed an increase in signal at approximately 240 eV, indicating graphite formation. Raising the temperature to 1,273 K for 15 min. resulted in the complete removal of silicon from the surface region according to AES. The acceleration of the surface graphitization at this temperature was attributed to Si sublimation from the surface region.

B) 10^{-8} Torr of O_2

The initial growth of oxide on α-SiC was examined at 300 K using an O_2 pressure of 10^{-8} Torr. Prior to O_2 exposure, the sample was Ar^+ sputtered at 940 K and then annealed for 15 minutes at 880 K. Exposure to O_2 produced a monotonic decline in the silicon and carbon AES intensities. (fig. 3.5) Lineshape analysis of the silicon and carbon AES signal after O_2 exposure showed the adsorbed oxygen was bonded to surface silicon atoms, not carbon. The intensity of the Si 89 eV AES transition after O_2 exposure showed the surface oxide produced was not SiO_2; however, AES was unable to determine the exact nature of the oxide. (fig. 3.6) The decrease

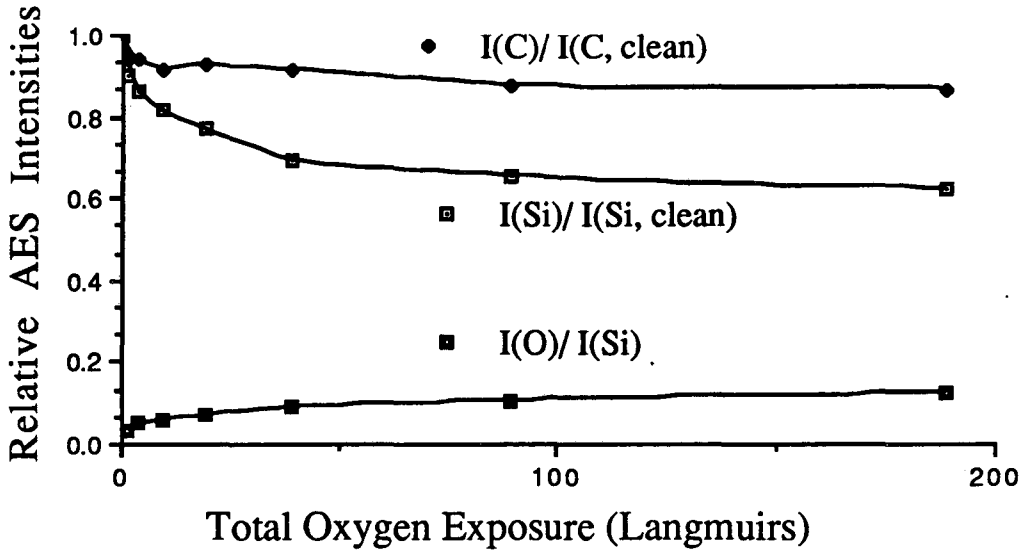

Fig. 3.5: Variation in the AES intensities of α-SiC as a function of O_2 exposure at 300 K.

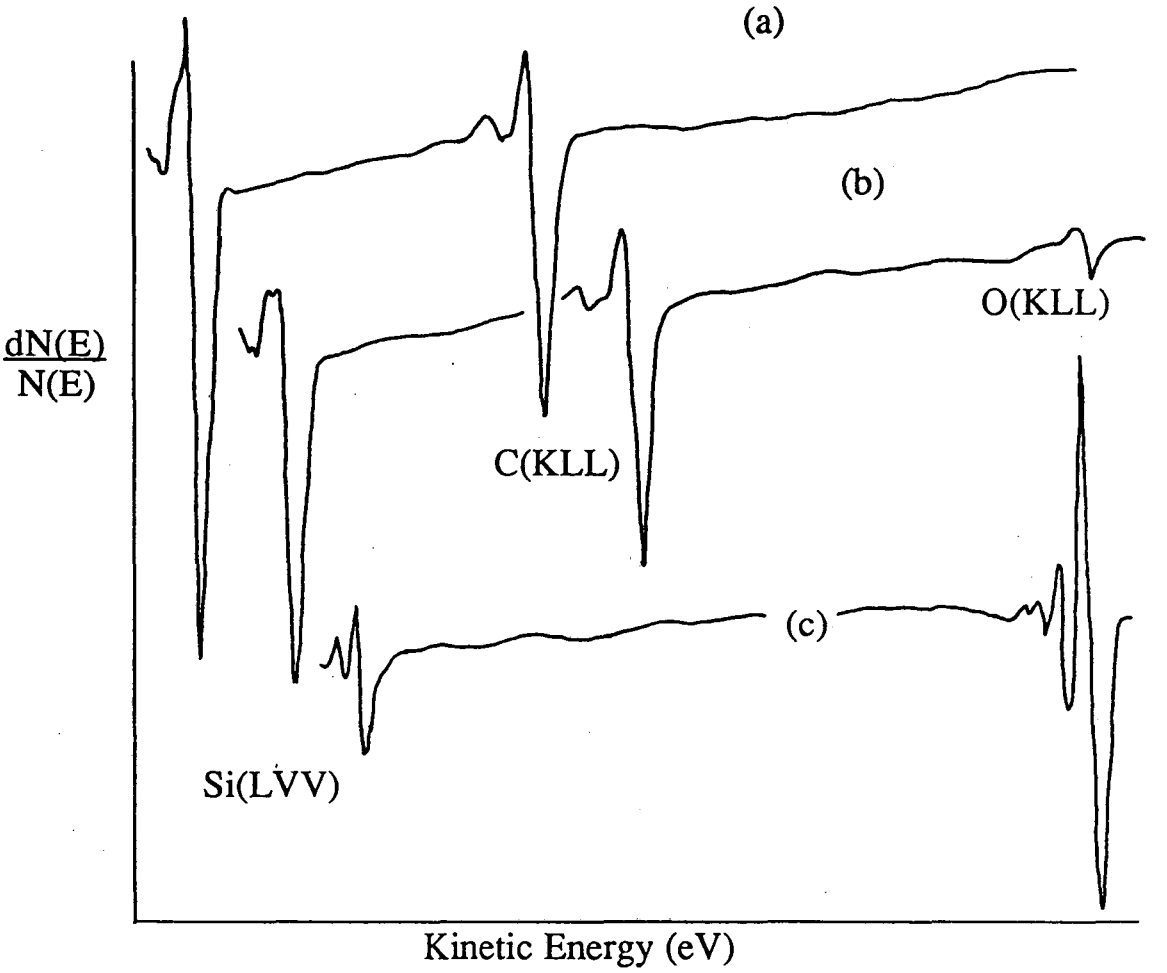

Fig. 3.6: AES spectra of a) clean α-SiC, b) after 190 L O_2 exposure at 300 K and c) clean SiO_2

in the Si 89 eV AES intensity showed the surface exhibited a relatively fast initial rate of oxygen adsorption, but then showed a slower adsorption rate with increasing O_2 exposure. The experiment repeated at temperatures up to 833 K produced similar results to those found at 300 K. At all temperatures examined, the α-SiC surface appeared to approach a submonolayer oxidation limit with increasing O_2 exposure. In all cases the temperature during O_2 exposure was low enough such that surface graphitization did not occur due to Si and SiO sublimation. Heating the sample to 1,100 K in UHV after O_2 exposure removed the surface oxide via SiO sublimation, leaving behind surface graphite.

C) 1 atmosphere of O_2

X-Ray photoelectron spectroscopy was utilized to better determine the nature of the initial oxide formed on α-SiC by O_2 exposure. Alpha SiC cleaned by 3 kV Ar^+ bombardment at room temperature exhibited a C 1s and Si 2p binding energy (B.E.) of 283.0 and 100.0 eV, respectively. Oxidation of the sample was performed by exposure to air for 25 minutes at room temperature. After exposure, the Si 2p peak showed a higher binding energy shoulder, attributed to the presence of oxidized silicon. A computer fitting of the experimental results assumed two types of silicon; oxidized and non-oxidized. (fig. 3.7) The oxidized silicon exhibited a 2p B.E. of 100.8 eV, which is too low to be SiO_2 (Si 2p B.E. = 103.4 eV).[26] The oxygen bonding to the α-SiC surface created a silicon oxidation state similar to that found in hexamethyldisiloxane ($(CH_3)_3SiOSi(CH_3)_3$; Si 2p B.E. = 100.9 eV).[26] In this compound, oxygen is bonded between two silicon atoms, which are in turn bonded to 6 carbon atoms. This type of Si-O-Si bonding is a reasonable model for the initial oxide found on α-SiC.

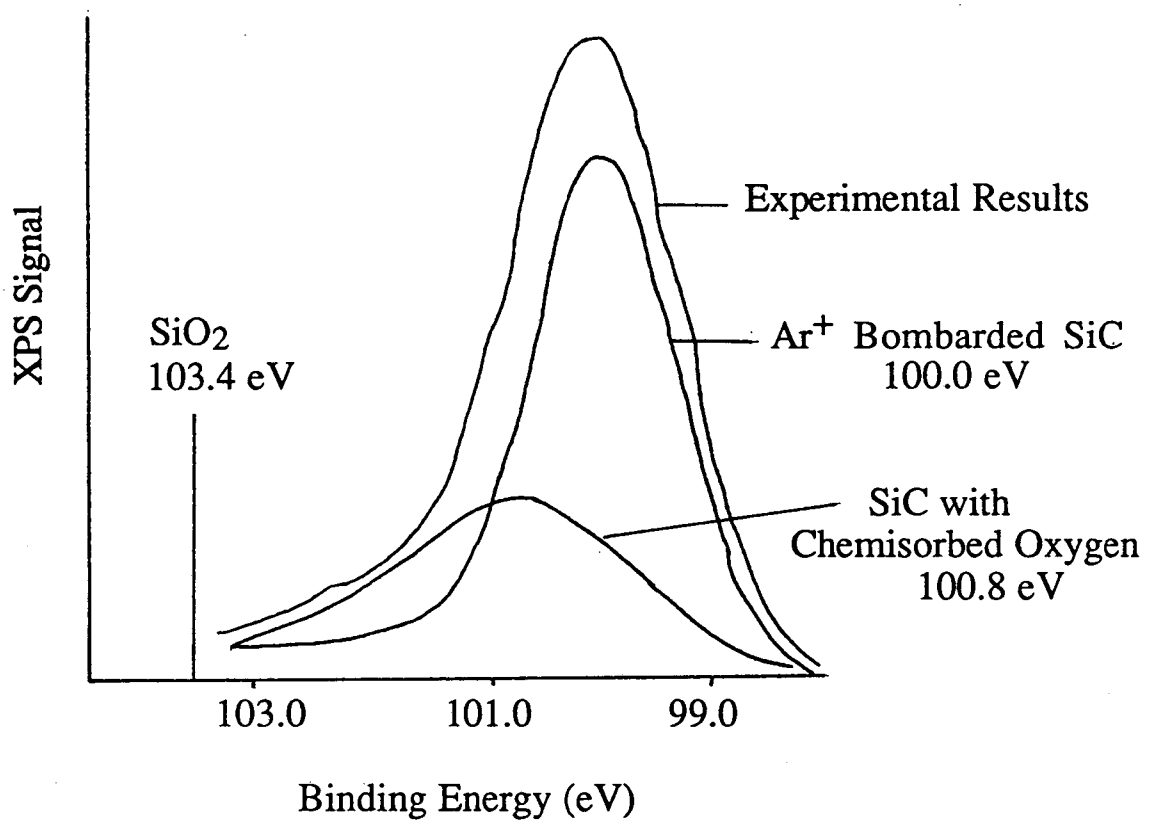

Fig. 3.7: The Si 2p B.E. peak after exposing the sputtered α-SiC to air for 25 minutes. The position of the peak maximum for SiO_2 is also shown.

The composition of the {0001} surfaces of an α-SiC single crystal was examined via SAES after exposure to 1 atm of O_2 at various temperatures. Figure 3.8 shows the composition of the (0001) surface after one hour O_2 exposure at several temperatures. Exposure to O_2 at 300 K and 573 K did not produce surface SiO_2, while O_2 exposure from 873 K to 1,373 K did produce SiO_2. As expected, the average SiO_2 thickness increased with increasing temperature (120 Å SiO_2 at 873 K vs. 1250 Å SiO_2 at 1,373 K). The presence of carbon within the SiO_2 layer was not detected by SAES. At each temperature examined, no significant difference in surface composition existed between the (0001) and $(000\bar{1})$ surfaces of the crystal. However, the SiO_2 overlayer produced on the $(000\bar{1})$ surface was 1.3 times thicker on average than the SiO_2 layer on the (0001) surface.

In order to determine if the difference in oxidative behavior seen between the {0001} surfaces was sample dependent, four α-SiC samples (2 Lely, 2 commercial) were exposed to 1 atm of flowing O_2 at 1,323 K for one hour. It was found with each crystal that the $(000\bar{1})$ surface produced, on average, a thicker SiO_2 layer than the (0001) surface under the same conditions. However, the difference in oxide thickness between the two surfaces of the same crystal was far less dramatic than reported by Harris and Call. As table 3.1 shows, the thickness of the oxide produced and the difference between the two {0001} surfaces also appeared to be sample dependent. Argon ion depth profiling coupled with SAES revealed the SiO_2 thickness could vary considerably over each basal surface. No obvious differences between the Lely and commercial samples were observed.

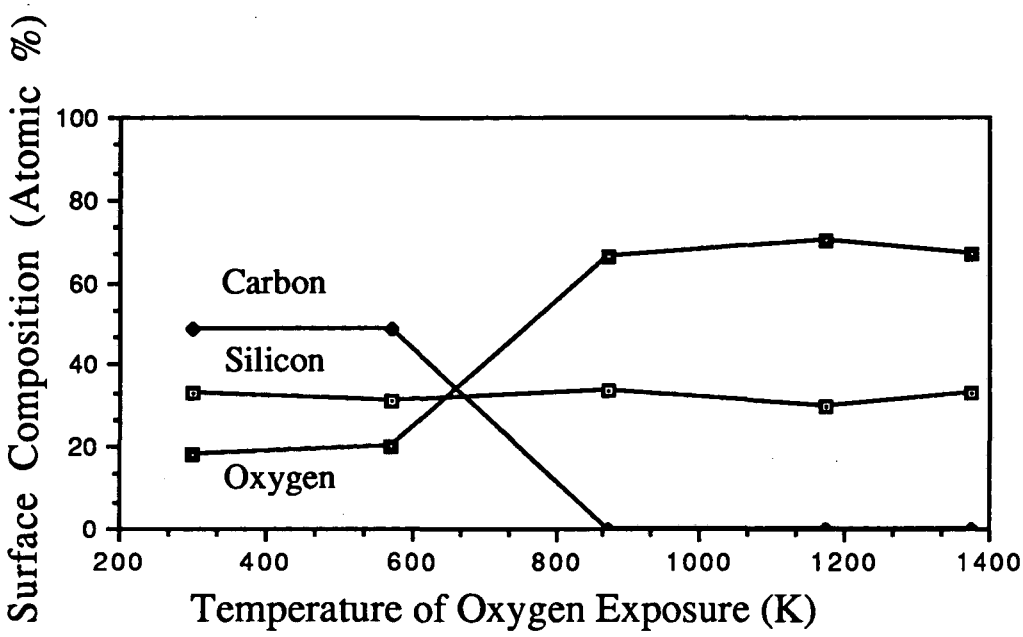

Fig. 3.8: The α-SiC (0001) surface composition after exposure to 1 atm O_2 for 1 hour at various temperatures

Table 3.1: Oxidation of α-SiC: 1 atm O_2, 1323K, 60 min

Crystal	Surface	Oxide Thickness (Å) by AES Depth Profiling		
		Ave.	Crystal Edge	Center of Crystal
α-SiC #1	$(000\bar{1})$	820	890	760
	(0001)	390	410	330
α-SiC #2	$(000\bar{1})$	720	740	770
	(0001)	290	320	280
α-SiC #3	$(000\bar{1})$	840	760	950
	(0001)	540	480	600
α-SiC #4	$(000\bar{1})$	780	820	740
	(0001)	640	820	460
Si	(111)	1270		

3.3.2 The Role of Surface Defects in Oxidation of α-SiC by O_2

The results cited above suggest that the polarity of the α-SiC {0001} surfaces alone is not as dominating a factor for O_2 oxidation as previously reported. In order to explore how sample annealing prior to 10^{-8} Torr O_2 exposure affects the interaction of O_2 with α-SiC, two different surface preparations with the same commercial α-SiC crystal were utilized. In case 1), the sample was sputtered at 923 K for 15 minutes, quickly cooled to 773 K, and then exposed to O_2. This will be referred to as the nonannealed surface. In case 2), the sample was sputtered under identical conditions, annealed in UHV at 923 K for 15 minutes, then cooled to 773 K and exposed to O_2. This will be referred to as the annealed surface.

The sputtered, nonannealed surface reacted with O_2 more extensively than the sputtered, annealed surface, as illustrated in fig. 3.9. Interestingly, the carbon AES intensity of the nonannealed surface (not shown in fig. 3.9) showed a 26% decline with only 6 L O_2 exposure. This abrupt decline indicated Ar^+ sputtering produced reactive surface carbon that was removed to the gas phases by O_2. The reactivity of this carbon appeared to be removed during annealing at 923 K. In both cases the surface still showed a two-stage oxidation process similar to that seen with O_2 exposure of α-SiC at 300 K.

The interaction of an ordered $(000\bar{1})$ surface with O_2 was examined at 973 K. This temperature was chosen to maximize the surface oxidation rate while simultaneously avoiding SiO sublimation from the surface region. Exposure of the ordered (1x1) surface to 10^{-8} Torr O_2 produced much slower surface oxidation than seen with the poorer quality crystals

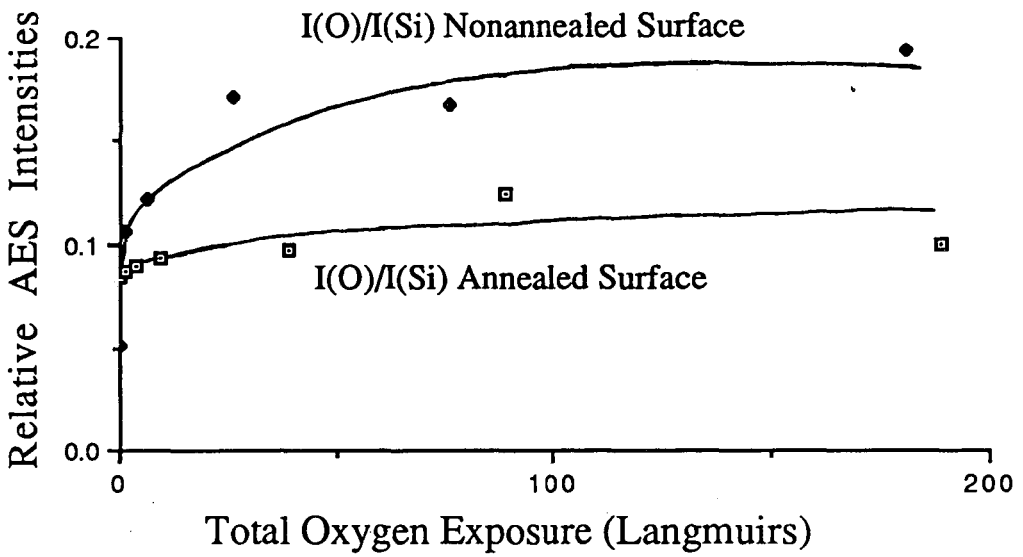

Fig. 3.9: Variation in the I(O)/I(Si) AES ratio of α-SiC as a function of O_2 exposure at 773 K. Note than sample annealing in UHV after Ar^+ sputtering reduces the chemisorption of surface oxygen.

used previously. After 6,700 L O_2 the silicon and carbon AES intensities had declined 22% and 11%, respectively. (fig. 3.10) The (1x1) LEED pattern did not change with O_2 exposure; rather, it became sharper due to annealing at 973 K during the O_2 exposure. This result suggested oxygen was bonding on steps or other defects.

3.4 Discussion

3.4.1 Surface Composition of α-SiC as a Function of Temperature and O_2 Pressure

The UHV composition of the sputtered α-SiC $(000\bar{1})$ surface as a function of temperature changed due to surface oxide formation and sublimation of Si and SiO. Room temperature Ar^+ sputtering roughened the surface, making it highly susceptible to oxidation by background O_2 and/or H_2O. Lineshape analysis of the silicon AES signal showed that the oxide formed was not SiO_2. The surface oxide began to be removed at approximately 1,100 K due to SiO sublimation from the surface region, which left behind graphitic surface carbon. At 1,100 K, the overall silicon AES intensity decreased, but analysis of the peak lineshape showed the silicon remaining on the surface was bonded to considerably less oxygen than before. This showed the changes in I(C)/I(Si) and I(O) were not due simply to a deposition of carbon on the surface. The sublimation of SiO at approximately 1,100 K has also been proposed and utilized by Kaplan as a method of removing surface oxide from SiC.[32] The graphitization of the surface was further accelerated at 1,273 K due to silicon sublimation from

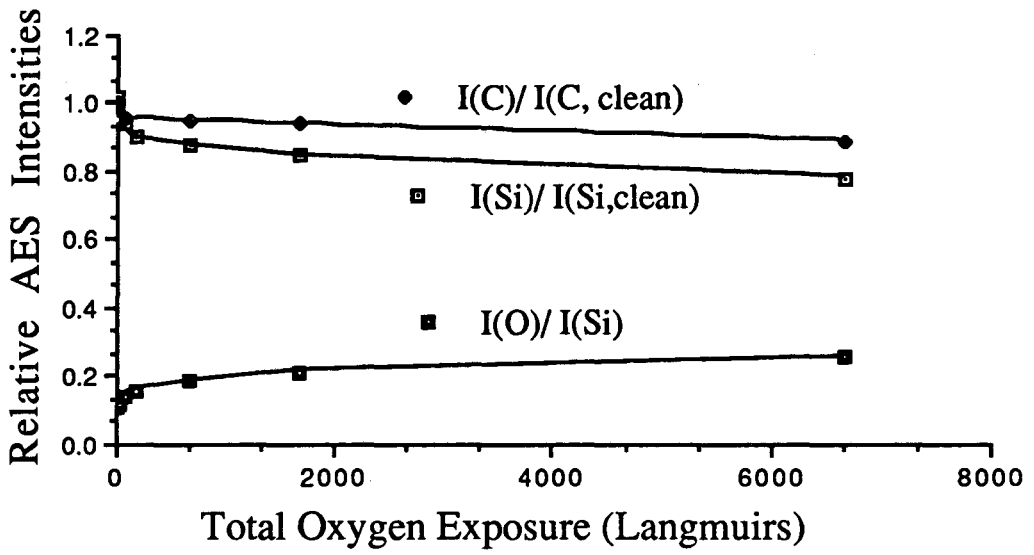

Fig. 3.10: Variation in the AES intensities of an ordered α-SiC (000$\bar{1}$)-(1x1) surface as a function of O_2 exposure at 973 K.

the surface region. Mass spectroscopic studies of the high temperature decomposition of α-SiC have shown that $Si_{(g)}$ is clearly the dominate species found over α-SiC at thermodynamic equilibrium.[33] The $Si_{(g)}$ is produced via the reaction

$$\alpha\text{-SiC} \text{----}> Si_{(g)} + C_{(graphite)} \quad \Delta H^{\circ}_{298} = 125\ ^{kcal}/_{mole} \qquad (3.1)$$

It is believed that as the graphite layer increases in thickness, the diffusion of silicon from the bulk to the surface dominates the sublimation process.

For comparison, Muehlhoff et al. reported that the surface composition of a sputtered $(000\bar{1})$ surface was stable up to 900 K, at which point carbon enrichment of the surface region took place. Further graphitization occurred at 1,300 K due to silicon sublimation from the surface region. One possible explanation for the differences in our results is that Muehlhoff's studies were done with a lower chamber pressure ($P<10^{-9}$ Torr vs. $P=2x10^{-9}$ Torr), which would slow the formation of surface oxides.

Exposure of sputtered, annealed α-SiC to 10^{-8} Torr O_2 from 300 K to 833 K produced a submonolayer surface oxide. In all cases the surface showed a two-stage oxidation process; a fast initial reaction with O_2 followed by a slower oxidation process with increasing O_2 exposure time. This type of oxygen adsorption has also been observed on single crystal Si (111) [34] and on room temperature α-SiC (0001).[27] At these temperatures, the O_2 exposure did not produce SiO_2 and surface graphitization due to Si and SiO sublimation did not occur. Heating this submonolayer surface oxide to 1,100 K in UHV removed the oxide via SiO sublimation, leaving behind graphitic surface carbon.

$$\alpha\text{-SiC} + {}^{1}/_{2}\, O_2 \text{------}> SiO_{(g)} + C_{(graphite)} \qquad (3.2)$$

The inability to obtain any LEED results from the basal surface used in these experiments indicated the surface was completely disordered. The orientation of the surface was not determined via Na_2CO_3 etching, since the oxidation results could not be attributed to a specific surface structure.

While α-SiC in low O_2 pressures and at elevated temperatures exhibits surface graphitization, the exposure of α-SiC to air or 1 atm O_2 produces surface silicon oxide (SiO_x) layers. Exposure of Ar^+ sputtered α-SiC to air for 25 minutes produced oxidized silicon with a fitted Si 2p B.E. of 100.8 eV, which suggested oxygen atoms were bridging surface silicon atoms. The model that the oxygen was bridging two silicon atoms, which were in turn bonded to carbon was based on a comparison of our results to reported XPS results for various organosilicon compounds. This type of bridging oxygen has also been proposed with single crystal Si [35] and β-SiC.[36] These binding energies are independent of the surface orientation utilized, since it appears that Ar^+ bombardment at room temperature disorders the surface, removing the "memory" of the surface polarity.

The production of SiO_2 from α-SiC and O_2 is extremely exothermic

$$\alpha\text{-SiC} + {}^3/_2\, O_2 \text{---->} SiO_{2\,(amorphous)} + CO \qquad (3.3)$$
$$\Delta H^\circ_{298} = -227\ {}^{kcal}/_{mole}$$

Therefore, the often cited resistance of SiC to oxidation should be attributed to kinetic factors. In our experiments, exposure of α-SiC {0001} surfaces to 1 atm O_2 for 1 hour at 300 K and 573 K did not produce SiO_2, while SiO_2 was produced from 873 K to 1,373 K. The thickness of the SiO_2 surface layer produced in one hour on both {0001} surfaces increased with oxidation temperature. Carbon was not detected by

SAES in the SiO_2 surface layers. This is consistent with previous gas chromatographic results, which suggested CO and/or CO_2 gas are the only C/O species formed during SiC oxidation in O_2 or air.[37] It has been proposed that with thicker SiO_2 surface layers, the diffusion of the by-product CO through the SiO_2 layer determines the overall oxidation rate.[16]

The exposure of four different α-SiC crystals at 1,323 K to 1 atm of flowing O_2 for one hour produced a wide range of surface oxide thicknesses. On each crystal the $(000\bar{1})$ surface produced a thicker SiO_2 surface layer than the (0001) surface. However, the difference between the two {0001} surfaces appeared sample dependent. In addition, the thickness of the SiO_2 layer on each basal surface varied over the area of the surface. These results suggest that the crystallographic polarity of α-SiC alone does not dominate the oxidation of the {0001} surfaces as significantly as previously reported.

It is reasonable to expect that an ideal, C-terminated $(000\bar{1})$ surface of α-SiC would show different oxidation characteristics than an ideal, Si-terminated (0001) surface during the growth of the first oxide layer. This could be attributed to the fact that oxygen bonded to the surface of SiC bonds only to silicon, not to carbon. However, it is expected that as the oxide layer increases in thickness, the sharpness of the SiO_2/SiC interface would be diminished. This would lead to the production of a Si/C/O interfacial region between the SiO_2 overlayer and the SiC substrate. Once this Si/C/O interface forms, the "memory" of the underlying crystal polarity is lost, and the two {0001} surfaces would be expected to produce SiO_2 layers of similar thickness under identical oxidative conditions.

The question remaining is why different α-SiC crystals produce SiO_2 layers of significantly different thicknesses and uniformity under identical high temperature O_2 exposures. Our work has shown that the oxidation of α-SiC surfaces is enhanced by the presence of surface defects. One possible explanation for the different oxidation characteristics of the {0001} surfaces is that as-grown $(000\bar{1})$ surfaces possess a higher density of steps, kinks, or other defects than as-grown (0001) surfaces. This would cause the $(000\bar{1})$ surface to oxidize faster than the (0001) surface initially, but would not be a significant factor as the oxide layer increased in thickness. In addition, if the density of defects was not uniform across a basal surface, it is reasonable to conclude the SiO_2 layer produced on that surface would not be uniform.

3.4.2 The Role of Surface Defects in the Oxidation of α-SiC by O_2

The studies performed at 773 K showed that sputtered α-SiC surfaces exhibited a fast initial reaction with O_2, but then a slower oxidation process took over with increasing O_2 exposure time. The surfaces that were not annealed after Ar^+ bombardment were found to oxidize faster and more extensively than surfaces that did receive post-sputtering annealing. These nonannealed and presumably more disordered surfaces still showed a two-stage oxidation process with O_2 at 10^{-8} Torr. Argon ion bombardment produced highly reactive surface carbon, the reactivity of which was reduced by post-sputtering annealing. The susceptibility of SiC to ion bombardment damage has been documented. Studies of SiC subjected to 10 kV He^+ bombardment at room temperature

have shown that SiC becomes flaky and porous on a micron scale, while SiC at 870 K does not show bombardment damage.[38]

The importance of surface defects in the oxidation of α-SiC by O_2 was shown by the interaction of O_2 with an ordered $(000\bar{1})$ surface at 973 K. This ordered surface showed far less reactivity towards O_2 than the sputtered, disordered surfaces discussed previously. The low reactivity can be attributed in part to the fact that oxygen bonded to the surface of SiC bonds only to silicon atoms. In an ideal $(000\bar{1})$ surface, the topmost silicon atoms are in the second atomic layer and have no unsaturated bonds. Hence, the $(000\bar{1})$ surface would not be expected to react extensively with O_2. This is supported by the fact that the (1x1) LEED pattern was not diminished by the O_2 exposure; rather, it became sharper due to annealing at 973 K during the experiment. However, on an ideal α-SiC $(000\bar{1})$ surface the terminating atomic layer is composed only of carbon, with each carbon atom bonded to only three underlying silicon atoms. A surface terminated with unsaturated carbon bonds would be expected to be unstable, and yet the (1x1) LEED pattern of the $(000\bar{1})$ surface has been reported from 523 K [39] to 1,173 K.[28] One possible explanation for the apparent stability of the ordered $(000\bar{1})$ surface in UHV is that the topmost carbon atoms are H-terminated. An analogous system is diamond (111), which is hydrogen terminated in UHV and exhibits a (1x1) LEED pattern up to approximately 1,270 K, at which point hydrogen desorption occurs.[40]

3.5 Conclusions

This work utilized a wide temperature and O_2 pressure range in order to study the surface oxidation process of α-SiC from the initial stages of oxide growth to the production of thick SiO_2 layers. In UHV, a sputtered α-SiC surface showed carbon enrichment due to sublimation of SiO and Si at approximately 1,100 K and 1,270 K, respectively. Exposure of sputtered α-SiC to 10^{-8} Torr O_2 from 300 K to 833 K resulted in a two stage oxidation process; a fast initial reaction with O_2 followed by a slower oxidation process with increasing O_2 exposure. At the temperatures examined the 10^{-8} Torr O_2 exposure did not produce SiO_2 and surface graphitization due to SiO and Si sublimation did not occur. Surfaces that were not annealed after sputtering were found to oxidize faster and more extensively than surfaces that did receive post-sputtering annealing. This result, coupled with the low reactivity of an ordered $(000\bar{1})$ surface towards O_2, indicate the importance of surface defects in the initial oxidation of SiC.

Exposure of α-SiC to 1 atm of O_2 for 1 hr. at 300 K and 573 K resulted in the production of thin SiO_x ($x<2$) surface layers. Under identical pressure and time conditions, exposure of α-SiC to O_2 from 873 K to 1,373 K resulted in the production of SiO_2 surface layers on both {0001} surfaces, with the SiO_2 production rate increasing with temperature. Carbon was not detected in the surface SiO_2 layers formed between 873 K and 1373 K, which suggested carbon was removed as CO and/or CO_2 during the SiC oxidation process. For α-SiC, the $(000\bar{1})$ surface was found to produce a thicker SiO_2 layer than the (0001) surface. However, the difference between the two {0001} surfaces appeared sample dependent and was not as dramatic as previously reported. In addition, the thickness of the SiO_2 surface layer showed considerable variation over the

area of the basal surface. One possible explanation for these results is that as-grown α-SiC $(000\bar{1})$ surfaces possess a higher density of surface defects than (0001) surfaces. These defects enhance the oxidation process, causing the $(000\bar{1})$ surface to initially oxidize faster than the (0001) surface.

Chapter 4

The Preparation and Characterization of $Si_xC_yH_z$ Films by Plasma Enhanced Chemical Vapor Deposition

4.1 Introduction

The multiple uses of SiC has led to the development of several fabrication methods. The most commercially important method was developed by Acheson.[41] In this method, silica and carbon are combined in a graphite furnace and fired in a specific temperature vs. time scheme, producing an intergrown mass of intertwined, elongated crystals. Occasionally, lamellar single crystals are obtained, which usually are a mixture of α-SiC polytypes and exhibit only one well developed basal surface. The method is capable of producing SiC on a large scale, but it is prone to contamination and is generally utilized only for the production of abrasives and metalurgical-grade SiC. In 1955 Lely developed a method capable of producing higher quality single crystals.[42] Polycrystalline pieces of SiC produced by the Acheson process are used to form a hollow cylinder inside a graphite furnace. The SiC cylinder is heated to 2,775 K in an atmosphere of argon for several hours, which results in the growth of SiC single crystals on the inside wall of the cylinder. By adding the desired element into the argon atmosphere, the crystals can be doped either p- or n-type. Due to the high temperature, the method is only capable of producing α-SiC.

In recent years, chemical vapor deposition (CVD) has become the preferred method of producing high purity single crystal SiC thin films.[43-46] Unfortunately, the deposition process is slow, prone to contamination, and the high substrate temperatures required limits the applicability of the process.

This chapter details our attempts to produce SiC thin films at lower temperatures utilizing plasma enhanced CVD (PECVD) with methylsilane (CH_3SiH_3). The plasma, created by a radio frequency (R.F.) electrical discharge between two parallel plates, effectively dissociates gas phase molecules, allowing lower substrate temperatures to be used. A mass spectrometric analysis of the plasma showed that the majority of the Si-C bonds were preserved in the gas phase. The composition and the morphology of the $Si_xC_yH_z$ films was studied via XPS, SAES, and SEM as a function of substrate temperature, plasma power and ion flux bombardment of the surface during deposition. Structural information concerning the films was obtained with x-ray diffraction (XRD), Raman spectroscopy and Fourier transform infrared (FTIR) spectroscopy.

4.2 Plasma Enhanced Chemical Vapor Deposition

In chemical vapor deposition, a flow of reactive gases is passed over a heated substrate, which transfers thermal energy to gas phase species when they collide with the substrate surface. This transferred energy can cause bonds in the gas phase species to dissociate, which allows the atomic or molecular fragments to form new bonds with the surface of the growing film. Unfortunately, the process often requires high substrate temperatures in order to support the deposition process. Plasma enhanced CVD allows

lower substrate temperatures to be utilized since the reactive species are created in the gas phase by a plasma.

A plasma is a partially ionized gas mixture which contains electrons, ground state ions, free radicals and excited state ions and neutrals. The plasma is maintained by subjecting the gas to an A.C. or D.C. electric field, which transfers energy to the system chiefly through the acceleration of electrons in the plasma. These accelerated electrons collide with gas phase molecules or atoms to create the species necessary for film deposition. Energy is removed from the plasma by several different processes. Energetic gas phase species can transfer energy by collisions with the substrate or the chamber walls. Photon emission from electron/ion recombination in the plasma also removes energy from the system.

In this work a parallel plate electrode system, shown schematically in fig. 4.1, was utilized to create the plasma. During deposition, one electrode is electrically grounded while a R.F. voltage is applied to the other. The parallel plate configuration is often utilized for flat substrates since the electric field is highly uniform, which facilitates homogeneous film deposition. In this system the transport of neutral species to the substrate is described by known diffusion and adsorption processes. The motion of the ions and electrons in the plasma is quite complicated due to the applied oscillating electric field. The plasma electrons react to the applied electric field more quickly than the heavier ions. Hence, the R.F. plasma utilized in these experiments is considered a cold plasma, since the Boltzmann temperature of the electrons is considerably higher than that of the heavier ions and neutrals.

For a plasma to be stable its overall net charge must be zero, although local variations in charge density are permissible. This charge

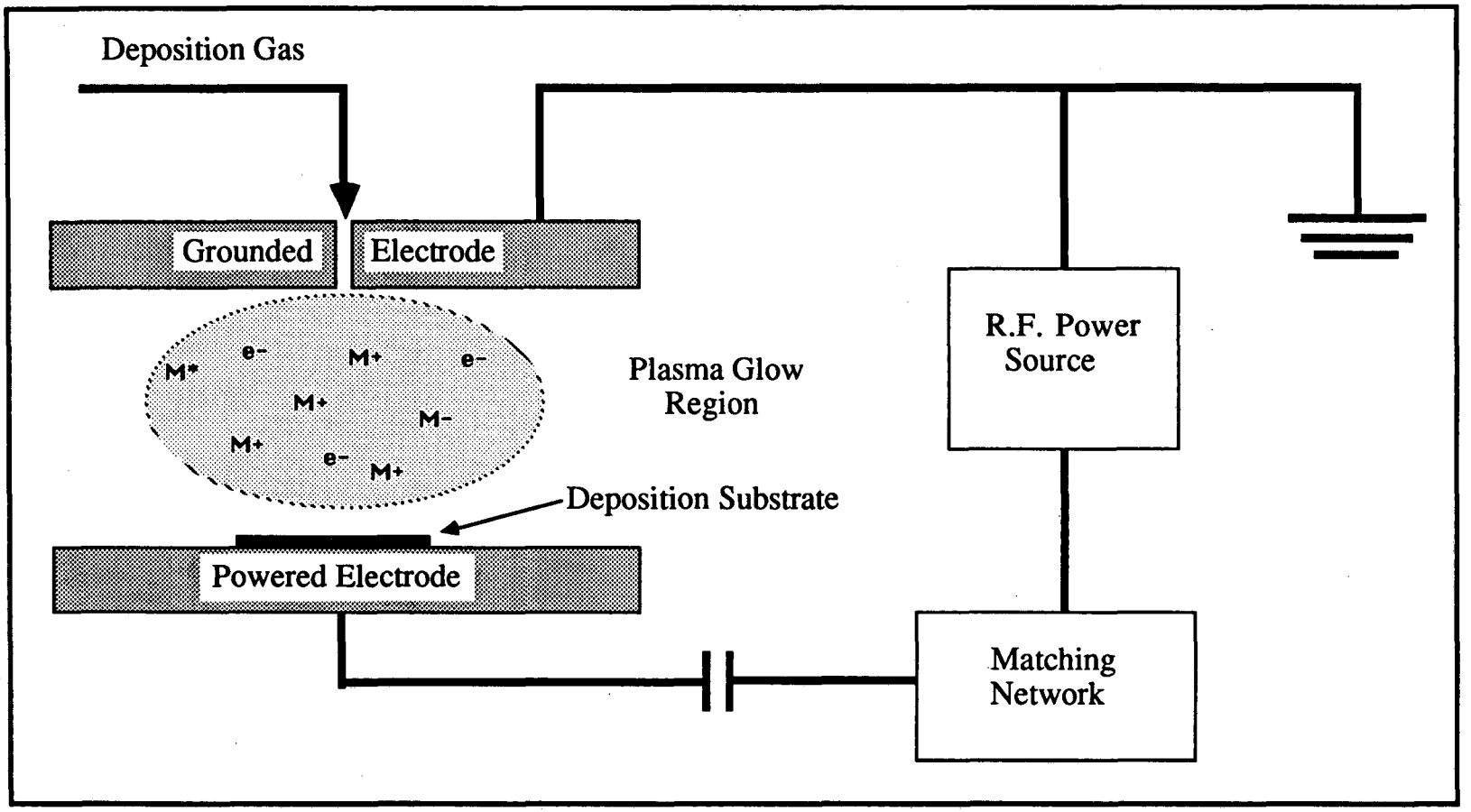

Fig. 4.1: Schematic diagram of the parallel plate R.F. plasma deposition system. The substrate can be attached to either electrode.

neutrality requirement necessitates the use of a capacitor between the powered electrode and and the R.F. power supply. The capacitor, coupled with the higher mobility of the plasma electrons relative to the ions, results in the establishment of a negative self-bias voltage on the powered electrode. (fig. 4.2) This self-bias voltage maintains plasma charge neutrality by retarding the flow of electrons out of the plasma. As shown in fig. 4.3, the self-bias voltage increases monotonically with increasing R.F. power.

Above the powered electrode is a region referred to as the ion sheath. This region is depleted in electron density relative to the glow space of the plasma. The region appears dark since its low concentration of electrons limits the rate of luminescent electron/ion recombination. The ion sheath also accelerates positive ions into the powered electrode, with their kinetic energy being controlled by the gas pressure and composition as well as the potential difference between the powered electrode and the plasma glow region. As will be shown in Section 4.5, the kinetic energy of the impinging ions has a substantial effect on the deposited film's density, composition and adhesion to the underlying substrate.

4.3 Experimental

The R.F. plasma deposition system is shown in fig. 4.4 and 4.5. Film deposition is performed in the upper plasma chamber, which is connected through a differentially pumped middle stage to a high vacuum chamber. A UTI model 100C quadrupole mass spectrometer is mounted in the lower chamber along with a series of electrostatic ion deflection lenses used to measure the ion energy distribution of the plasma. The plasma

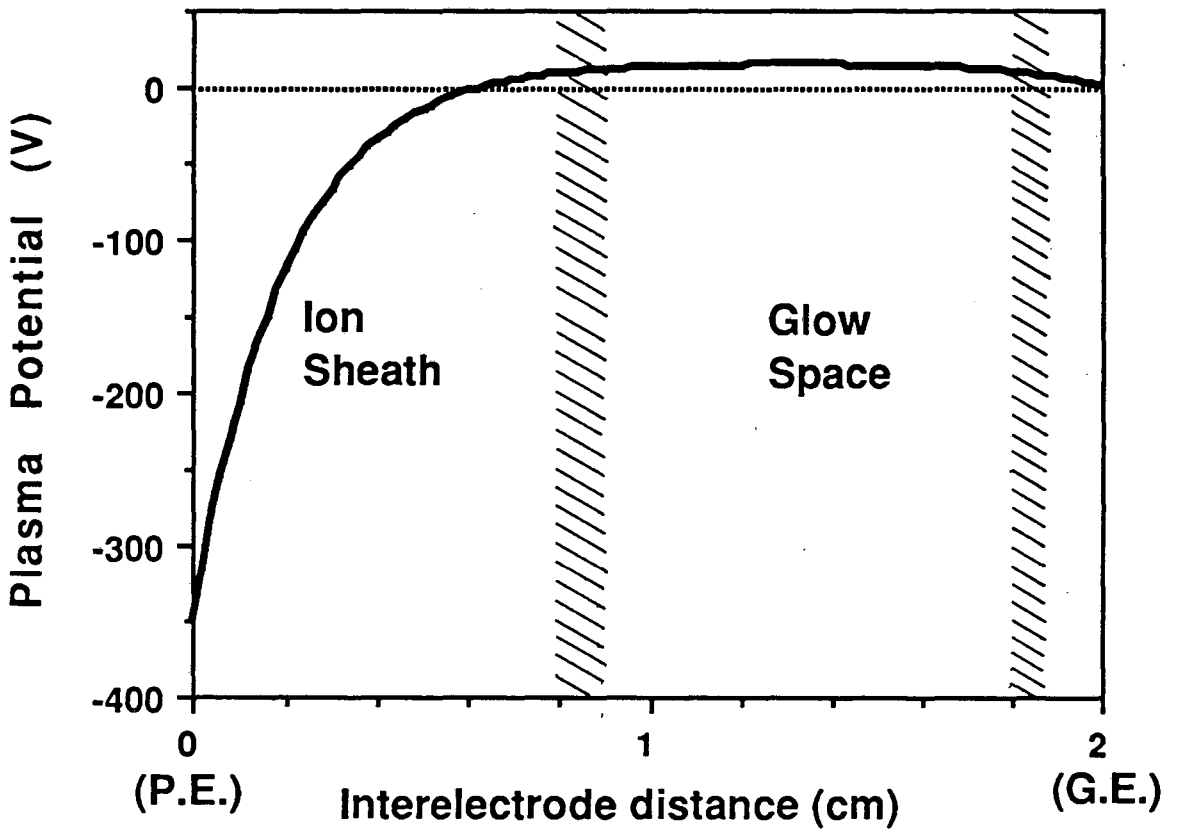

XBL 896-2522

Fig. 4.2: The plasma potential as it varies between the two parallel plate electrodes. The grounded electrode is 2 cm from the powered electrode. The potentials are based on Langmuir probe measurements and ion energy distribution. (G.J. Vandentop, Ph.D. thesis, University of California, Berkeley, 1990)

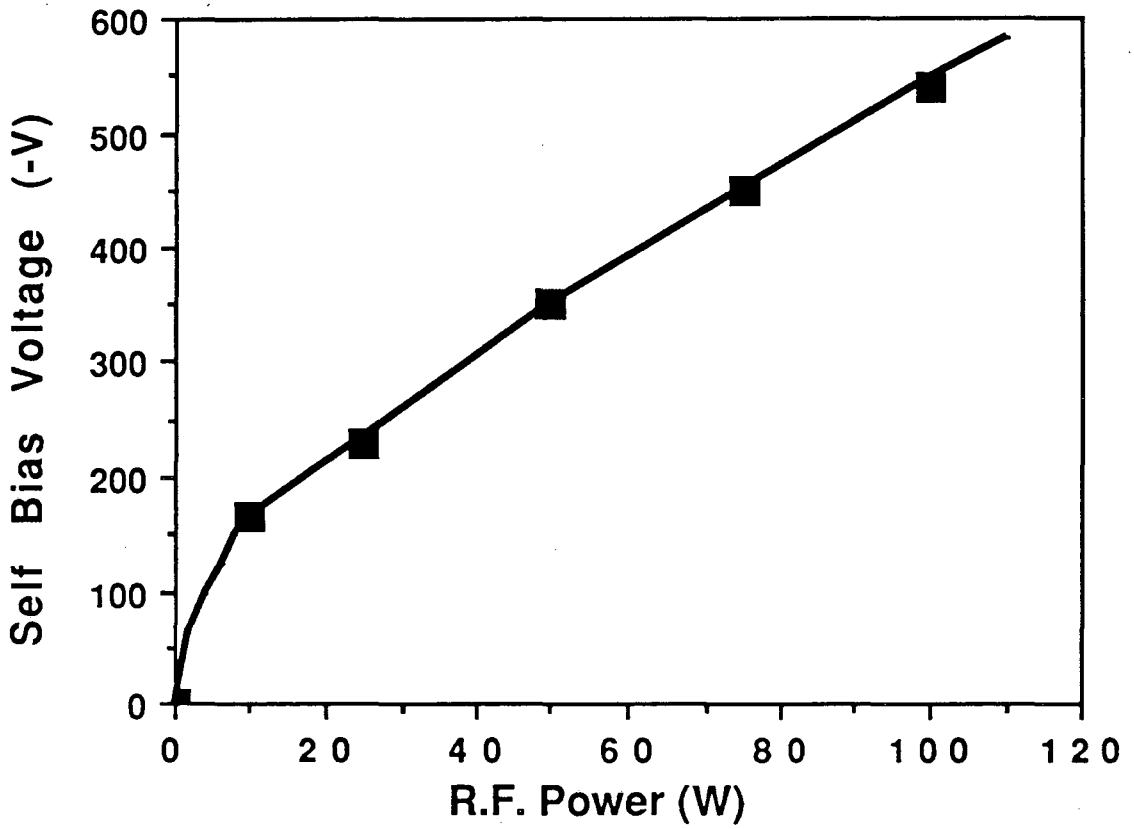

Fig. 4.3: Self-bias voltage of the powered electrode as a function of R.F. power. CH_4 pressure: 65 mTorr. (G.J. Vandentop, Ph.D. thesis, University of California, Berkeley, 1990)

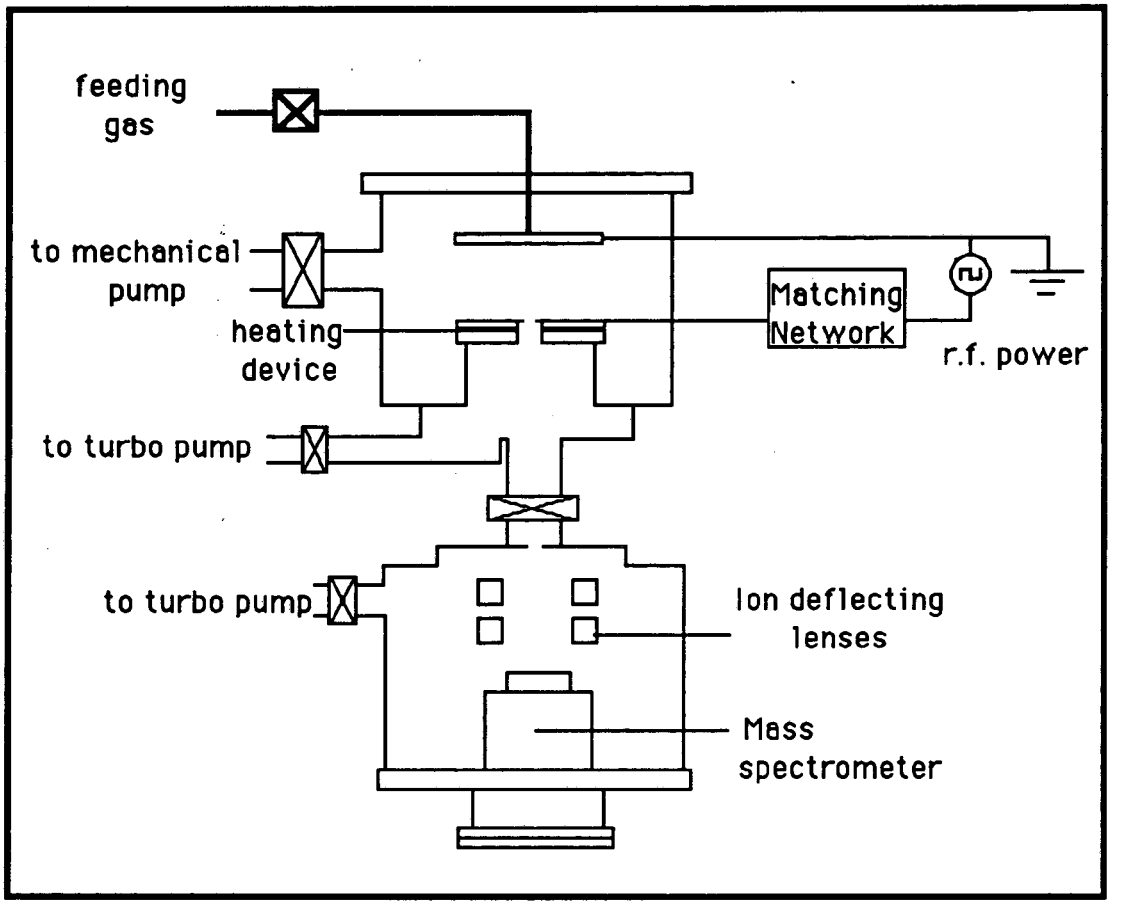

Fig. 4.4: Schematic of the plasma deposition and mass analysis system.

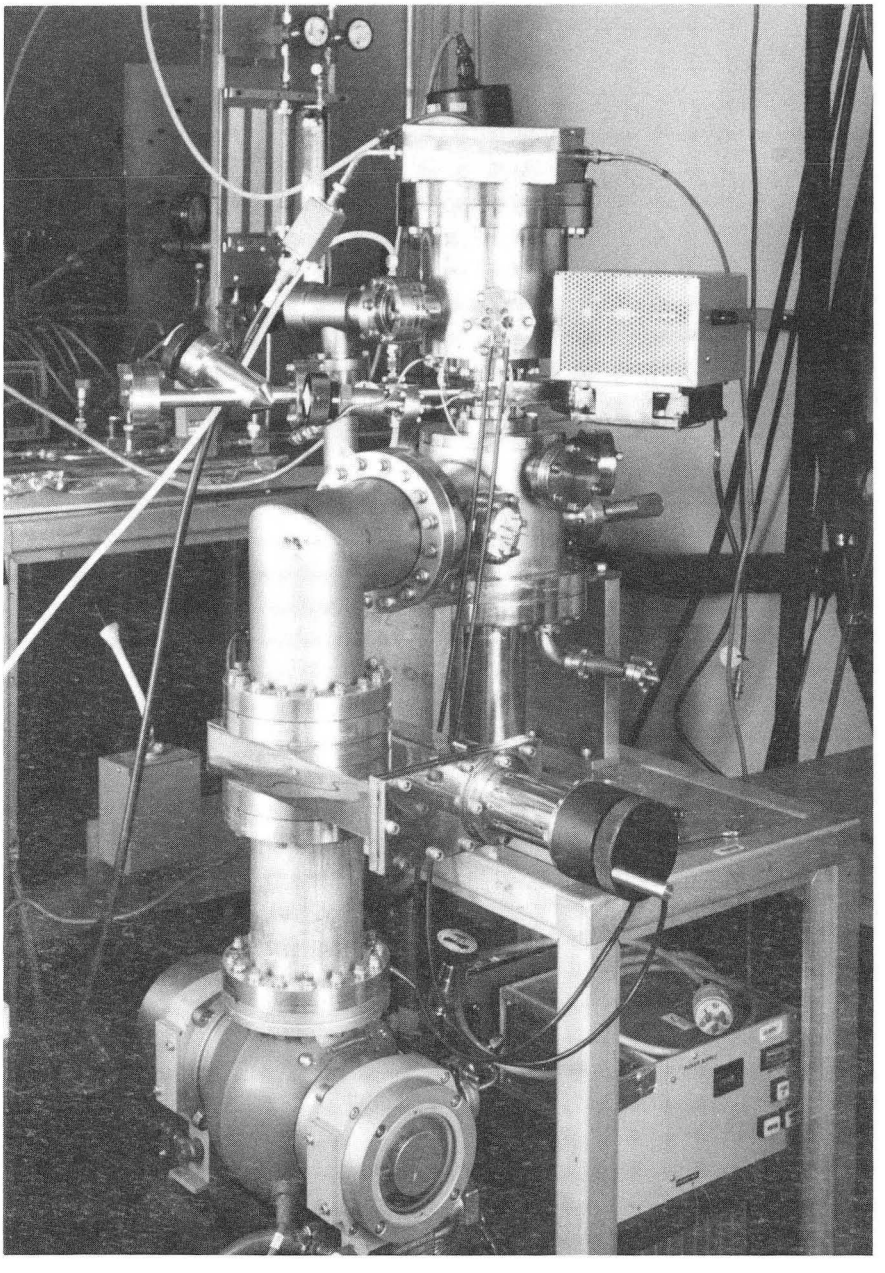

Fig. 4.5: Photo of the plasma deposition and mass analysis system.

chamber is pumped by a rotary vacuum pump and a sorption pump and possesses a base pressure of 10^{-4} Torr. The middle stage and the mass spectrometer chamber are both pumped by a turbomolecular pump, which maintains the lower chamber at a pressure of approximately 10^{-8} Torr. This arrangement allows the determination of the growth precursor species which are incident on the surface of the sample during deposition. A small orifice in the lower electrode allows all the species than normally strike the sample to be extracted from the plasma to be mass analyzed in the lower chamber. The loss of plasma species though the orifice is assumed to have negligible effect on the plasma concentrations since the orifice is small.

The plasma is maintained between two stainless steel electrodes separated by a gap of approximately 2 cm. The films were deposited on the lower electrode which could be heated to 773 K. Either electrode could be powered by the 13.56 MHz R.F. generator, while the other electrode would be grounded. The feed gas, in this case methylsilane (CH_3SiH_3), was introduced into the chamber via an orifice in the center of the upper electrode. Due to the difference in the mobility of electrons and ions in the plasma, the powered electrode spontaneously developed a self-bias. For a R.F. power of 50 W and a CH_3SiH_3 pressure of 100 mTorr, a self-bias voltage of -275 V relative to ground was produced.

Boron doped Si (100) wafers and polycrystalline gold foils were utilized as deposition substrates in these studies. Silicon was chosen in light of the favorable results obtained by CVD on this substrate, while gold was chosen since it forms a silicide at relatively low temperatures. In both cases there is a strong possibility of chemical bond formation between the substrate and deposited film, which leads to better film adhesion. The Si (100) wafers were etched in 49% HF for 5 minutes prior to introduction in

the deposition chamber. The gold foils were prepared for deposition by polishing them with 5 μm alumina paste, followed by a rinse with acetone and methanol. Once in the deposition chamber, the substrates were further cleaned by argon ion bombardment, followed by ignition of the CH_3SiH_3 plasma.

The composition and morphology of the deposited films was determined using SAES, SEM, and XPS. The PHI 660 and 5300 systems discussed previously were utilized. Argon ion depth profiling was performed in the XPS and SAES systems with an eroded area of 1 cm^2 and 1 mm^2, respectively. Thus, the atomic compositions reported in the following sections are representative of the bulk composition. During XPS analysis, the samples were partially covered with gold foil which was used as a reference. The reported XPS binding energies have been corrected in such a way that the $4f_{7/2}$ transition of gold appeared at 83.8 eV.

The crystalline structure of the films was examined with a Siemens x-ray diffractometer. The FTIR spectra were obtained on a Nicolet FTIR spectrometer operating in its transmission mode. The Raman analysis was performed with an Ar^+ laser operating at 488 nm with a spectrometer equipped with a photon counting imaging photomultiplier tube.

The thickness of the deposited films was determined by a Clevite Surfanalyser 150 profilometer for films thicker than 200 nm and by ellipsometry for thinner films. Profilometry also allowed the estimation of the degree of bending of the silicon substrate induced by the stress in the deposited $Si_xC_yH_z$ films. The density of the films was calculated from their mass and volume.

4.4 Mass Spectrometric Analysis of a CH_3SiH_3 Plasma

Two modes of mass spectra acquisition were utilized in these studies. With the ionizer of the mass spectrometer on, both neutrals and positive ions created in the plasma were detected. With the ionizer off, only positive ions created in the plasma were detected. The contribution of the ions (positive and negative) to the signal measured with the ionizer on is so small that the signal can effectively be considered due to neutrals only.

4.4.1 Neutral Species

The neutral species impinging on both the powered and grounded electrodes were measured at two different pressures of CH_3SiH_3 (50 and 100 mTorr) and at three different R.F. powers (50, 100 and 200 W). Under all conditions, four groups of peaks were observed, as seen in fig. 4.6a. The first one is related to species containing a Si-C bond. ($CSiH_z$, $1 \leq z \leq 6$) The second and third groups corresponded to SiH_y ($1 \leq y \leq 4$) and CH_x ($1 \leq x \leq 4$) species, respectively. The last group consists of atomic and molecular hydrogen. Aside from this last group, the most intense peak in the spectra appeared at 44 amu, which is a methylsilane molecule deficient in two hydrogen atoms. This peak could correspond to either CH_3SiH, CH_2SiH_2 or $CHSiH_3$. Experiments with deuterated methylsilane (CD_3SiH_3 or CH_3SiD_3) would allow the unambiguous assignment of this 44 amu peak.

A comparison of fig. 4.6a and 4.6b shows that ignition of the plasma produced minimal changes in the CH_3SiH_3 mass spectra. Plasma ignition increased the amount of atomic and molecular hydrogen. We concluded the plasma did not dissociate the majority of the Si-C bonds since the ratio

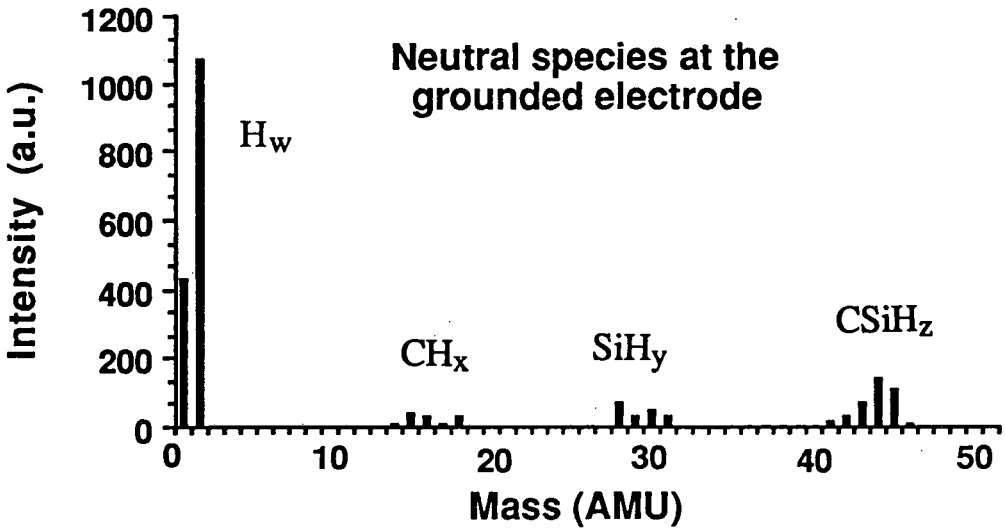

Mass spectrum of the neutral species collected at the grounded electrode. (CH_3SiH_3 pressure: 120 mTorr, R.F. power: 100W)

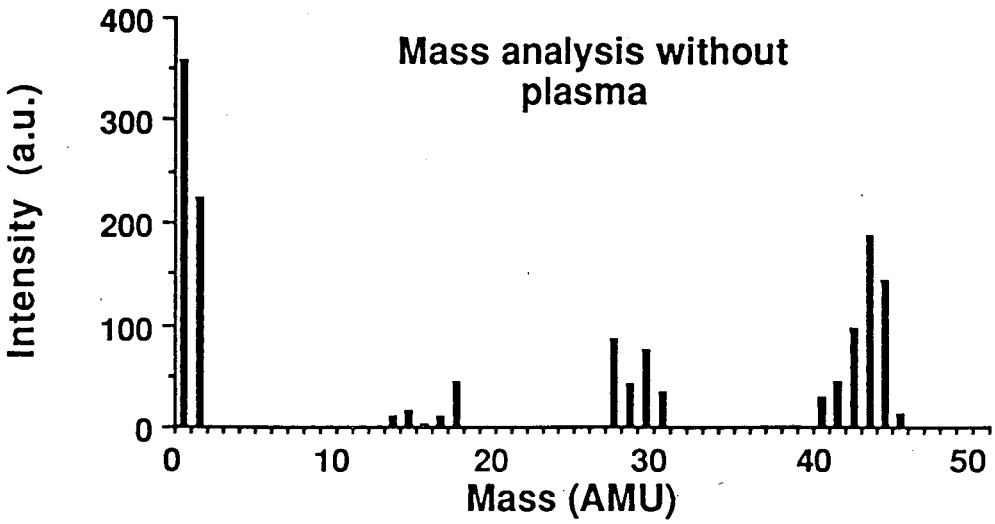

Mass spectrum of CH_3SiH_3 in the absence of plasma. (CH_3SiH_3 pressure: 50 mTorr)

Fig. 4.6

$CSiH_z/SiH_y$ did not change significantly in the absence or presence of the plasma (3.4 vs. 3.5, respectively). It should be noted that this simple comparison of figures 4.6a and 4.6b assumes equal mass spectrometer sensitivity for radicals and non-radicals. No noticeable variation in plasma composition with CH_3SiH_3 pressure or plasma power was observed. No gas phase polymerization appeared to occur since no molecular species with mass greater than 46 amu was detected. The proportions of fragments and intact molecules were the same at the powered and grounded electrodes.

The predominance of gas phase species containing a Si-C bond in the CH_3SiH_3 plasma is a major advantage for the formation of silicon carbide films via a PECVD process. For comparison, a mass spectrometric analysis of a R.F. plasma of a 1:1 CH_4/SiH_4 mixture in the same apparatus showed that few Si-C bonds were created in the plasma itself. In this case, the Si-C bond must be formed at the surface of the substrate, in agreement with the observations of Catherine et al.[47] Therefore, the probability of obtaining Si-C bonds in the deposited films should be higher for a CH_3SiH_3 plasma as compared to a CH_4/SiH_4 plasma.

4.4.2 Positive Ion Species

The ion species were investigated under the same conditions of pressure and R.F. power as were the neutral species. The ions detected in the CH_3SiH_3 plasma included the following:

CH_x^+ ($2 \leq x \leq 4$), SiH_y^+ ($2 \leq y \leq 4$), and $SiCH_z^+$ ($3 \leq z \leq 5$)

Based on a comparison of the mass spectra signal intensities with the ionizer on and off, we have concluded that the positive ions contribute

approximately 0.1% to the total flux of particles impinging on the electrode surface.

As fig. 4.7 shows, the mass spectrum of ions depended strongly on the electrode examined. The average degree of hydrogenation of Si and Si-C species was lower at the powered electrode than at the grounded electrode. More ions containing the Si-C bond bombarded the grounded electrode than the powered one. The difference in the ion flux composition between the two electrodes can be attributed to the influence of the self-bias voltage at the powered electrode. Due to the potential drop in the vicinity of the powered electrode, the average electron/molecule collision energy is higher and the impact is more likely to break Si-C, Si-H and C-H bonds. Thus, the powered electrode is impacted with lighter and less hydrogenated ions than the grounded electrode.

In conclusion, the composition of the neutrals impinging on the surface of the growing films did not appear to depend on whether the electrode was powered or grounded. In the case of ions, the powered electrode was bombarded with more fragmented ions with higher kinetic energy than the ions bombarding the grounded electrode. As will be shown in Section 4.5, these high energy ions had a dramatic effect on the deposited film's density, composition and adhesion to the underlying substrate. Thus, while the bulk of the deposited films was obtained from gas-phase neutrals, the mechanical properties of the films were controlled by the ion flux.

4.5 $Si_xC_yH_z$ Film Composition and Structure

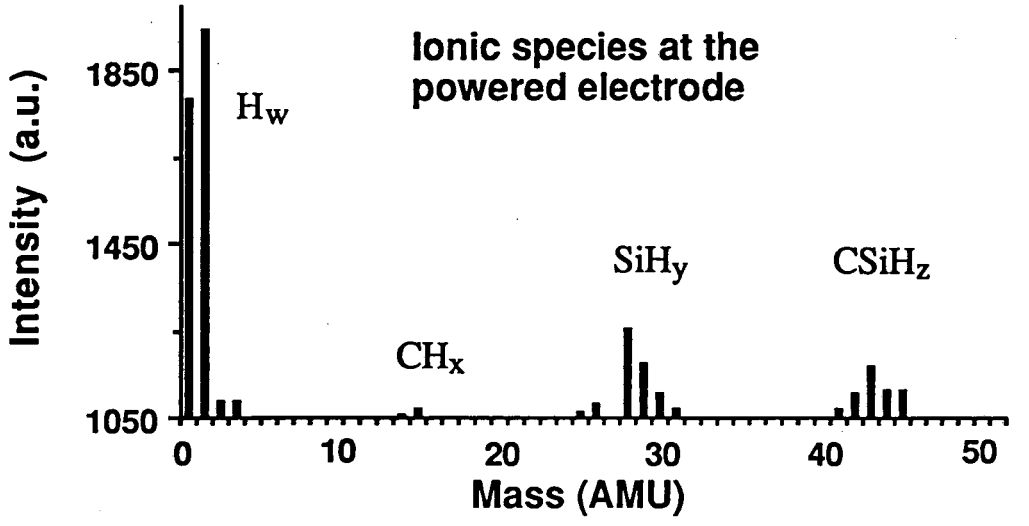

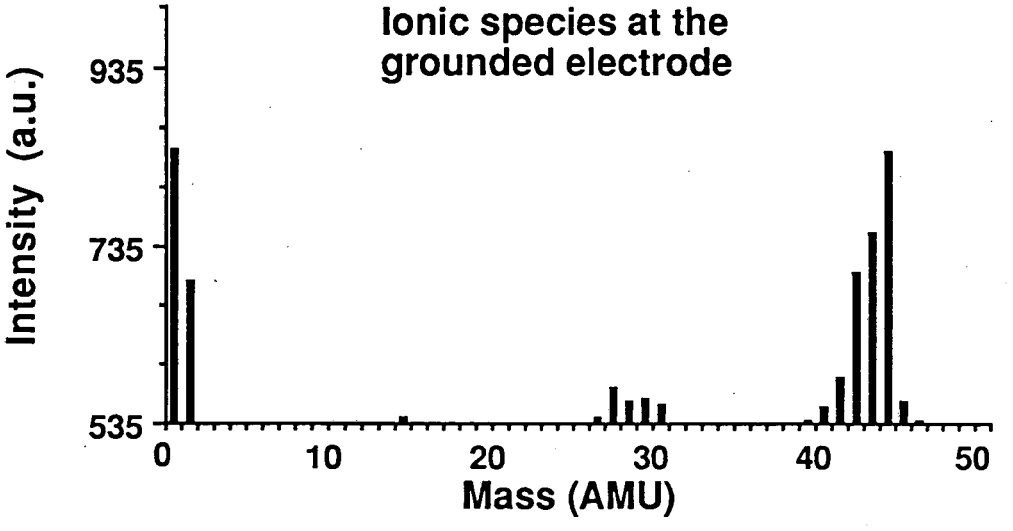

Fig. 4.7: Mass spectra of the ions collected at the grounded electrode and at the powered electrode. (CH_3SiH_3 pressure: 120 mTorr, R.F. power: 100W)

The four substrate temperatures investigated were 333, 423, 573 and 723 K. The deposition rate at each temperature is given in table 4.1. The deposition rate was found to decrease with increasing temperature. Similar behavior was observed for films deposited on gold foils.

4.5.1 Influence of the Substrate Temperature

For the grounded electrode films, XPS and AES analysis showed that the composition of the films depended on the substrate temperature during deposition. At 333 K and 423 K, the films were heavily contaminated with oxygen, while films deposited at 573 and 723 K contained less than 1% oxygen. (See table 4.2) The Si 2p peaks in the XPS spectra of the low temperature samples were broad and contained many contributions from non-stoichiometric and stoichiometric silicon oxides. The oxygen was integrated into the films during deposition and was not due to a contamination layer present on the substrate prior to deposition. The source of this oxygen was most probably H_2O vapor present the chamber. A temperature dependence of the sticking coefficient of the oxygenated species could explain the lack of oxygen incorporation in the high temperature films.

As table 4.2 shows, the films grown at the powered electrode were only slightly contaminated with oxygen, even at low temperatures. This is attributed to the negative self-bias of the powered electrode, which can remove oxygen two different ways. First, in D.C. sputter deposition it is known that a small bias voltage applied to the substrate limits the contamination of the deposit by inducing the desorption of weakly bonded species. Secondly, the powered electrode films are subjected to

Substrate Temperature (K)	Grounded Electrode Deposition Rate (nm/min)	Powered Electrode Deposition Rate (nm/min)
333	22	27
423	20	25
573	10	15
723	6	11

Table 4.1: Variation of the deposition rate as a function of the Si substrate temperature.

R.F. Power: 50 W CH_3SiH_3 Pressure: 100 mTorr

	GROUNDED ELECTRODE					POWERED ELECTRODE				
T (K)	Si 2p BE (eV)	C 1s BE (eV)	Si XPS (at.%)	O XPS (at.%)	Si AES (at.%)	Si 2p BE (eV)	C 1s BE (eV)	Si XPS (at.%)	O XPS (at.%)	Si AES (at.%)
333	98.5 102.0	284.6 280.7		15		100.0	284.8 283.2	60	<1	62
423	99.9	284.7 283.0	48	10		100.0	284.6 283.1	65	<1	65
573	100.1	284.8 283.3	56	<1	60	100.2	284.6 283.2	65	<1	60
723	100.1	284.6 283.1	63	<1	59	100.1	284.7 282.9	70	<1	62
single crystal α-SiC	99.9	283.3	50	0	50	99.9	283.3	50	0	50

Table 4.2: XPS and AES analysis of films deposited on gold foils.
r.f. power = 50W, CH_3SiH_3 pressure = 100 mTorr
Si 2p BE = Si 2p binding energy obtained by curve fitting
C 1s BE = C 1s binding energy obtained by curve fitting
Si XPS, AES = silicon concentration obtained by XPS and AES
O XPS= oxygen concentration obtained by XPS

bombardment by energetic hydrogen atoms and ions, which can induce the reduction of the oxygenated surface species.

Films grown on both the powered and grounded electrodes showed AES lineshapes and XPS C 1s and Si 2p binding energies characteristic of a mixture of SiC and amorphous carbon. The C 1s binding energy peak, shown in fig. 4.8, clearly shows the presence of at least two types of carbon; carbidic (ie. sp^3 hybridized) and amorphous. In contrast, the silicon AES and XPS signals exhibit mainly carbidic features, as shown in fig. 4.9. The XPS binding energy values obtained for the SiC phase of the films were within experimental error of the values obtained for single crystal α-SiC. The results indicated the presence of two phases in the deposited films: one characterized mainly by Si-C bonds and the other by C-C and/or C-H bonds. In AES, the carbon KLL transition exhibited "carbide" peaks at 249 and 255 eV, along with a peak at 240 eV characteristic of amorphous carbon or graphite.

For films grown on both electrodes, XPS and AES indicated that the SiC phase of the films was enriched in silicon relative to stoichiometric single crystal α-SiC. A difference in the sticking coefficients of the species containing carbon and the species containing silicon could be responsible for this nonstoichiometry.

A difference in composition between powered electrode films and grounded electrode films was small but reproducible: the powered electrode films systematically contained more silicon. One possible explanation for this phenomenon is that energetic hydrogen bombardment at the powered electrode preferentially removes carbon from the growing film as CH_4, leaving silicon remaining on the surface.[48]

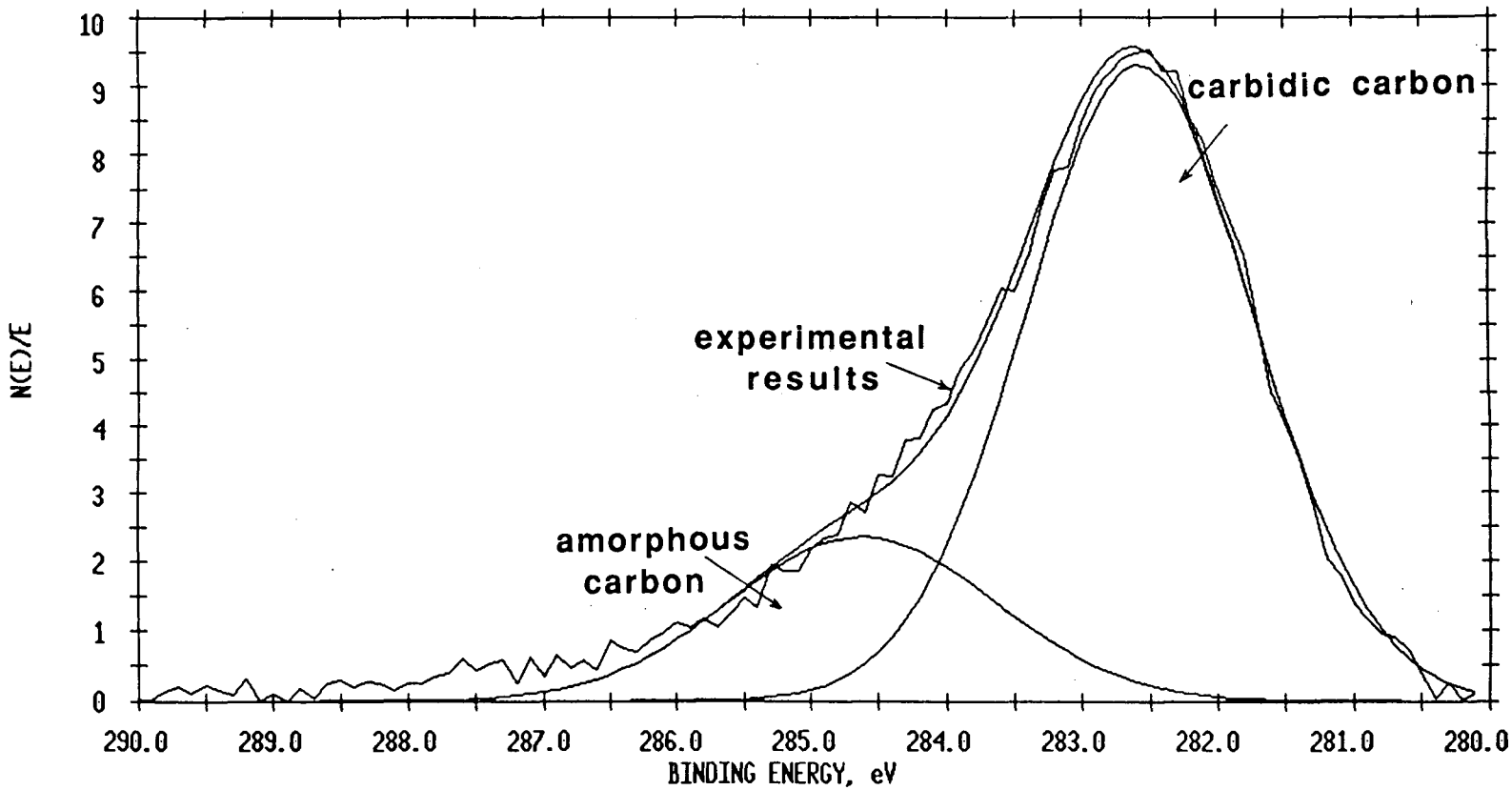

Fig. 4.8: The C 1s photoelectron line of a film deposited on gold at 723 K on the powered electrode. (CH_3SiH_3 pressure: 100 mTorr, R.F. power: 50 W)

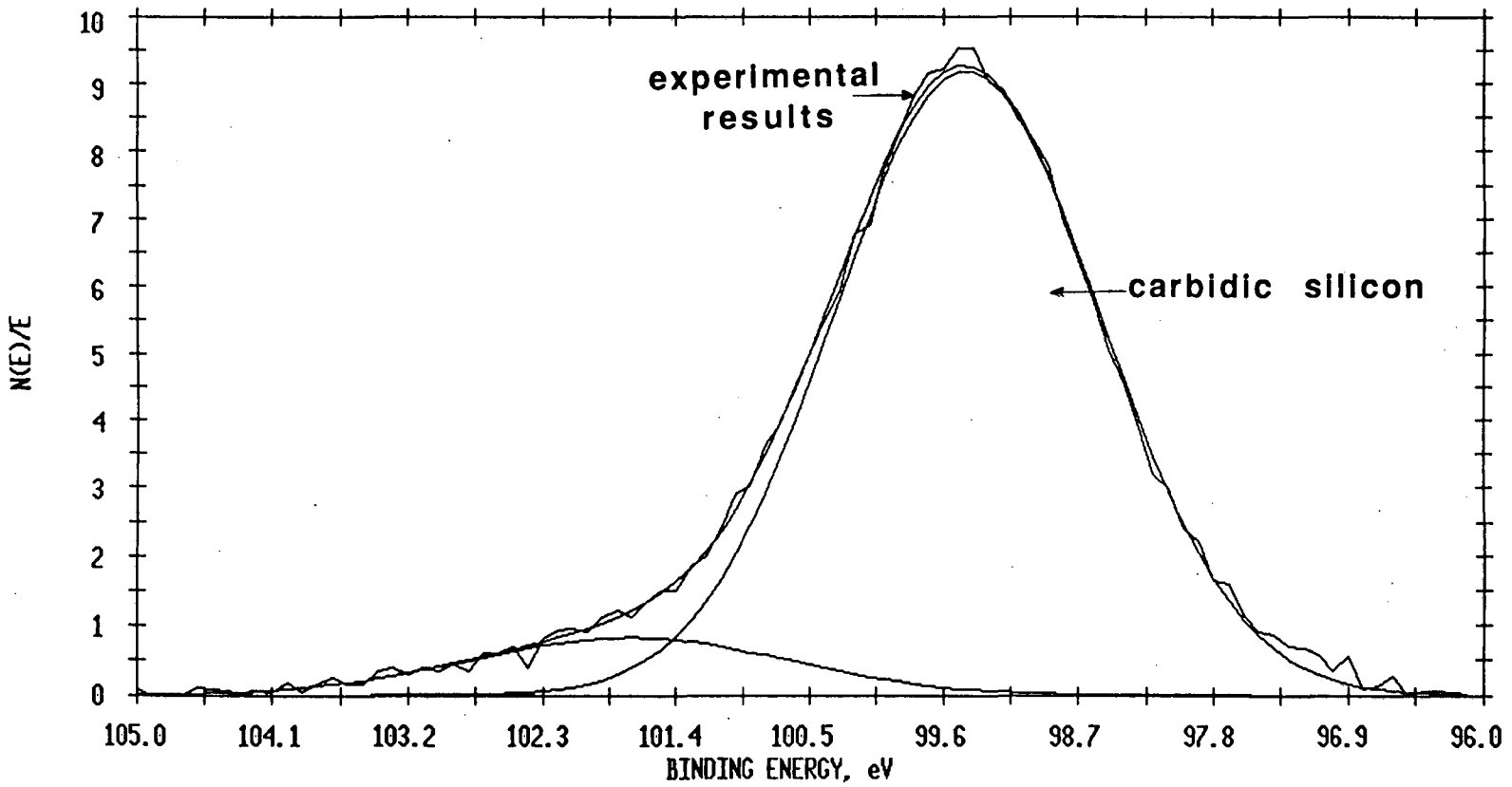

Fig. 4.9: The Si 2p photoelectron line of a film deposited on gold at 723 K on the powered electrode. (CH_3SiH_3 pressure: 100 mTorr, R.F. power: 50 W)

4.5.2 Influence of the R.F. Power

Films formed at the powered electrode at 573 K at three different R.F. powers (50, 75 and 100 W) were investigated. The self-bias developed by the powered electrode under these conditions varied between -225V at 50 W and -300V at 100 W. An increase in the deposition rate with increasing plasma power was observed, which was expected because the increase in R.F. power increased the degree of molecular dissociation in the gas phase.

No strong dependance of the film composition on the R.F. power was detected. The compositional variations were within the experimental error range of AES and quantitative XPS analysis. The change in the energy of the ions bombarding the surface of the growing films did not significantly influence the carbon/silicon ratio in the films.

4.5.3 Film Density and Stress

At both electrodes, an increase in the substrate temperature resulted in an increase in the film density, as shown in table 4.3. A comparison of films produced on the powered and grounded electrodes at the same temperature showed that ion bombardment also increased the density of the films. The density measured for a film deposited at 573 K on the powered electrode was close to that of bulk silicon carbide (3.21 g/cm^3).

Profilometry was utilized to estimate the degree of bending of the silicon and gold substrates induced by the compressive stress in the deposited films. The bending due to the film stress was found to increase with increasing deposition temperature. For the grounded electrode, no

T (K)	GROUNDED ELECTRODE		POWERED ELECTRODE	
	Deposition rate (nm/min)	Density (g/cm^3)	Deposition rate (nm/min)	Density (g/cm^3)
333	22	1.5	27	2.0
573	10	2.0	15	3.2

Table 4.3 : Deposition rate and density of the films as a function of the substrate temperature.

R.F. Power: 50 W CH_3SiH_3 Pressure: 100 mTorr
Density of single crystal SiC : 3.21 g/cm^3.

stress was detected on the two substrates at 333 and 423 K, while at 573 and 723 K a slight bending of the substrate was measured. The stresses in the films formed at the powered electrode were so large that the gold foils were visibly bent and thick films (> 1 μm) deposited on silicon wafers delaminated to release the interfacial tension. Thinner films deposited on silicon substrates remained attached. The adhesion of these films to the substrates in the presence of high stresses suggested the formation of strong chemical bonds at the interfaces. The nature of these bonds would be C-Si and Si-Si for silicon substrates and Si-Au on gold substrates.

4.5.4 Film Structure

In order to obtain information concerning film structure, films thicker than 1 μm were deposited on silicon and sapphire substrates and examined by SEM, XRD, Raman and FTIR. The SEM images of the films duplicated the substrate morphology and did not show any features of their own. X-ray diffraction analysis indicated the films were completely amorphous under all deposition conditions. The absence of any features in the Raman spectra of the films indicated they were completely disordered with a polymer-like structure.

FTIR spectroscopy provided information concerning the bonding between the Si, C and H present in the film. Silicon substrates were utilized for spectra in the 250-2300 cm^{-1} range while sapphire substrates were used for spectra in the 2300-4000 cm^{-1} region. Sapphire was chosen for its transparency in this range of IR frequencies. Typical spectra are shown in fig. 4.10. The spectra exhibited three main regions of IR adsorption. The first region, located at about 2080 cm^{-1}, was assigned to

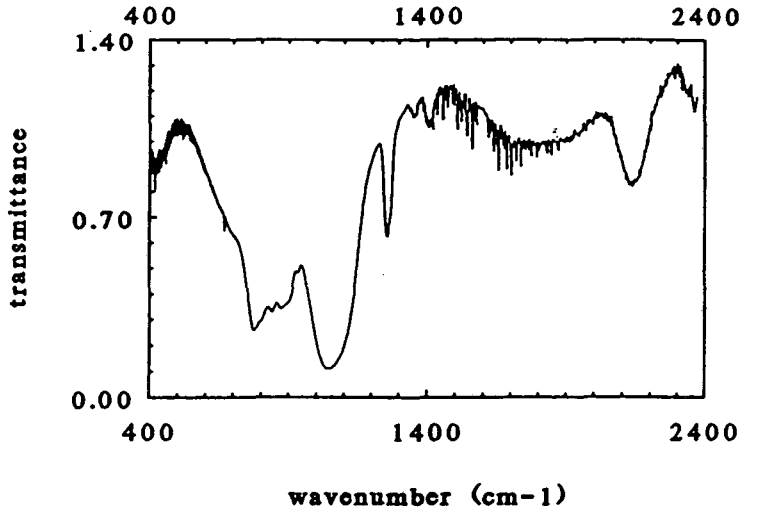

(a)

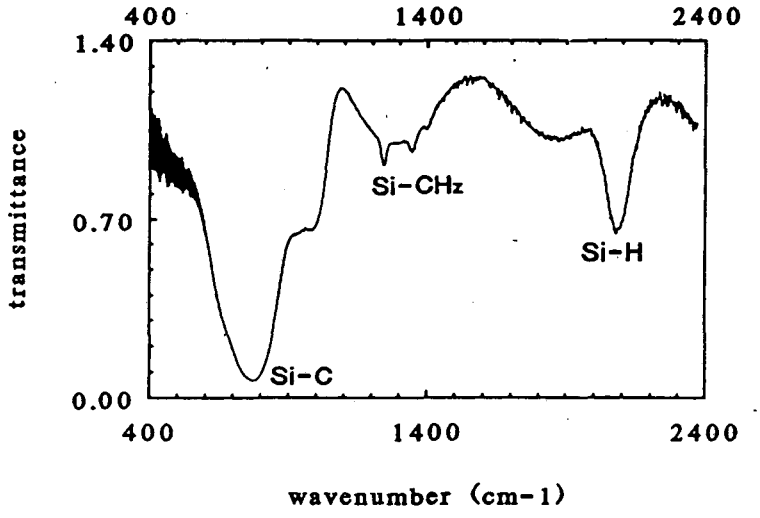

(b)

Fig. 4.10: The FTIR spectra of
a) film deposited at the grounded electrode at 333K
b) film deposited at the grounded electrode at 573K
c) film deposited at the powered electrode at 333K
d) film deposited at the powered electrode at 573 K

(CH_3SiH_3 pressure: 100 mTorr, R.F. power: 50 W)

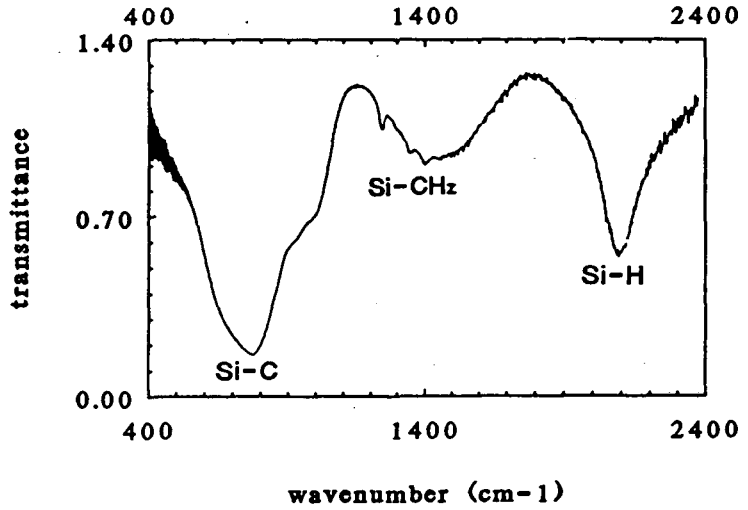
400
1400
2400
1.40
0.70
0.00
transmittance
Si-CH2
Si-H
Si-C
400
1400
2400
wavenumber (cm-1)

(c)

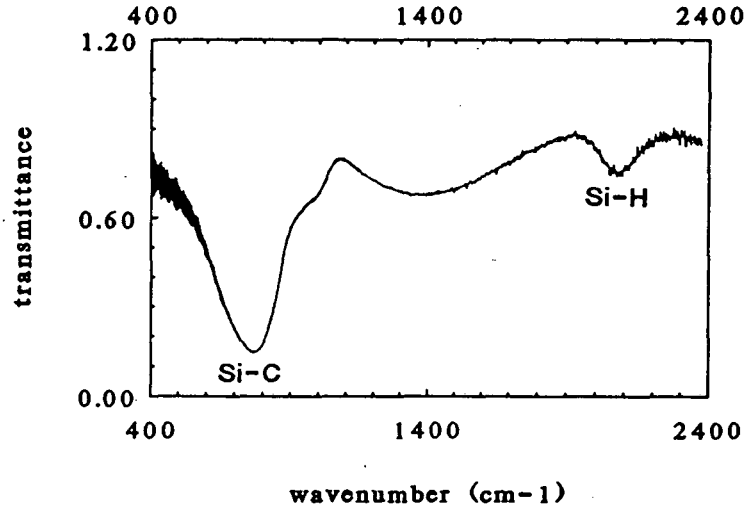
400
1400
2400
1.20
0.60
0.00
transmittance
Si-H
Si-C
400
1400
2400
wavenumber (cm-1)

(d)

the Si-H vibrational stretch when 1-3 carbon atoms are attached to the silicon atom.[47,49] The assignment of the absorption bands in the second region (400-1100 cm^{-1}) is summarized in table 4.4.[47] Lastly, the stretching modes of C-H bonds in $-CH_3$ and $-CH_2$ groups are responsible for the absorption bands in the vicinity of 3000 cm^{-1}.

The spectrum obtained for a film deposited at the grounded electrode at 333 K (fig. 4.10a) presented features resulting from the incorporation of oxygen and was not characteristic of Si-Si, Si-C, Si-H or C-H vibration modes. Increasing the deposition temperature to 573 K removed the oxygen from the film and transformed the IR spectrum into one characteristic of an amorphous $Si_xC_yH_z$ compound. (fig. 4.10b)

The ion bombardment present at the powered electrode produced films with IR spectra very similar to those seen with high temperature grounded electrode films. A comparison of fig. 4.10b and 4.10c shows that the spectra of films obtained at 573 K on the grounded electrode closely resemble those of films produced at 333 K on the powered electrode. The strong asymmetry of the absorption band at 780 cm^{-1} reflects the presence of SiH_2 groups ($\cong$ 620 cm^{-1}) and of $Si-CH_3$ and $Si-CH_2$ groups (shoulder at $\cong$ 1000 cm^{-1}). This was confirmed by the absorption bands present in the region 1250-1400 cm^{-1} corresponding to bending modes of CH_2-Si (1250 cm^{-1}), CH_3-Si (1350 cm^{-1}) and CH_3-SiH_3 (1400 cm^{-1}). The stretching modes of $-CH_2$ and CH_3 groups are unresolved but the asymmetry of the peak indicated a higher proportion of $-CH_2$ groups. As shown by the relative intensity of the Si-H stretching band, hydrogen incorporation in the films was influenced more strongly by increasing temperature than ion bombardment.

Wavenumber (cm^{-1})	Vibration Mode
620	Si-H,Si-H_2 wagging & rocking
675-680	Si-C stretching
780	Si-C stretching
	Si-CH_3 rocking or wagging
860	Si-H_2, $(SiH_2)_n$ bending
890-900	Si-CH_3 rocking
1020-1040	Si-CH_2 rocking or twisting

Table 4.4: Assignment of the IR absorption bands in the 400-1100 cm^{-1} range.

Films deposited on the powered electrode at 573 K presented the least distinct absorption properties (fig. 4.10d) of all the films examined. The absence or reduced intensity of many of the absorption bands was related to the smaller amount of hydrogen incorporation in the film. The intensity of the Si-H stretching mode at 2080 cm^{-1} was reduced by a factor of two relative to the grounded electrode film. The CH_3-Si bending modes were completely absent. This reduction in hydrogen incorporation was due to both the high temperature and ion bombardment during deposition. This increased the number of Si-C bonds in the film, which resulted in a film density within experimental error of bulk, single crystal SiC.

4.6 Conclusions

Deposition of amorphous SiC:H films by PECVD from CH_3SiH_3 on silicon and gold substrates was investigated. The characteristics of the films, including composition, density, structure and IR absorption bands were determined as a function of the deposition variables. These variables included plasma composition, substrate temperature, R.F. plasma power and ion flux.

The mass spectrometric analysis of the $CH_3\dot{S}iH_3$ plasma showed that the majority of the Si-C bonds were preserved in the gas phase, increasing the probability of including this type of bonding in the films. Differences in the ion flux composition and energy were observed between the powered and grounded electrode. Powered electrode films, subjected to high energy ion bombardment, were found to be denser, to contain less hydrogen and oxygen, and to have better adhesion to the substrate. A large amount of compressive stress was developed in the powered electrode films, but their

adhesion to the substrates suggests the formation of strong chemical bonds at the interface.

Analysis by AES and XPS showed the presence of two phases in the deposited films. The "SiC" phase was characterized by a majority of Si-C bonds, while the amorphous carbon phase was characterized by C-C and/or C-H bonds. Compared to single crystal α-SiC, the "SiC" phase of the deposited films was found to contain excess silicon.

Under all deposition conditions the films were found to be completely amorphous. We believe this is due to the relatively low substrate temperatures utilized and the high deposition rate of the R.F. plasma. We are currently attempting to produce crystalline SiC by microwave plasma enhanced chemical vapor deposition, which has proven effective in the low pressure deposition of diamond. However, microwave deposition systems require higher gas pressures in order to maintain a stable plasma. Thus, we plan to dilute the CH_3SiH_3 feed gas with H_2, which should also retard the formation of amorphous carbon phases.

Chapter 5

Surface Crystallography of β-SiC by LEED

5.1 Introduction

The β-SiC surface, like GaAs, exhibits a wide range of reconstructions which are dependent on the surface composition and morphology.[32] The stoichiometric β-SiC (100) surface is terminated in a layer of silicon atoms, which reconstruct to produce either a (2x1) or c(4x2) LEED pattern. These reconstructions are believed to be analogous to those found with Si (100), in which the topmost silicon atoms dimerize in order to reduce the number of unsaturated surface bonds.[32] The addition of silicon to the stoichiometric β-SiC (100)-(2x1) surface has been reported to produce (3x2) and (5x2) surface reconstructions.[50] It is postulated that these surfaces involve rows of silicon dimers on top of a silicon terminated surface. The removal of silicon from the (2x1) surface via high temperature UHV annealing results in a surface reconstruction exhibiting a slightly diffuse c(2x2) LEED pattern. A sharper c(2x2) pattern may be obtained by the deposition of surface carbon produced by exposing the (2x1) surface to ethylene (C_2H_4) gas at 1,125 K.

The determination of the internal geometry of the surface unit cells of these reconstructions by LEED requires the intensity (I) of each diffraction spot to be measured as a function of incident electron energy (V). Once done, dynamical LEED theory is utilized to determine the positions of the surface atoms through a comparison of theoretical I-V

curves from model surfaces with the experimentally determined I-V curves. This chapter begins with a discussion of the main components of modern dynamical LEED theory. It is written at a level suitable for a beginning chemistry graduate student who wishes to understand the logic and nomenclature of LEED calculations. The remainder of the chapter discusses the atomic structure of the c(2x2) and (2x1) surface reconstructions. Our structure analysis of the c(2x2) surfaces produced by silicon sublimation or C_2H_4 exposure shows both surfaces are terminated with C_2 groups in staggered silicon bridge sites. Evidence of weak Si--Si dimer formation is found in the 2nd atomic layer of the silicon sublimation c(2x2), but not for the C_2H_4 exposed c(2x2). Preliminary results for the (2x1) reconstruction indicate the surface is silicon terminated with the topmost silicon atoms forming asymmetric dimers. This agrees well with total energy calculations which predict the dimer asymmetry is caused by charge transfer within the dimer.

5.2 Dynamic LEED Theory

Unlike x-rays, low energy electrons (30-400 eV) have such a limited elastic mean free path in a solid that diffraction processes detected by LEED originate from the topmost 5-10 Å of the solid. The scattering of low energy electrons by the ion cores of the solid is considerably stronger than found for x-rays. This strong scattering greatly complicates surface crystallography studies, since one must account for the significant probability that an electron will scatter elastically several times in the surface region before escaping to be detected. This multiple scattering phenomenon does not allow LEED theory to utilize many of the simple

kinematic ideas developed for x-ray diffraction, which is based on the assumption that the x-ray scatters only once while in the solid.

The electron diffraction process is considered a "dynamical" process since non-geometrical parameters must be included in any theoretical modeling of experimental results. These parameters include multiple scattering, the inner potential of the solid, inelastic electron damping in the solid and energy and angular dependent atomic scattering amplitudes.

5.2.1 Calculational Overview

The calculation of the I-V curves of a model surface assumes that the crystal surface is a perfect lattice and the incident electron beam can be described by a plane wave with wavevector $\mathbf{k}_o$. The first step involves the calculation of the energy dependent electron scattering amplitudes of each atom present at the surface. This is simplified since only elastic scattering contributes to LEED, which means only the phase of the incident electron wavefunction is changed by the scattering process. Hence, in LEED calculations atoms may be replaced by point scatterers with scattering characteristics described by energy dependent phase shifts.

Once the phase shifts are computed, the atoms (now represented as point scatterers) are placed in a layer. The multiple scattering within this layer is now computed with the wavefunction of the LEED electrons represented as a linear combination of spherical waves. Finally, the layers are stacked upon each other using one of several computational schemes and the interlayer scattering is calculated. At this stage the wavefunction between the stacked layers is represented as a plane wave, since the diffraction by each layer produces a discrete set of diffraction beams, each

of which may be represented as a plane wave. During the calculation of intra- and interlayer scattering, the loss of incident electron flux due to inelastic processes such as plasmon excitation is accounted for by including a damping term in the inner potential of the solid. The reduction of diffracted intensity due to electron/phonon scattering is accounted for with a Debye-Waller term. An excellent source of additional information concerning dynamical LEED may be found in *Low-Energy Electron Diffraction.*[51]

5.2.2 The Muffin-Tin Model

The electron scattering characteristics of an atom depend strongly on the species and also on the local chemical environment of the atom. The scattering potential of an atom, which depends on the local electron density of the crystal, is often approximated quite well using the muffin-tin model. In this model, each atom in the surface is represented by a spherically symmetrical potential of known radius (R). As fig. 5.1 shows, outside each ion core the potential is considered to be constant and is referred to as the muffin-tin constant or muffin-tin zero. Within the ion core the electron distribution is calculated using free atom electron wavefunctions that are truncated at radius R. The remaining electron density is distributed evenly throughout the remaining space. This model is especially well-suited for metals, where the interaction of the incident electrons with the conduction electrons of the crystal is represented by the muffin-tin constant and the interaction with the ion cores is represented by the spherically symmetrical component.

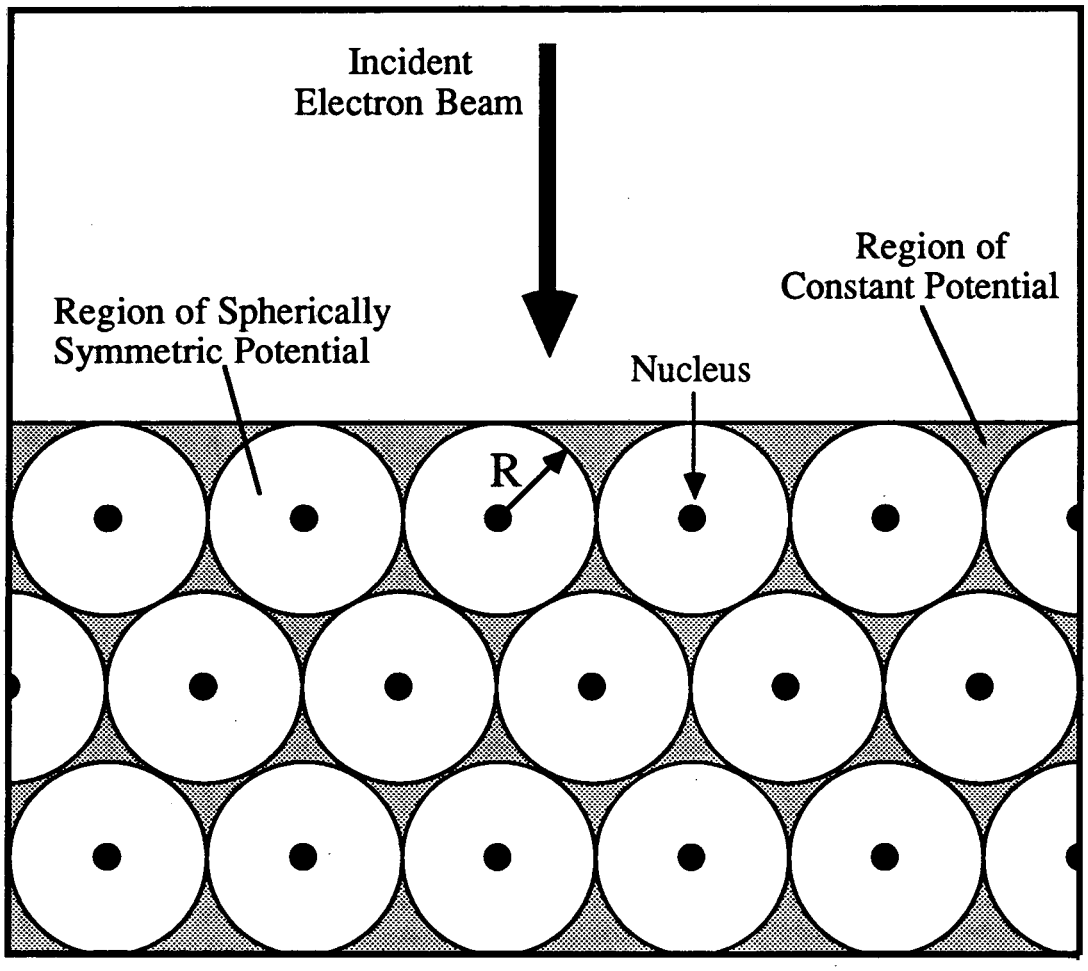

Fig. 5.1: Sketch of a surface represented by the muffin-tin model.

The muffin-tin model, coupled with the requirement of elastic scattering, allows the electron scattering of a single atom to be represented by a series of phase shifts. The scattering of a plane wave by a spherically symmetrical potential of finite range may be represented by an atomic scattering factor $t(\theta)$, where θ is the scattering angle. For a wave with wavevector $\mathbf{k}_o$, the scattering has the following asymptotic (i.e. $|\mathbf{r}| \rightarrow \infty$) form

$$\exp(i\mathbf{k}_o \cdot \mathbf{r}) + [t(\theta)/r] \cdot \exp(i\mathbf{k}_o \cdot \mathbf{r}) \tag{5.1}$$

where r is the distance from the atomic nucleus. The atomic scattering factor is expanded in Legendre polynomials P_j, yielding

$$t(\theta) = 4\pi \sum_{j=0}^{\infty} (2j + 1)\, t_j\, P_j(\cos\theta) \tag{5.2}$$

where t_j is a t-matrix element with

$$t_j = [\exp(i\delta_j) \sin \delta_j] / (2k_o) \tag{5.3}$$

where δ_j are the energy dependent phase shifts. Given the phase shifts of an element, one can calculate the scattering by its muffin-tin sphere of any wave incident upon it. To calculate the phase shifts, one must integrate the radial Schrodinger equation involving the atomic potential described by the muffin-tin model.[51] Fortunately, the phase shifts of an element need only be calculated once for use in many different LEED calculations.

The relationship between $|\mathbf{k}_o|$ and the incident electron energy (V) is given by $|\mathbf{k}_o| = \{2(V - V_{or} - iV_{oi})\}^{1/2}$. The real and imaginary components of the muffin-tin constant (V_{or} and V_{oi}, respectively) are included for two reasons. The V_{or} term (typically -10 to -14 eV) is included to correct for the fact that experimentally measured electron energies are referenced to

the Fermi levels of the sample and electron gun, while theoretical electron energies are referenced to the vacuum levels of the sample and electron gun. The imaginary component of the muffin-tin constant accounts for the loss of incident electron flux due to inelastic processes such as plasmon excitation. The majority of LEED calculations assume V_{oi} to be constant (typically -4 to -5 eV), although some allow it to be a function of incident electron energy.

In LEED calculations, the decrease in diffracted intensity with increasing crystal temperature is accounted for by multiplying the scattering amplitude of each atom by a Debye-Waller factor

$$t^T(\theta) = \exp(-\Theta/T) \cdot t(\theta) \qquad (5.4)$$

where Θ is the surface Debye temperature and T is the sample temperature. Hence, by measuring LEED beam intensities as a function of temperature, one may gain information concerning surface vibration characteristics, which may be quite different from those of the bulk.

5.2.3 Intra- and Interlayer Electron Scattering

The next step of the calculation involves the determination of the electron scattering characteristics of individual planes of atoms. This is done by producing a diffraction matrix (M) for the layer. The elements of this matrix $\{M_{g'g}\}$ describe the diffraction amplitude between the incident wave $\exp(i\mathbf{k}_g \cdot \mathbf{r})$ and the scattered wave $\exp(i\mathbf{k}_{g'} \cdot \mathbf{r})$. The matrix elements are calculated utilizing the phase shifts described previously. Within the plane the scattered electron wave is represented as a linear combination of spherical waves.

Once completed, the electron scattering between the various layers is calculated. This requires that the diffraction matrix for each layer be "stacked", using one of several computational schemes such as renormalized forward scattering (RFS) or layer doubling. Computationally, RFS is often the faster of the two, but it is generally unsuited for small interlayer spacings. As shown schematically in fig. 5.2, the incident wave field on underlying layers consists of the sum of the transmitted incident plane wave and any scattering which occurs in previous layers. The total diffracted wave field is the sum of the diffraction amplitudes from all of the layers. By calculating the diffracted intensity of each beam at various incident electron energies, one obtains the theoretical I-V curves for a model surface.

The number of plane waves in set $\{\mathbf{k_g}\}$ depends on the interlayer spacing and also on the mean free path of the electron in the solid. Incident electron energies above 400 eV and small interlayer spacing are problematic for LEED calculations due to the large number of plane waves and phase shifts that must be considered.

5.2.4 R-Factors

A surface structure is thought to be "solved" when the agreement between theoretical and experimental I-V curves has been optimized. To compare I-V curves quickly and quantitatively, various quantifiers known as reliability factors, R-factors, residues or residuals have been developed. R-factors are single numbers summarizing the agreement between theoretical and experimental results. They are always positive with zero signifying perfect agreement between theory and experiment. Multiple

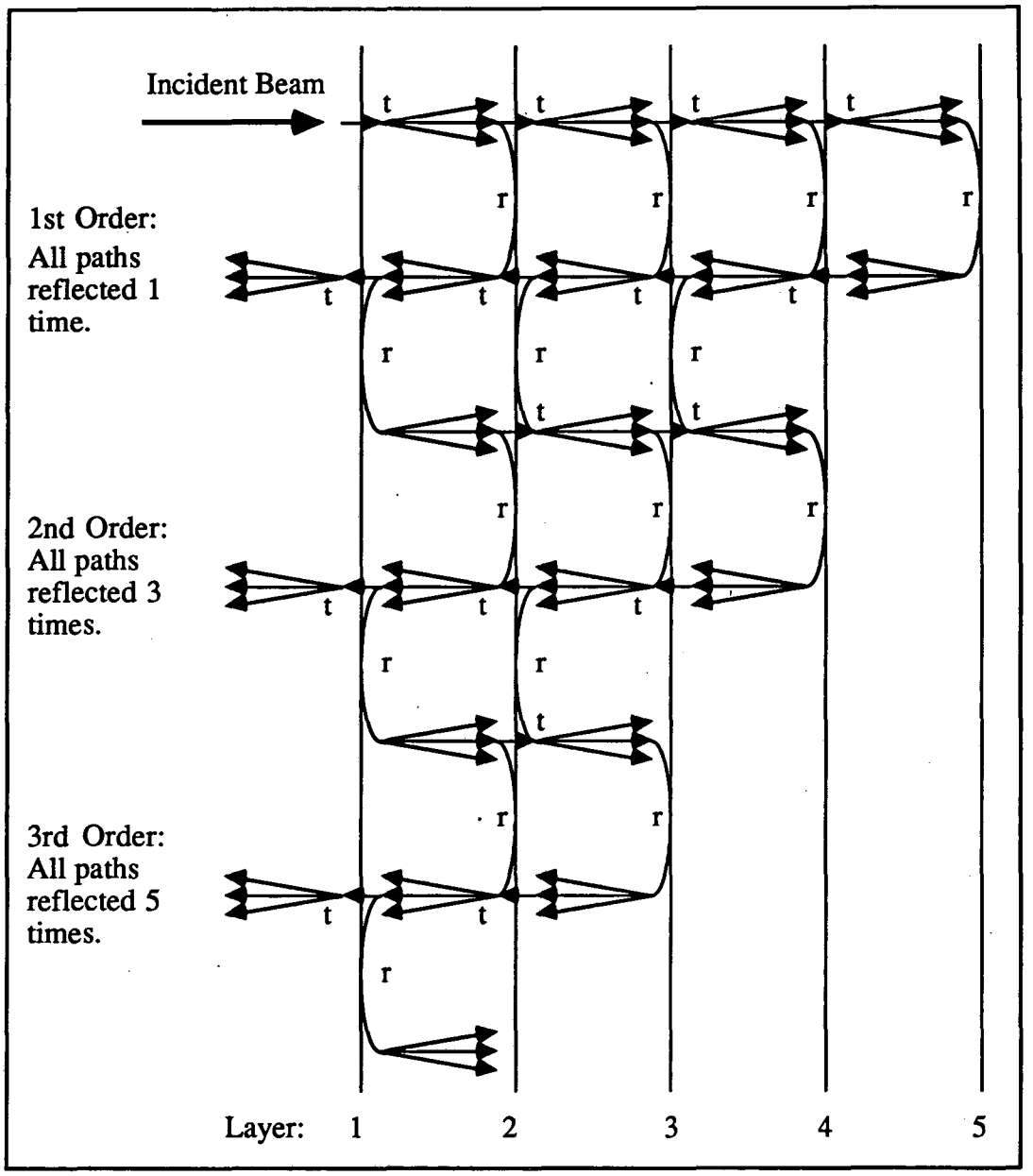

Fig. 5.2: Diagram of layer stacking using the RFS scheme. Each triplet of arrows represents the complete set of plane waves that travels from layer to layer. At each layer the set is either transmitted (t) or reflected (r). RFS is a perturbation method based on the assumption that reflection by any layer is weak. Therefore, the total reflectivity is expanded in terms of the number of reflections.[51]

R-factors have been developed, each having a different sensitivity to the features of the I-V curves such as peak position, relative peak height or peak widths. For this work, the Pendry R-factor has been utilized.[52] This R-factor attempts to treat the peak positions of large and small peaks with equal weight by utilizing the first derivative of the theoretical and experimental I-V curves. It is based on the logarithmic derivative of the I-V curves ($L = (dI/dE)/I$) arranged so as to avoid singularities at $I=0$ by defining the function

$$Y = L/(1 + (V_{oi}L)^2) \tag{5.5}$$

where $2V_{oi}$ may be approximated as the average experimental peak width. Pendry's R-factor is then defined by

$$R = \left(\int (Y_{expt} - Y_{th})^2 \, dE\right) / \left(\int [(Y_{expt})^2 + (Y_{th})^2] \, dE\right) \tag{5.6}$$

As a rule of thumb, a difference of 20% in the Pendry R-factors between two different models is considered sufficient to disregard the higher R-factor model. This percentage is obtained from a conservative statistical error analysis and is a function of the total energy range of the data base.

5.3 Experimental

The Varian UHV system described in sec. 3.2 was utilized for the AES and LEED I-V studies. The β-SiC (100) samples utilized were 4-6 μm thick films grown on Si (100) wafers via chemical vapor deposition. The samples were provided by L. Matus of NASA Lewis Research Center.[53] Previous research has shown that these films yield LEED patterns which are superpositions of patterns originating from surface domains rotated 90° relative to each other.[1] To generate a larger

experimental data base (unaffected by domain averaging) a single-domain pattern is preferable. Thus, our studies utilized β-SiC (100) films grown on Si (100) wafers cut 0.5° towards the (110) direction. These off-normal β-SiC (100) films exhibited only 1-domain LEED patterns. The samples were mounted on an off-axis manipulator capable of independent azimuthal rotation. The samples were resistively heated using a constant current power supply. The removal of oxide from the β-SiC surface was performed in situ by heating the sample to 1,175 K and placing it 2.5 cm from a resistively heated 2 cm^2 silicon wafer at approximately 1,300 K. The flux of silicon atoms obtained from the silicon wafer removed the oxide from the β-SiC surface as $SiO_{(g)}$ and also allowed the surface silicon/carbon ratio to be controlled.

The LEED data were collected using a silicon-intensified-target video camera. The video signal was digitized utilizing a video conversion board mounted in a Everex 386 PC, which was also used for data storage. The LEED data were taken at normal incidence between 30 and 230 eV, in 2 eV increments. At each energy, 128 video images were averaged to increase the signal-to-noise ratio. The LEED I-V curves were then generated from the stored diffraction images. The I-V curves of symmetrically equivalent beams were compared to check for normal incidence.

5.4 The β-SiC (100)-c(2x2) Surface

5.4.1 Introduction

Several researchers have reported that high temperature annealing of the β-SiC (100)-(2x1) surface produces a surface reconstruction exhibiting a c(2x2) LEED pattern.[28,54,55] No analogous structure has been reported for GaAs (100), Si (100), or diamond (100). The ideal silicon-terminated unreconstructed β-SiC (100)-(1x1) surface is illustrated in fig. 5.3a. A variety of surface reconstruction models has been proposed for the β-SiC (100)-c(2x2) surface. Dayan proposed that the c(2x2) surface is terminated in a complete layer of silicon, with silicon dimers arranged in a staggered pattern, as shown in fig. 5.3b.[55] Kaplan, believing the surface to be silicon deficient relative to the (2x1) reconstruction, proposed that the surface is terminated in 0.5 monolayer (ML) of silicon, with the silicon atoms positioned in alternating carbon hollow sites.[32] (fig. 5.3c) Based on medium energy ion scattering (MEIS) results, Hara et al. proposed that the c(2x2) surface is terminated in a complete monolayer of carbon.[50] However, a more detailed surface structure analysis was not reported.

Determining the c(2x2) surface structure using AES or MEIS is hampered by the fact that several of the possible β-SiC (100) reconstructions can exist on the surface simultaneously, dependent only on the local atomic composition. When this is the case, AES and MEIS sample multiple reconstructions simultaneously, due to the relatively large analysis areas of the techniques. A structural determination of the c(2x2) surface via LEED I-V analysis is not dramatically affected by the simultaneous presence of the (3x2), (5x2) or (2x1) surface reconstructions. This is due to the fact that these reconstructions cannot add diffraction intensity to the half-order spots of the c(2x2) pattern.

Two different routes were utilized to prepare the c(2x2) surface reconstruction. As previously mentioned, annealing the (2x1) surface

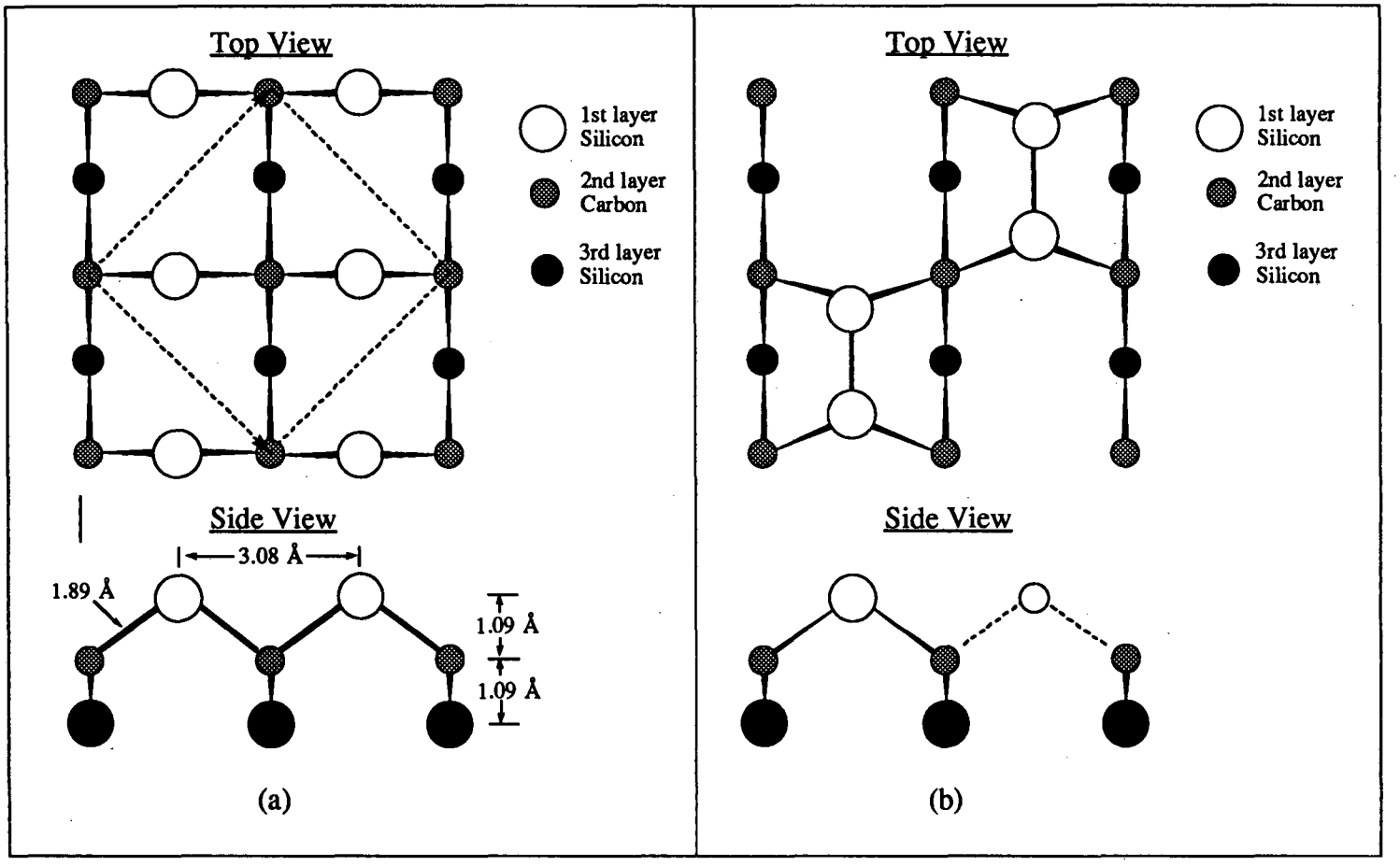

Fig. 5.3: Silicon -terminated models for the beta-SiC (100)-(1x1) and c(2x2) surfaces: a) the ideal unreconstructed (1x1) surface with a superimposed c(2x2) unit cell, b) the staggered Si dimer model, c) Si in C hollow sites and d) Si in C bridge sites.

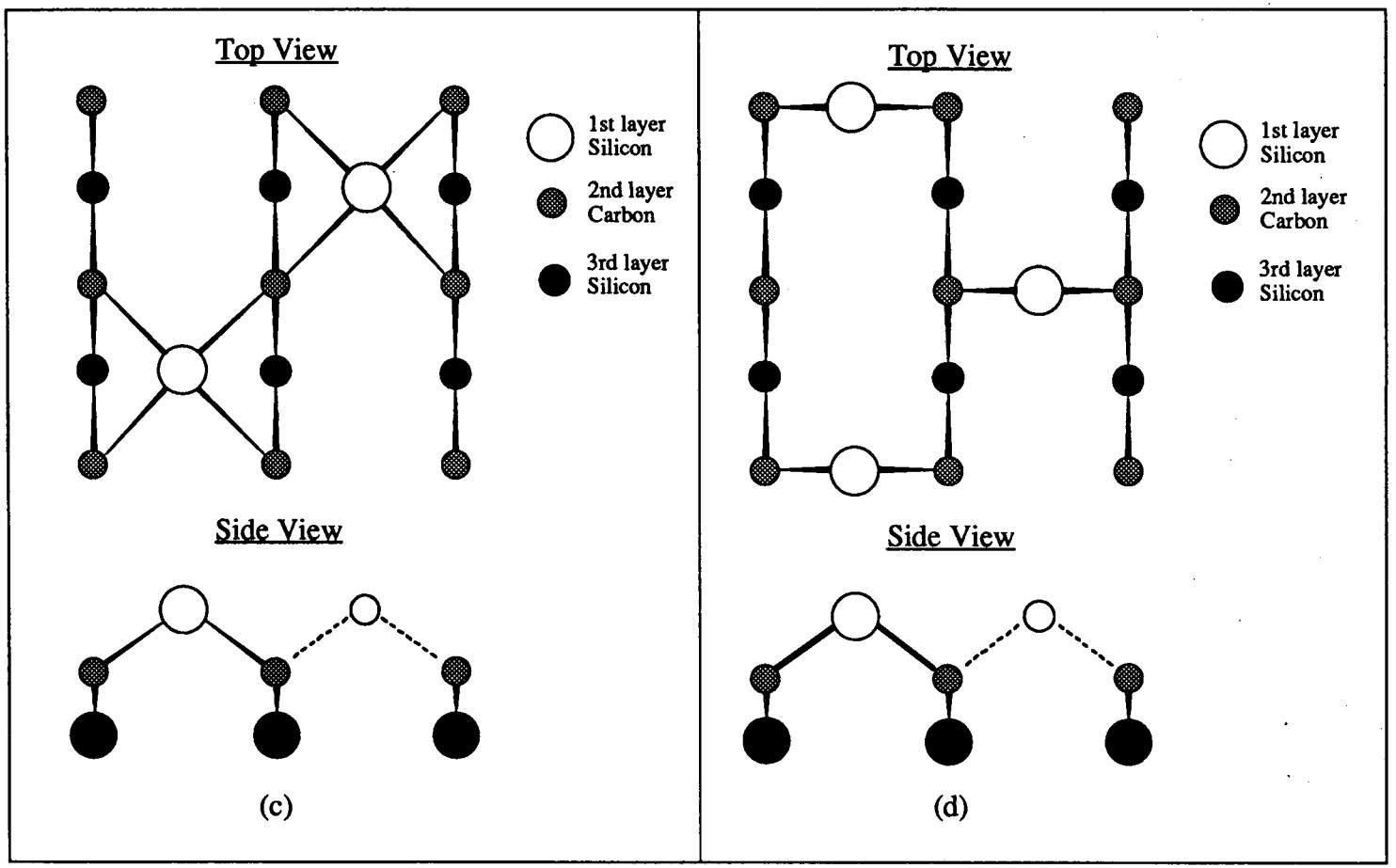
Top View
1st layer Silicon
2nd layer Carbon
3rd layer Silicon
Side View
(c)
Top View
1st layer Silicon
2nd layer Carbon
3rd layer Silicon
Side View
(d)

Fig. 5.3

above 1,300 K removes surface silicon via sublimation, producing a slightly diffuse c(2x2) pattern. Secondly, a sharper c(2x2) pattern may be obtained by the deposition of surface carbon, produced by exposing the (2x1) surface at 1,125 K to ethylene (C_2H_4) gas. A comparison of the LEED I-V curves of both c(2x2) surfaces showed them to share many features, but with some clear differences. The structural analysis indicated that both c(2x2) surfaces were terminated with C_2 groups in staggered silicon bridge sites. Evidence of weak silicon dimer bond formation in the second atomic layer was found for the c(2x2) surface produced by silicon sublimation, but not for the c(2x2) surface produced by C_2H_4 exposure. This suggests that hydrogen, released by the thermal decomposition of C_2H_4, saturated silicon dangling bonds and suppressed silicon dimer formation.

5.4.2 Surface Preparation

Two different techniques were utilized to produce the c(2x2) surfaces. The first required the removal of surface silicon from a (2x1) or (3x2) surface by high temperature annealing in UHV. At approximately 1,300 K, the (2x1) to c(2x2) conversion required 10-15 minutes of annealing, while a (3x2) surface required an additional 5-10 minutes. A better ordered c(2x2) surface could be produced by exposure of the (2x1) surface at 1,125 K to 100 L of C_2H_4 (1 Langmuir = 10^{-6} Torr·sec). Exposure of this c(2x2) to additional C_2H_4 produced no change in the LEED pattern or the AES spectra.

The eight independent diffraction beams analyzed for the c(2x2) produced by C_2H_4 exposure are shown in fig. 5.4. The cumulative energy

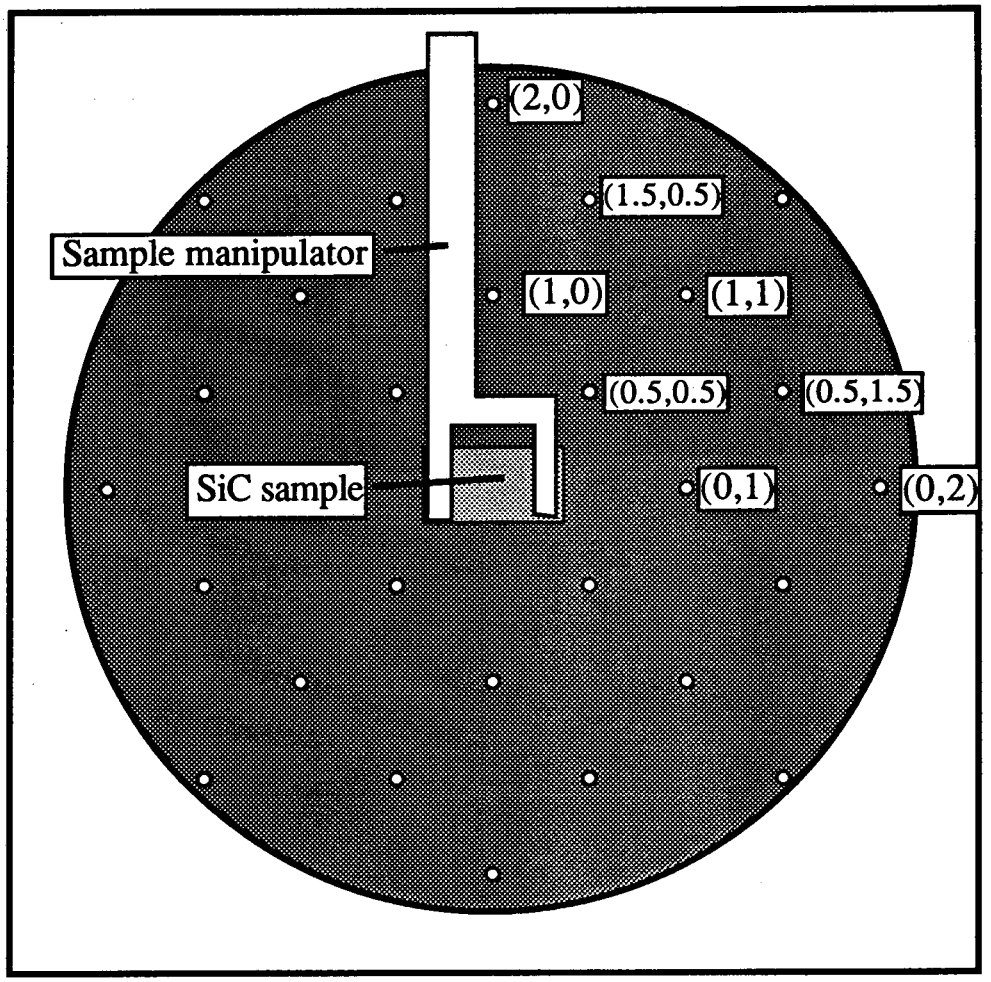

Fig. 5.4: Schematic of the beta-SiC (100)-c(2x2) LEED pattern and the diffraction spots measured for I-V curves.

range for the (0,1), (1,0), (1,1), (2,0), (0,2), (0.5,0.5), (1.5,0.5) and (0.5,1.5) beams was 870 eV. Due to the lower quality of the c(2x2) produced by silicon sublimation, only seven independent diffraction beams {(0,1), (1,0), (1,1), (2,0), (0.5,0.5), (0.5,1.5) and (1.5,0.5)} were utilized. These seven beams had a cumulative energy range of 818 eV. The I-V curves due to the two preparation methods are compared in fig. 5.5 and 5.6.

5.4.3 LEED Analysis and Structural Models Examined

The experimental I-V curves were analyzed in two stages. First, a conventional dynamical LEED analysis was performed, in which only first-layer reconstruction was allowed, keeping the bulk structure in deeper layers. This enabled us to identify the most promising candidate structures for further analysis. The analysis of the best candidate structures was then refined by allowing any first and second layer relaxations to occur which were compatible with the c(2x2) periodicity. This analysis was performed using the recently developed automated search method based on tensor LEED (TLEED).[56]

The initial calculations were performed using standard dynamical LEED theory.[57] Phase shifts for silicon and carbon were derived from an infinite bulk lattice calculation using Herman-Skillman wave functions. A composite layer consisting of the first and second atomic layers was treated using matrix inversion, although only the first atomic layer was allowed to reconstruct. The use of a composite layer allows for possible small first to second layer distances. The layers were then stacked using layer doubling. Surface vibrations were included via a Debye-Waller

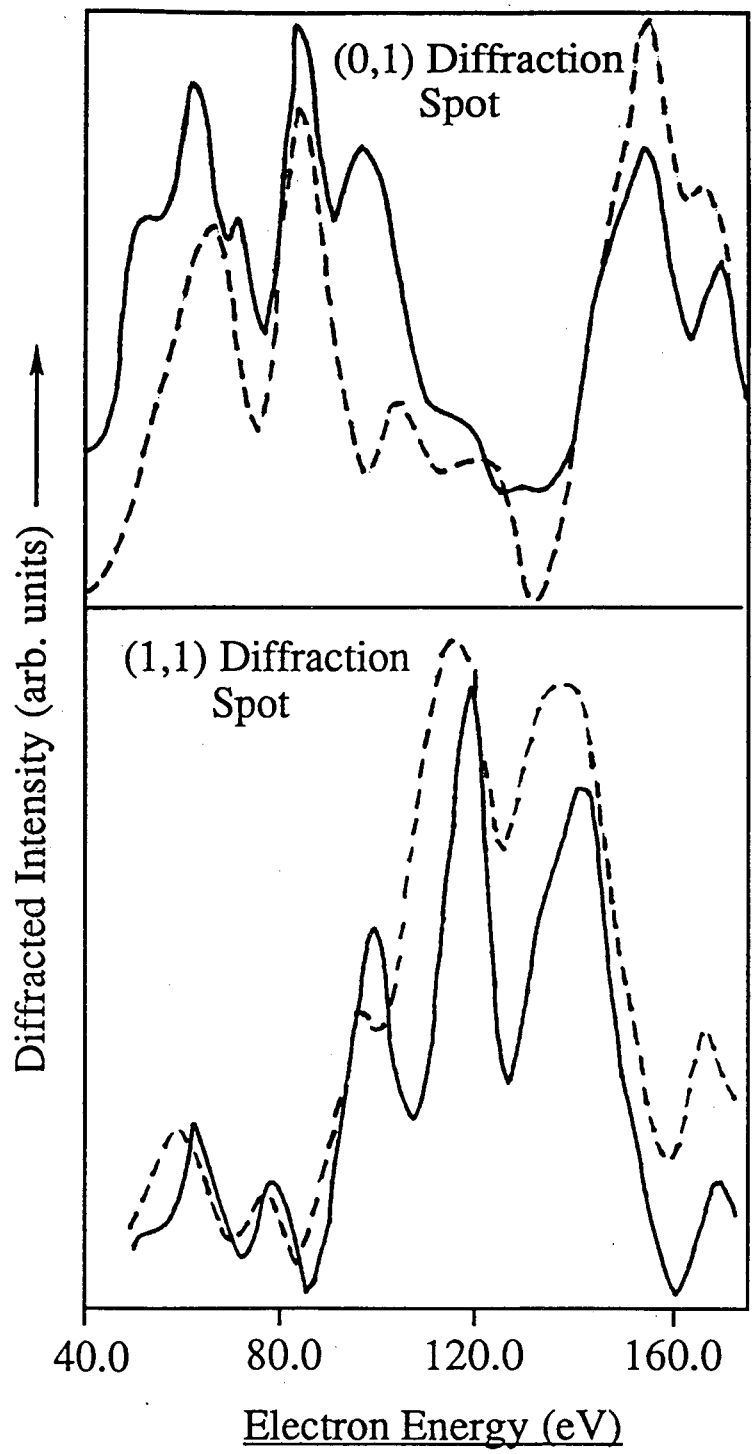

Fig. 5.5: The I-V curves of the (0,1) and (1,1) beams of the c(2x2) produced by Si sublimation (solid line) and C_2H_4 exposure (dashed line).

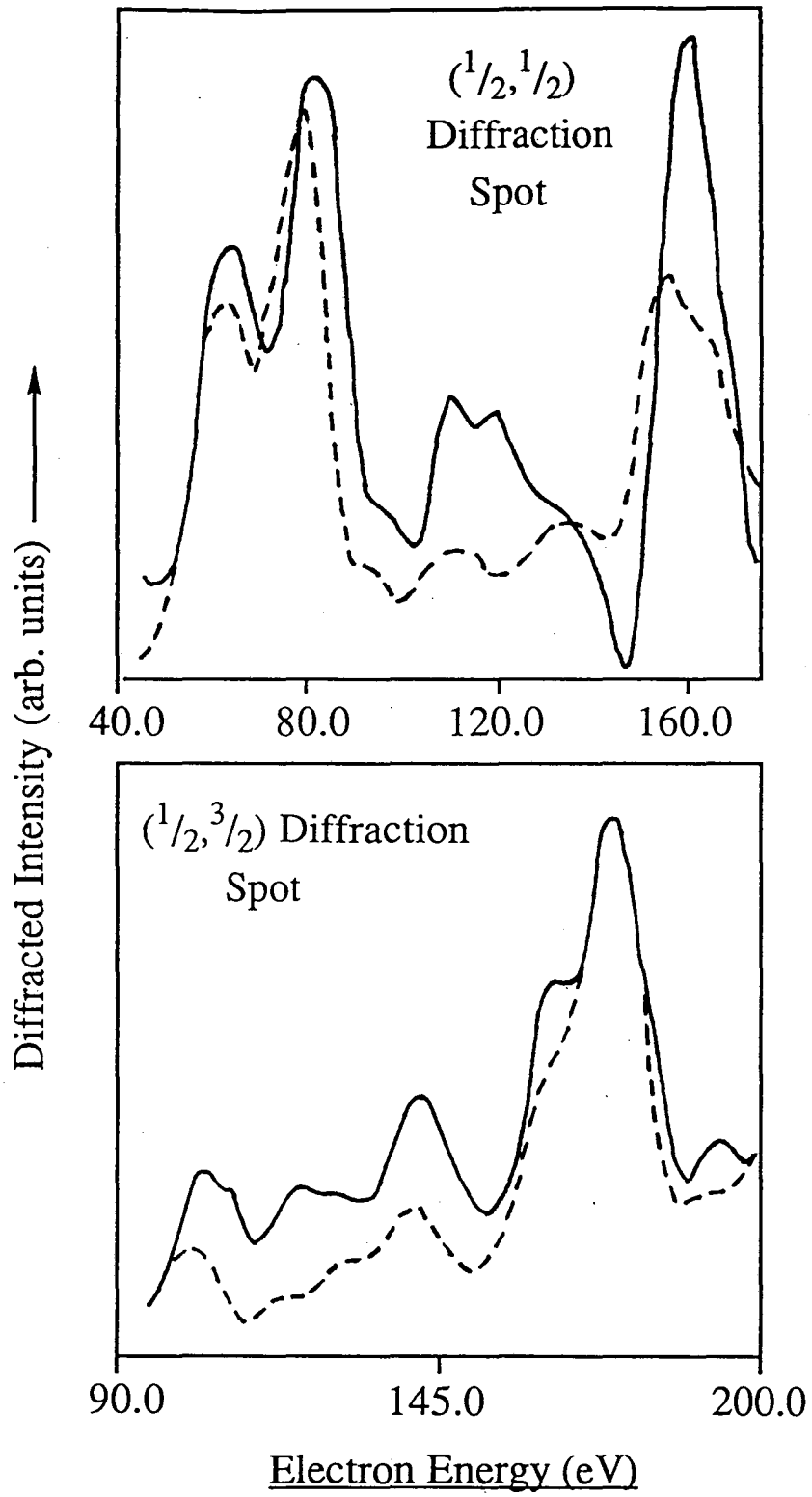

Fig. 5.6: The I-V curves of the (0.5,0.5) and (0.5,1.5) beams of the c(2x2) produced by Si sublimation (solid line) and C_2H_4 exposure (dashed line).

factor. A Debye temperature equal to the bulk Debye temperature of 1,430 K was used throughout both the dynamical and tensor LEED calculations. A damping term of -5 eV was used during this stage. The theoretical and experimental I-V curves were then compared using the Pendry R-Factor.

The analysis by tensor LEED allowed four atoms in the first and second layers to move independently in all three dimensions. Thus, 12 structural parameters were optimized simultaneously, in addition to the muffin-tin zero. TLEED utilizes first order perturbation theory to express the change in amplitude of the scattered LEED intensities resulting from small displacements (< 0.4 Å) of the surface atoms away from a reference structure. The first step in the method performs a dynamical LEED calculation for a reference structure. In addition, the expansion coefficients for the perturbation series are evaluated in the form of a tensor. In the second stage, the tensor is used to perform a fast and efficient perturbative LEED calculation. This stage is coupled with an optimization routine that allows the relatively quick location of a R-factor minimum in structural parameter space. TLEED has previously been applied to the Mo (100)-c(2x2)-S [58] and Rh (111)-(2x2)-C_2H_3 systems.[59]

The TLEED method currently requires layer stacking to be performed using renormalized forward scattering (RFS). However, convergence problems were experienced using this technique together with the -5 eV damping term used in the conventional dynamic calculations. These problems were removed by increasing the damping to -6 eV. While this results in a broadening of the peaks in the theoretical I-V spectra, it should not significantly affect the structural outcome.

Seven different models were analyzed for the c(2x2) surface. In addition to the two models discussed previously (fig. 5.3b and 5.3c), a surface terminated with silicon atoms in staggered carbon bridge sites (fig. 5.3d) was examined. Based on the MEIS results of Hara et al., the carbon-terminated analogs of these models were also examined: i) a surface terminated with staggered carbon dimers (fig. 5.7a), ii) carbon atoms in silicon hollows (fig. 5.7b) and iii) carbon atoms in silicon bridges (fig. 5.7c). Lastly, based on the reported adsorbed state of C_2H_4 on Si (100), a surface with C_2 groups in silicon bridging sites (fig. 5.7d) was examined.[60]

5.4.4 Results and Discussion

According to AES, the atomic compositions of the c(2x2) surfaces produced by silicon sublimation or by C_2H_4 exposure were very similar (fig. 5.8). As fig. 5.8 shows, the c(2x2) surfaces exhibited a lower Si/C AES ratio than the (2x1) surface. Assuming the (2x1) surface to be analogous to the Si (100)-(2x1), the AES results indicated that the topmost atomic layer of both c(2x2) surfaces was either a mixed Si/C layer or was composed entirely of carbon atoms.

The results of the theoretical fitting of the I-V curves using the conventional dynamical LEED analysis are shown in table 5.1. These calculations clearly favored the model in which C_2 groups bridge silicon atoms. The muffin-tin zero for this model optimized at -10 ± 1 eV. A qualitatively similar model has been reported for C_2H_4 adsorbed on the Si (100)-(2x1) surface, in which the C_2H_4 molecule bonds on the silicon dimer, maintaining the (2x1) surface symmetry.[60] In addition, our

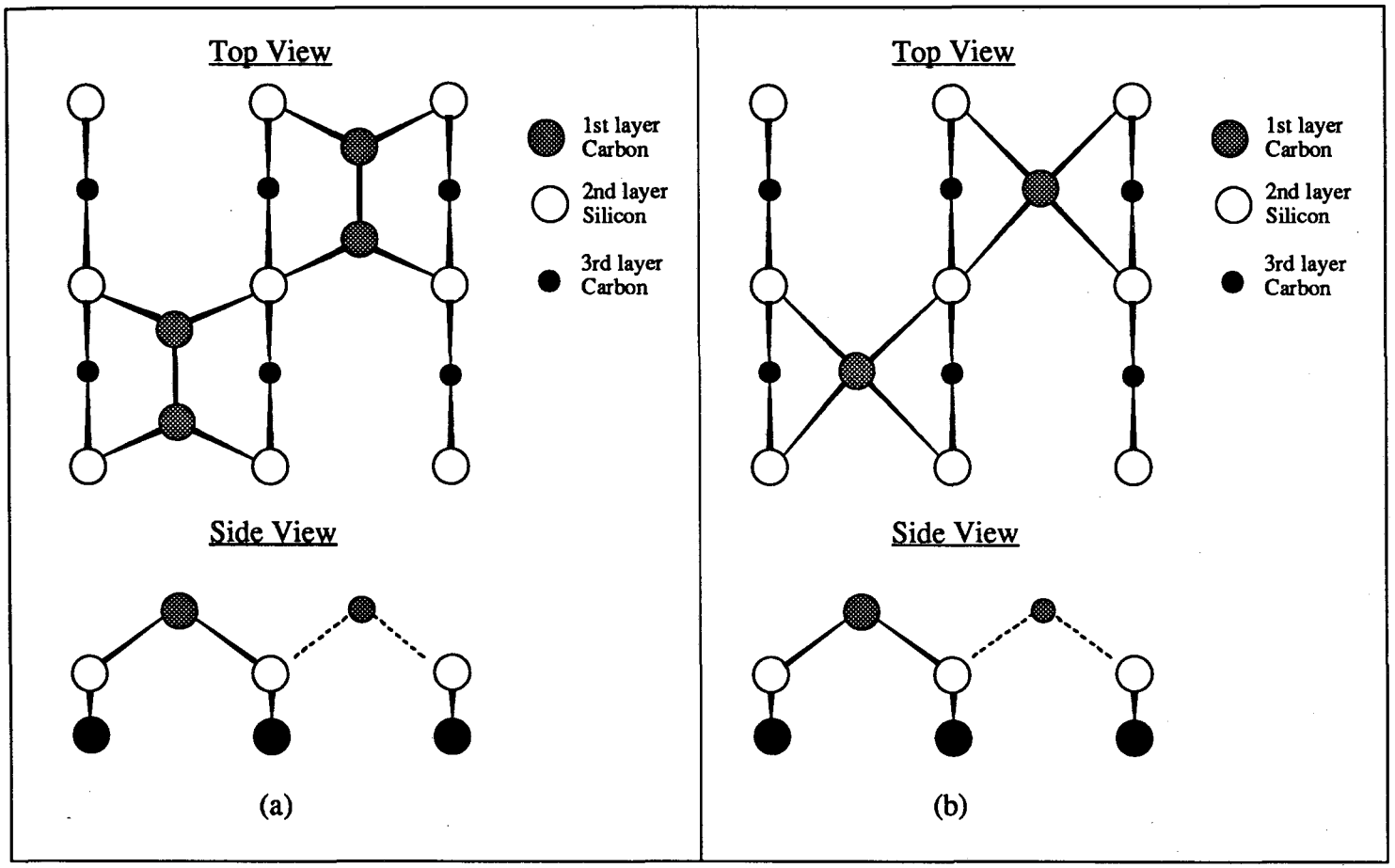

Fig. 5.7: Carbon-terminated trial models for the beta-SiC (100)-c(2x2) surfaces: a) the staggered C dimer model, b) C in Si hollow sites, c) C in Si bridge sites and d) C_2 groups in Si bridge sites.

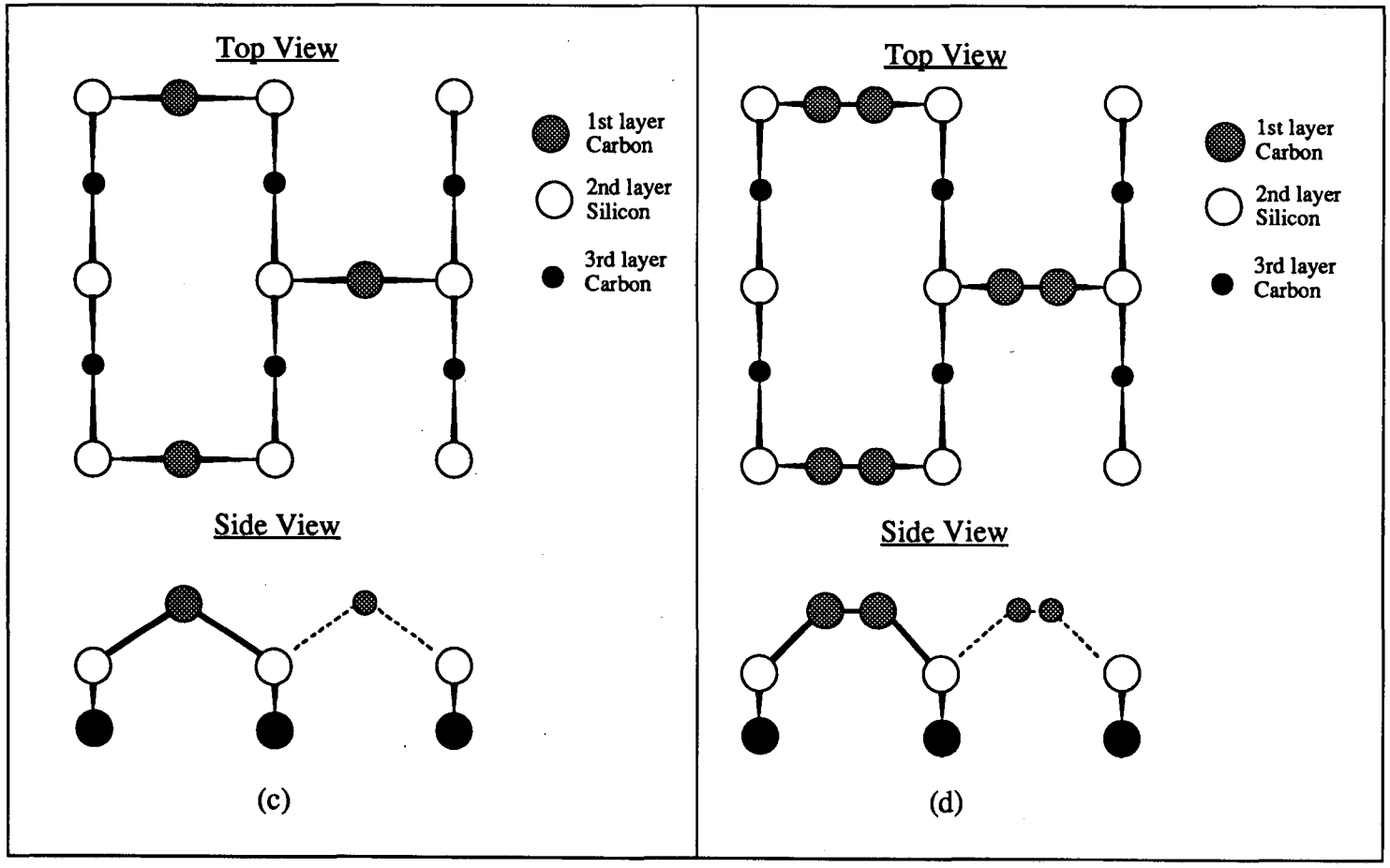
Top View
1st layer Carbon
2nd layer Silicon
3rd layer Carbon
Side View
(c)
Top View
1st layer Carbon
2nd layer Silicon
3rd layer Carbon
Side View
(d)

Fig. 5.7

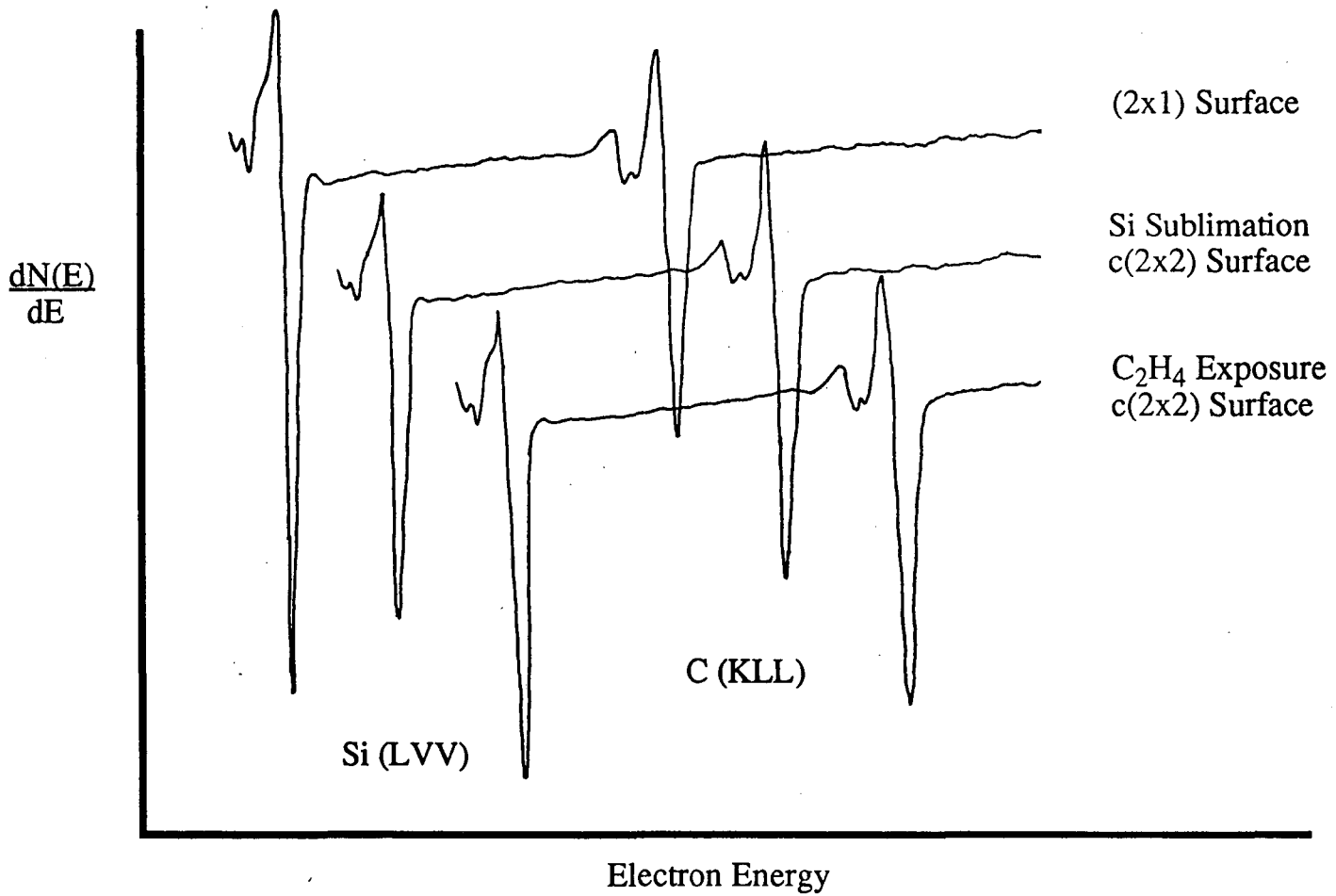

Fig. 5.8: AES spectra of the beta-SiC (100)-(2x1) and c(2x2) surfaces.

Table 5.1: Models of the β-SiC (100)-c(2x2) Examined Using Conventional Dynamical LEED.

c(2x2) via C_2H_4 exposure

Model	Vertical Height Range [a,b]	Optimized Vertical Height	Dimer Length Range[a]	Optimized Dimer Length	Pendry R-Factor
Staggered Si dimers	1.0-1.6	-----	2.15-3.00	----	*See below
Staggered C dimers	1.0-1.6	1.32	1.20-1.60	1.46	0.31
Si in C hollows	0.0-1.4	0.77	----------	----	0.35
C in Si hollows	0.0-1.4	0.20	----------	----	0.28
Si in C bridges	0.0-1.4	0.60	----------	----	0.36
C in Si bridges	0.0-1.4	0.36	----------	----	0.33
C_2 in Si bridges	1.0-2.0	1.62	1.13-1.43	1.26	0.24

c(2x2) via Si sublimation

Model	Vertical Height Range [a,b]	Optimized Vertical Height	Dimer Length Range[a]	Optimized Dimer Length	Pendry R-Factor
Staggered Si dimers	1.0-1.6	----	2.15-3.00	----	*See below
Staggered C dimers	1.0-1.6	1.23	1.20-1.60	1.32	0.32
Si in C hollows	0.0-1.4	0.89	----------	----	0.36
C in Si hollows	0.0-1.4	0.33	----------	----	0.35
Si in C bridges	0.0-1.4	0.38	----------	----	0.34
C in Si bridges	0.0-1.4	0.34	----------	----	0.36
C_2 in Si bridges	1.0-2.0	1.62	1.13-1.43	1.25	0.27

(a) All heights and lengths are in angstroms (Å).

(b) The vertical height is the distance between the 1st and 2nd atomic layers, with the 2nd layer in its bulk-like position.

* For the staggered Si dimer model, no R-factor minimum was found within the explored ranges.

model agrees with the MEIS results of Hara et al., since the terminating atomic layer of the model consists of a monolayer of carbon.[50]

Several characteristics of the c(2x2) surface support our preferred model. First, exposure of the (2x1) surface to CH_4 at elevated temperatures does not produce a c(2x2) pattern, implying a C--C surface bond is necessary to create the c(2x2) reconstruction. Secondly, the oxidation rate of the c(2x2) surface is lower than that of the (2x1) and (3x2) surfaces.[36] Previous research has shown that the rate of oxidation increases with increasing surface silicon concentration.[27] Our preferred model, in which the topmost atomic layer is only carbon, would not be expected to oxidize quickly. Lastly, exposure of the c(2x2) surface to H_2 does not change the LEED pattern symmetry, suggesting that the c(2x2) structure is not created by staggered silicon dimers. The (2x1) surface is readily converted to a (1x1) surface by exposure to 10^{-6} Torr of H_2 at 1,125 K, indicating that H_2 exposure dissociates silicon dimers.

Based on the conventional dynamical LEED results, only the staggered carbon dimer and bridging C_2 groups models were further refined using tensor LEED. Once again, the calculations favored the C_2 bridging model, as shown in table 5.2. However, by allowing 2nd layer relaxations it was determined that the c(2x2) surface produced by C_2H_4 exposure was slightly different than the one produced by Si sublimation. For the surface produced by C_2H_4 exposure, TLEED results showed no significant changes from the conventional dynamical LEED results previously discussed (fig. 5.9a). Tensor LEED gave a 2% contraction (0.02 Å) in the 2nd and 3rd layer interatomic distance, although this change is well within the uncertainty of the analysis (approximately 0.05 Å). The optimized muffin-tin zero in this case was -9 ± 1 eV.

Table 5.2: Models of the β-SiC (100)-c(2x2) Examined Using Tensor LEED.

Model	Optimized Vertical Height[a]	Optimized C--C Bond Length[a]	Pendry R-Factor
c(2x2) via C_2H_4 exposure			
Staggered C dimers	1.32	1.46	0.31
C_2 in Si bridges	1.62	1.25	0.24
c(2x2) via Si sublimation			
Staggered C dimers	1.23	1.32	0.32
C_2 in Si bridges	1.60	1.31	0.22

(a) All heights and lengths are in angstroms (Å).

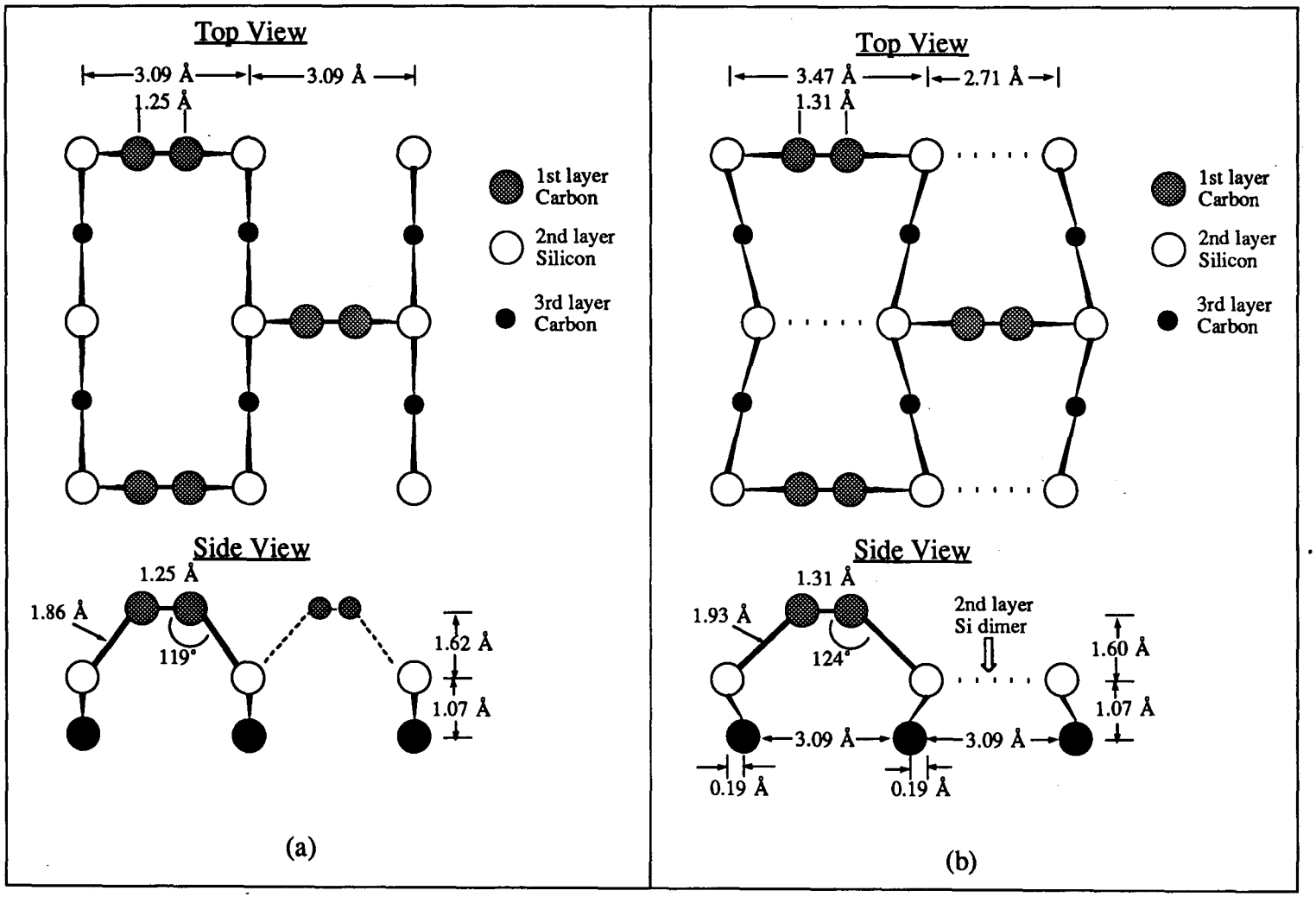

Fig. 5.9: The best-fit surface structures for the c(2x2) produced by a) ethylene exposure and b) Si sublimation.

For the Si sublimation c(2x2) data, TLEED results suggested the formation of weak 2nd layer silicon dimers. (fig. 5.9b) By allowing 2nd layer relaxation, the R-factor was lowered from 0.27 to 0.22. In this case the optimized muffin-tin zero was -11 ± 1 eV. This weak silicon dimer has a bond length of 2.71 Å, which is considerably longer than dimers found on the Si (100)-(2x1) surface (2.47 Å).[61] However, this long silicon dimer bond length results in a C--C bond distance of 1.31 Å, which suggests the surface carbon are sp^2 hybridized. Assuming the C_2 groups to be double bonded, this leaves the surface carbon with one sp^2 dangling bond. Our calculated Si--C distance of 1.93 Å agrees well with the bulk Si--C bond distance of 1.89 Å. This calculated configuration results in a C-C-Si bond angle of 124° vs. 120° for ideal sp^2 carbon. Hence, the model of C_2 groups in bridging sites would appear to be able to exist without a high degree of strain. Our model for the c(2x2) surface is also favored by the total energy calculations of Badziag, although with somewhat different bond lengths for the bridging C_2 group.[62]

The fact that the Si sublimation and C_2H_4 exposure I-V data sets gave somewhat different surface structures by TLEED suggests that hydrogen plays a role in the c(2x2) surface formed by C_2H_4 exposure. We propose that hydrogen, released by the thermal decomposition of C_2H_4 at 1,125 K, could be bonding to surface silicon and/or carbon atoms. This could explain the apparent lack of silicon dimer formation in the 2nd atomic layer of the c(2x2) surface formed by C_2H_4 exposure.

Tensor LEED calculations showed no significant differences from the conventional dynamical LEED results for the staggered carbon dimer model suggested by Bermudez and Kaplan.[63] The optimized R-factors for this model, listed in table 5.2, are significantly higher than those found

for the bridging C_2 model. As shown in fig. 5.7a, the staggered carbon dimer model requires significant distortion in the sp^3 bonding of the silicon atoms in the second atomic layer. Badziag's total energy calculations have predicted the staggered carbon dimer geometry to have substantially higher energy than the bridging C_2 groups model.[62]

5.5 The β-SiC (100)-(2x1) Surface

5.5.1 Introduction

Since its discovery by Dayan in 1985, the β-SiC (100)-(2x1) surface has been modeled as a dimer reconstruction, similar to that found with Si and Ge (100) surfaces.[1] In this model, pairs of adjacent rows of silicon atoms move towards each other to form dimers, reducing the number of unsaturated surface bonds. (fig. 5.10) This model is supported by the work of Parrill and Chung, who reported AES lineshape evidence of Si--C and Si--Si bonding in the (2x1) surface region.[4] The discovery of a c(4x2) reconstruction on highly smooth β-SiC (100) samples introduced the possibility that both the (2x1) and c(4x2) reconstructions are formed from an array of asymmetric dimers, as shown schematically in fig. 5.11.[32] A similar model has been invoked to explain the (2x1) to c(4x2) transformation of Ge and Si (100) surfaces below 220 and 150 K, respectively.[64,65] Interestingly, the β-SiC (100)-c(4x2) shows no thermal disordering as high as 875 K.[32]

Total energy calculations of the β-SiC (100)-(2x1) surface predicts the dimer asymmetry is caused by charge transfer within the dimer, which

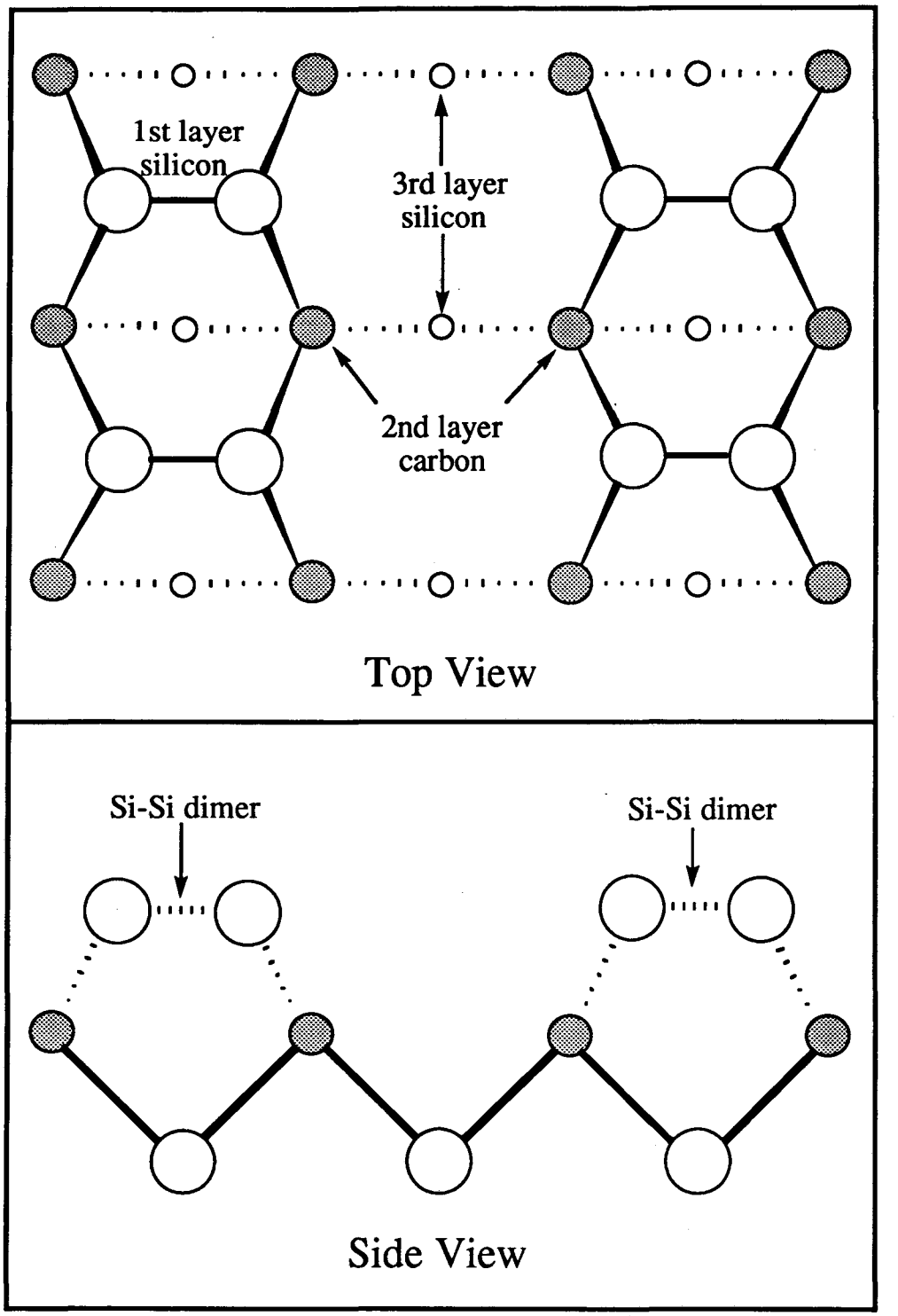

Fig. 5.10: The silicon dimer model for the beta-SiC (100)-(2x1) surface reconstruction.

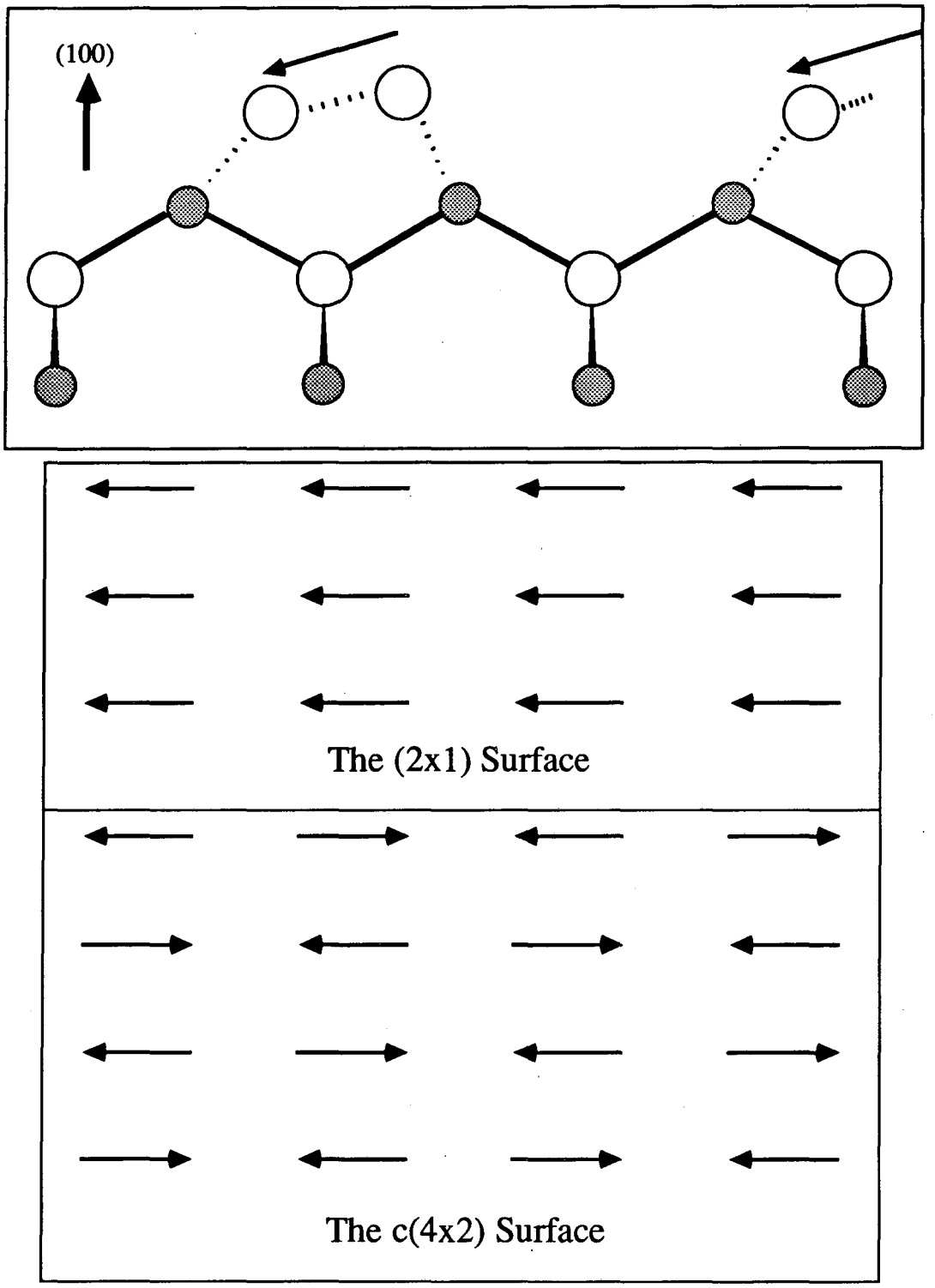

Fig. 5.11: The asymmetric silicon dimer model for the beta-SiC (100) (2x1) and c(4x2) surfaces. The direction of the dimer arrows is arbitrary and is for illustration purposes only.

causes it to buckle, as shown in fig. 5.12.[66] This configuration is stabilized by the electrostatic attraction of the positively charged lower Si atom with the negatively charged C atoms in the second layer. This electrostatically driven buckling is also predicted to occur in the third and fourth atomic layers.

Tensor LEED was utilized to analyze the structure of the first three atomic layers of the β-SiC (100)-(2x1) surface reconstruction. Preliminary results indicate the (2x1) surface is terminated with buckled silicon dimers. However, the results do not find the theoretically predicted buckling in the third and fourth atomic layers.

5.5.2 LEED Analysis and Structural Models Examined

The off-normal β-SiC (100) film used for the c(2x2) surface reconstruction studies was again utilized in order to produce 1-domain (2x1) LEED patterns. The (2x1) surface reconstruction was prepared by first heating the β-SiC (100) surface to approximately 1,250 K for 10 min. in the presence of a silicon flux. (See section 5.3) Following the silicon exposure the surface was annealed in UHV for 10 min. at 1,275 K. This resulted in a (2x1) surface exhibiting a Si/C AES ratio of 1.8 vs. 1.0 for the carbon terminated c(2x2) surface. This indicated that the (2x1) surface is terminated by a complete layer of silicon atoms.

The five independent diffraction beams used in the analysis are shown in fig. 5.13. The cumulative energy range for the (0,1), (1,0), (1,1), (1,0.5) and (0,0.5) beams was 920 eV.

The analysis by tensor LEED allowed the atoms in the first three atomic layers to move independently in all three directions. Thus, 18

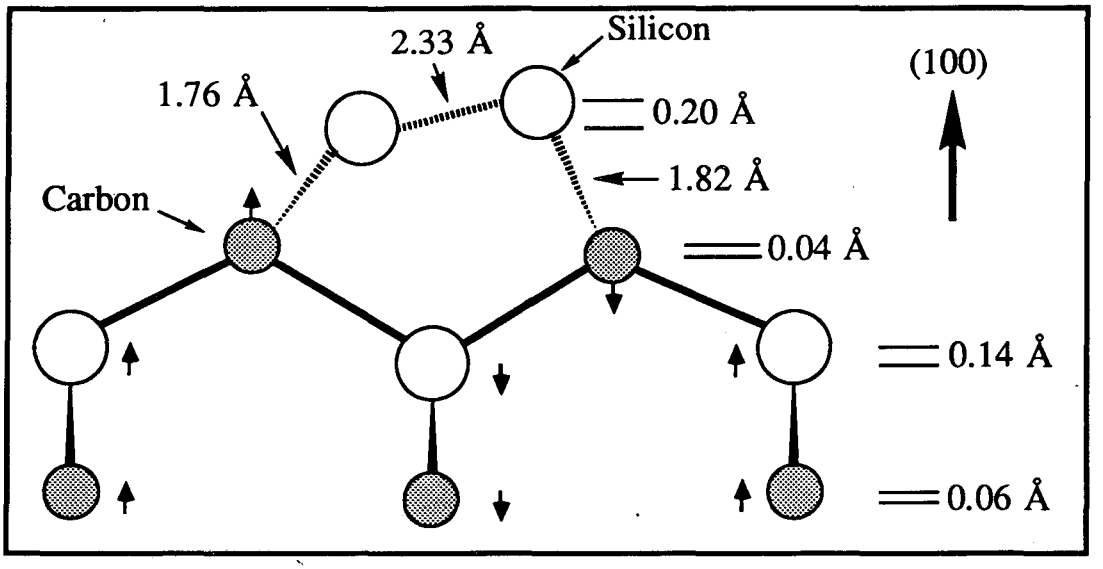

Fig. 5.12: The beta-SiC (100)-(2x1) surface reconstruction predicted by total energy calculations.[66] (Note: distances are not to scale)

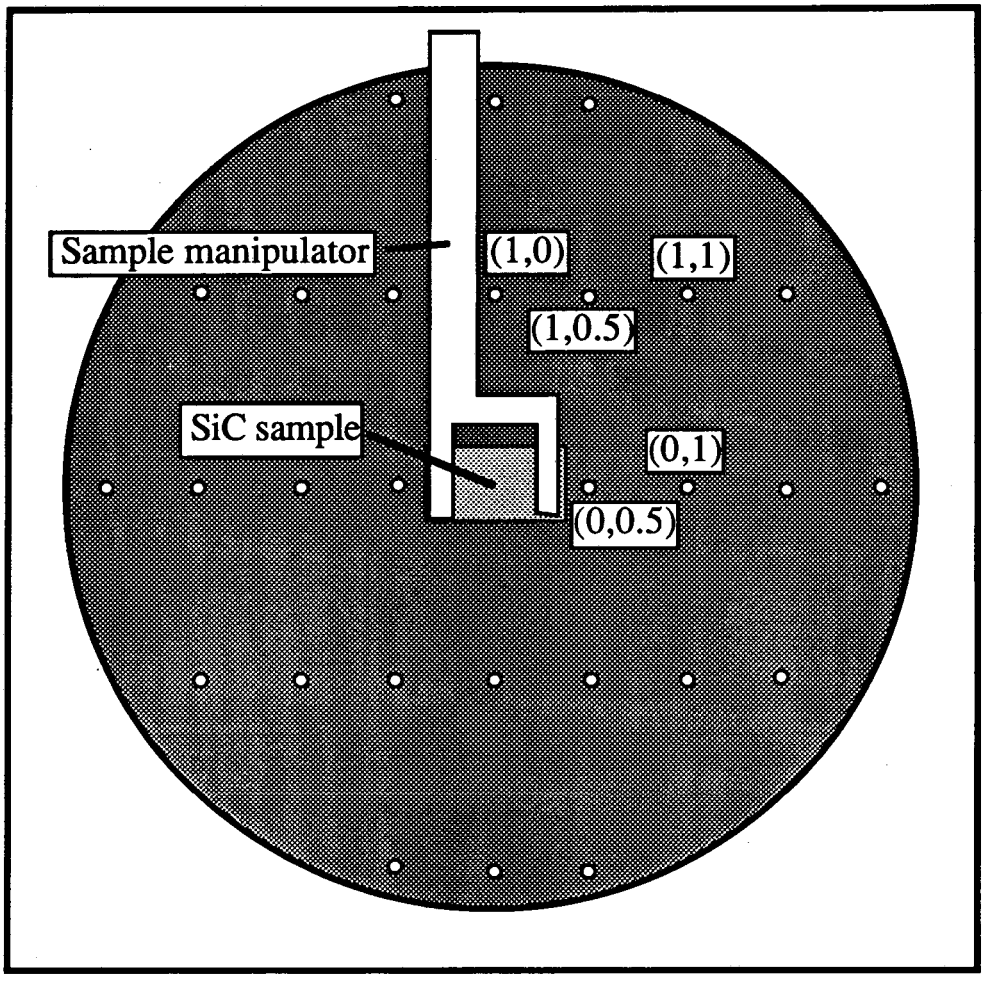

Fig. 5.13: Schematic of the beta-SiC (100)-(2x1) LEED pattern and the diffraction spots measured for I-V curves.

structural parameters were optimized simultaneously in addition to the muffin-tin zero. Layer stacking was performed using renormalized forward scattering coupled with a damping term of -6 eV and a Debye temperature of 1,430 K. Diffraction intensities above 160 eV were not calculated due to convergence problems associated with using RFS with the small interlayer distances of β-SiC.

Three different reference structures were utilized for the TLEED calculations of the (2x1) surface reconstruction. Reference structure 1, shown in fig. 5.14a, is a symmetric dimer model with a Si--Si bond length of 2.4 Å. Reference structures 2 and 3 (fig. 5.14b and 5.14c) are buckled dimer models, both with a Si--Si dimer length of 2.4 Å. The use of several reference structures is desirable when the atomic positions of multiple atoms are being optimized. This reduces the probability the TLEED automated optimization routine will find only a local R-factor minimum in the multi-dimensional structural parameter space.

5.5.3 Results and Discussion

Regardless of the starting reference structure, all three TLEED calculations optimized to the buckled dimer model shown in fig. 5.15. For this optimized model the Pendry R-factor was 0.27 and the muffin-tin zero point energy was -10 ± 1 eV. The optimized silicon dimer length of 2.31 Å is substantially shorter than that found on the Si(100)-(2x1) surface (2.47 Å).[61] However, our optimized dimer length and dimer buckling (0.20 Å) agree well with the total energy calculations of Craig and Smith (2.33 Å and 0.20 Å, respectively).[66] Their predicted subsurface buckling in the 3rd and 4th atomic layers (0.15 Å and 0.06 Å, respectively) does not

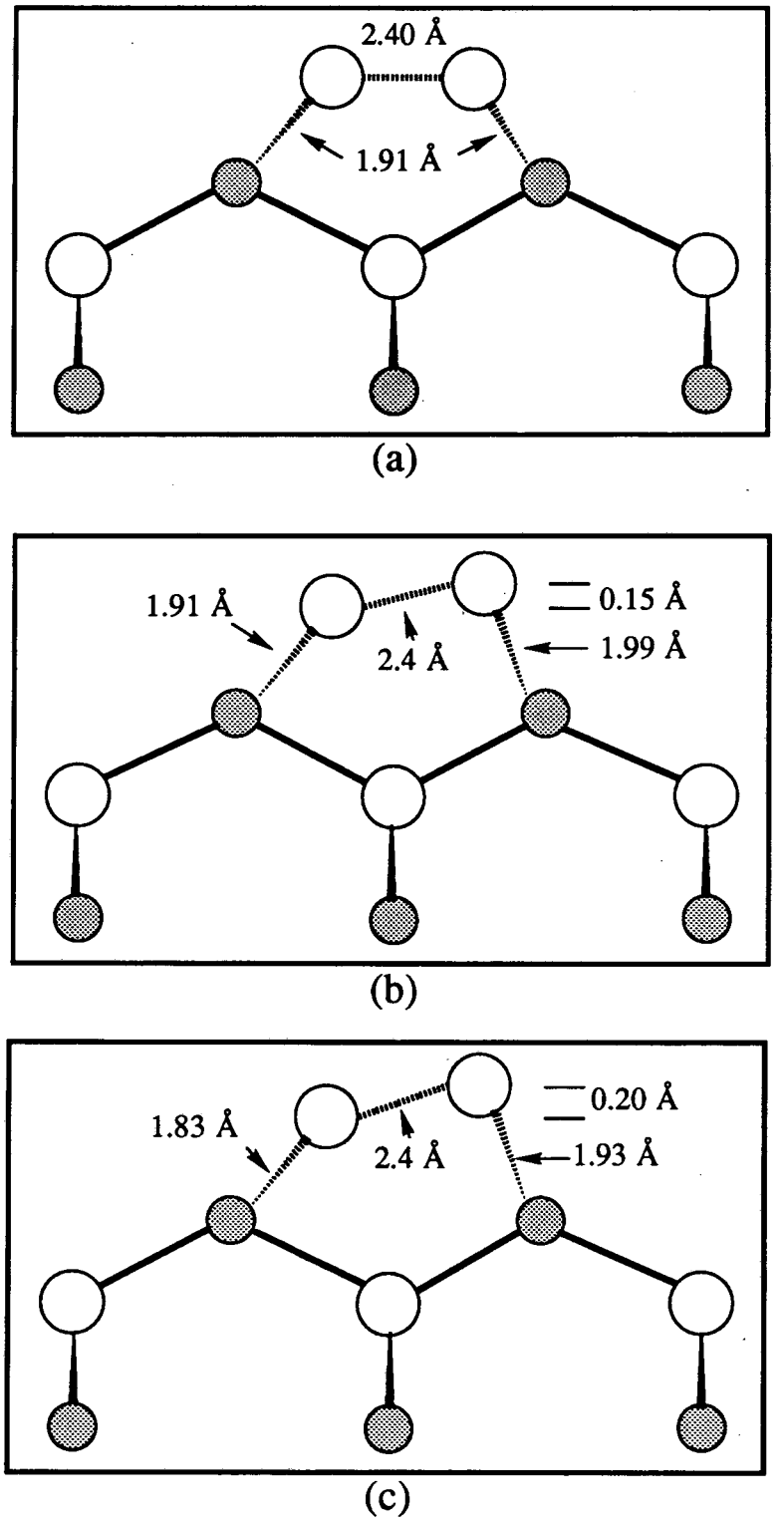

Fig. 5.14: Reference structures utilized for the TLEED analysis of the (2x1) reconstruction. In all three cases the atoms in the 2nd and 3rd layers are in their bulk-like positions. (Note: distances are not to scale)

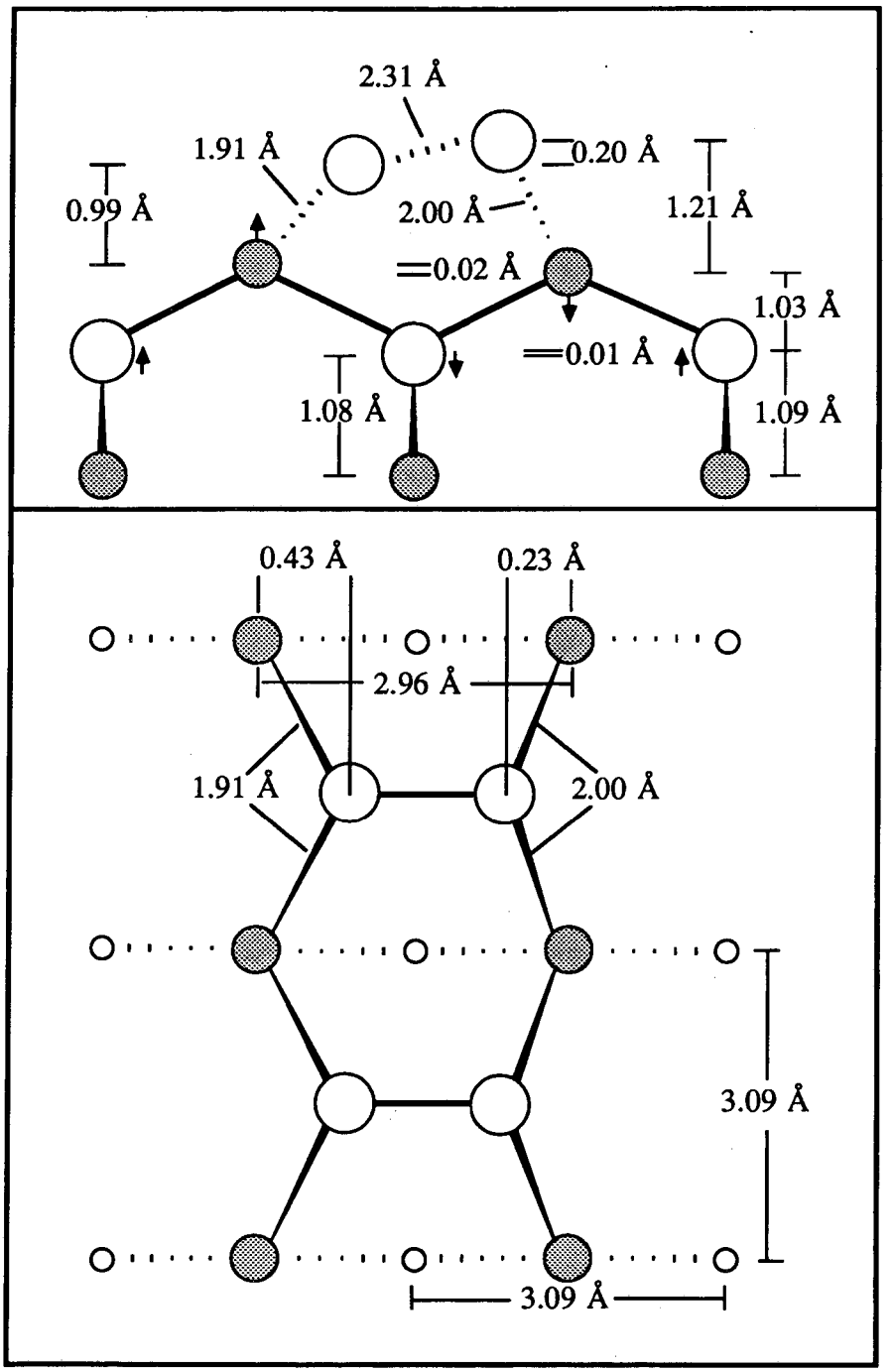

Fig. 5.15: The best fit surface structure for the beta-SiC (100)-(2x1) surface. (Note: distances are not to scale)

appear in our optimized results. This lack of buckling in our model may be due to the inability of RFS to calculate diffracted intensity above 160 eV due to the small interlayer spacing of β-SiC. Higher energy electrons, with their corresponding longer mean free paths, generally provide more subsurface structural information than lower energy (50-100 eV) electrons. Layer stacking using layer doubling should avoid these convergence problems and allow diffracted intensities to be calculated over the full energy range of the experimental data. Future plans include the modification of the current TLEED programs to allow calculations using layer doubling.

5.6 Conclusions

Beta-SiC, like other semiconductors, shows a range of surface reconstructions which are dependent on the surface composition and morphology. Dynamical LEED I-V analysis of the β-SiC (100)-c(2x2) surface showed the surface to be terminated with a staggered array of C_2 groups in silicon bridge sites. Weak silicon dimer bonds were found in the second atomic layer of the c(2x2) surface produced by silicon sublimation, but not in the c(2x2) surface produced by C_2H_4 exposure. We propose that hydrogen, released by the decomposition of C_2H_4, saturated surface dangling bonds and suppressed silicon dimer formation. Analysis of the β-SiC (100)-(2x1) reconstruction showed the surface to be terminated with buckled silicon dimers.

References

[1] M. Dayan, *J. Vac. Sci. Technol. A* **4(1)**, 38 (1986)

[2] S. Adachi, M. Mohri and T. Yamashina, *Surface Sci.* **169**: 479 (1985)

[3] L. Muehlhoff, W.J. Choyke, M.J. Bozack and J.T. Yates, Jr., *J. Appl. Phys.* **60(8)**, 2842 (1986)

[4] T.M. Parrill and Y.W. Chung, *Surface Sci.* **243**: 96 (1991)

[5] H. Jagodzinski and H. Arnold, in *Silicon Carbide, A High Temperature Semiconductor*, edited by J.R. O'Connor and J. Smiltens (Pergamon, New York, 1960), p. 136

[6] A. Taylor and R.M. Jones, in *Silicon Carbide, A High Temperature Semiconductor*, edited by J.R. O'Connor and J. Smiltens (Pergamon, New York, 1960), p. 147

[7] *Silicon Carbide--1968*, edited by H.K. Henisch and R. Roy (Pergamon, New York, 1969), p. 366

[8] C. Kittel, *Introduction to Solid State Physics, Sixth Edition*, John Wiley and Sons, Inc., (New York, Chichester, Brisbane, Toronto, Singapore, 1986), p. 22

[9] W.V. Wright, Jr. and F.T. Bartels, in *Silicon Carbide, A High Temperature Semiconductor*, edited by J.R. O'Connor and J. Smiltens (Pergamon, New York, 1960), p. 31

[10] *CRC Handbook of Chemistry and Physics, 64th Edition*, edited by R. Weast (CRC Press, Inc., Boca Raton, Florida, 1983) p. E-92

[11] *Silicon Carbide--1968*, op. cit., p. 368

[12] J. Powell, L. Matus and M. Kuczmarski, *J. Electrochem Soc.*, **134(6)**, 1558, (1987)

[13] S. Nishino, J. A. Powell and H. Will, *Appl. Phys. Lett.*, **42(5)**, 460, (1983)

[14] S. Nishino, Y. Hazuki, H. Matsunami and T. Tanaka, *J. Electrochem. Soc.*, **127**, 2674, (1980)

[15] Data provided by CREE Research, Inc., Durham, North Carolina

[16] A. Suzuki, H. Matsunami and T. Tanaka, *J. Electrochem Soc.*, **125(11)**, 1896, (1978)

[17] J. Costello and R. Tressler, *J. Amer. Ceram. Soc.*, **69(9)**, 674, (1986)

[18] A. Suzuki, H. Ashida, N. Furui, K. Mameno and H. Matsunami, *Jap. J. of Appl. Phys.*, **21(4)**, 579, (1982)

[19] W. Von Münch and I. Pfaffender, *J. Electrochem. Soc.*, **122(5)**, 642, (1975)

[20] W. Moore, Basic Physical Chemistry, Prentice-Hall, Inc., (Englewood Cliffs, New Jersey, 1983), p. 16

[21] J. Moore, C. Davis and M. Coplan, *Building Scientific Apparatus*, Addison-Wesley Publishing Company, (London, Amsterdam, Ontario, Sydney, Tokyo, 1983), p. 72

[22] C. Kittel, op. cit., p. 536

[23] G.A. Somorjai, *Chemistry in Two Dimensions: Surfaces*, Cornell University Press, (Ithaca and London), p. 72

[24] ibid., p.41

[25] C. Wagner, W. Riggs, L. Davis and J. Moulder, *Handbook of X-Ray Photoelectron Spectroscopy*, (Perkin-Elmer Corp., Physical Electronics Div., Eden Prairie, MN, 1979), p. 4

[26] ibid., p. 52

[27] B. Jørgensen and P. Morgan, *J. Vac. Sci. Technol. A* **4(3)** 1701

(1986)

[28] R. Kaplan, T. Parrill, *Surface Sci. Lett.*, **165**, L45, (1986)

[29] K. Brack, *J. Appl. Phys.*, **36(11)**, 3560, (1965)

[30] Harris and Call in *Silicon Carbide 1973*, edited by R. Marshall, J. Faust, Jr.,and C. Ryan (Univ. of South Carolina Press, Columbia, 1974), p.329

[31] L. Muehlhoff, M. J. Bozack, W. J. Choyke, J. Yates, Jr., *J. Appl. Phys.*, **60(7)**, 2558, (1986)

[32] R. Kaplan, *Surface Sci.*, **215**, 111, (1989)

[33] J. Drowart, G. De Mani, M. Inghram, *J. Chem. Phys.*, **29(5)**, 1015, (1958)

[34] C. Carosella, J. Comas, *Surface Sci.*, **15**, 303, (1969)

[35] X. Zheng, P. Cao, *Surface Sci. Lett.*, **219**, L543, (1989)

[36] V. Bermudez, *J. Appl. Phys.*, **66(12)**, 6084, (1989)

[37] Fitzer and Ebi in *Silicon Carbide 1973*, edited by R. Marshall, J. Faust, Jr., and C. Ryan (Univ. of South Carolina Press, Columbia, 1974) p.320

[38] S. Miyagawa, Y. Ato, Y. Miyagawa, *J. Appl. Phys.*, **53(12)**, 8697, (1982)

[39] A. Van Bommel, J. Crombeen, A. Van Tooren, *Surface Sci.*, **48**, 463, (1975)

[40] B. Pate, M. Oshima, J. Silberman, G. Rossi, I. Lindau, W. Spicer, J. *Vac. Sci. Technol. A*, **2(2)**, 957, (1984)

[41] A.G. Acheson, British Patent No. 17911, (1892)

[42] J. Lely, *Ber. dtsch. keram. Ges.*, **32**, 229, (1955)

[43] A. Addamiano and P.H. Klein, *J. Cryst. Growth*, **70**, 291, (1984)

[44] J.I. Federer, *Thin Solid Films*, **60**, 89, 1977

[45] H.S. Kong, J.T. Glass and R.F. Davis, *J. Appl. Phys.*, **64(5)**, 2672, (1988)

[46] C.D. Stinespring and J.C. Wormhoudt, *J. Appl. Phys.*, **65(4)**, 1733, (1989)

[47] Y. Catherine, A. Zamouche, J. Bullot and M. Gauthier, *Thin Solid Films*, **109**, 145, (1983)

[48] A. Raveh, A. Inspektor, U. Carmi and R. Avni, *J. Vac. Sci. Technol. A*, **5**, 2836, (1987)

[49] H. Wieder, M. Cardona and C.R. Guarnieri, *Phys. Stat. Sol. B*, **92**, 99 (1979)

[50] S. Hara, W.F.J. Slijkerman, J.F. van der Veen, I. Ohdomari, S. Misawa, E. Sakuma and S. Yoshida, *Surface Sci. Lett.* **231**: 196 (1990)

[51] M.A. Van Hove, W.H. Weinberg and C. Chan, *Low-Energy Electron Diffraction*, Springer Series in Surf. Sci., Vol. 6, (Springer, Berlin, Heidelberg, New York, 1986)

[52] J. Pendry, *J. Phys. C*, 13, 937, (1980)

[53] J.A. Powell, L.G. Matus and M.A. Kuczmarski, *J. Electrochem Soc.* **134**, 1558 (1987)

[54] C.S. Chang, N.J. Zheng, I. Tsong, Y.C. Wang and R.F. Davis, *J. Am. Ceram. Soc.*, **73**(11) 3264 (1990)

[55] M. Dayan, *J. Vac. Sci. Technol. A* **3(2)**, 361 (1985)

[56] P.J. Rous, M.A. Van Hove and G.A. Somorjai, *Surface Sci.*, **226**:15, (1990)

[57] M.A. Van Hove and S.Y. Tong, *Surface Crystallography by LEED*, Springer Ser. Chem. Phys., Vol. 2 (Springer, Berlin, Heidelberg 1979)

[58] P.J. Rous, D. Jentz, D.J. Kelly, R.Q. Hwang, M.A. Van Hove and G.A. Somorjai, in *The Structure of Surfaces-III, Proc. ICSOS-III*, Eds. S.Y. Tong, M.A. Van Hove, K. Takayanagi and X.D. Xie, Springer-Verlag (Berlin, Heidelberg, New York) 1991, In press

[59] A. Wander, M.A. Van Hove and G.A. Somorjai, (Submitted to *Phys. Rev. Letters*, May 1991)

[60] J. Yoshinobu, H. Tsuda, M. Onchi, and M. Nishijima, *J. Chem. Phys.* **87(12)** 7332 (1987)

[61] B.W. Holland, C.B. Duke and A. Paton, *Surface Sci.* **140**: L269 (1984)

[62] P. Badziag (Submitted to *Phys. Rev. B*, Feb. 1991))

[63] V.M. Bermudez and R. Kaplan (Submitted to *Phys. Rev. B*, Feb. 1991)

[64] S. Kevan, *Phys. Rev. B*, **32**, 2344, (1985)

[65] T. Tabata, T. Aruga and Y. Murata, *Surface Sci.*, **179**, L63, (1987)

[66] B. Craig and P. Smith, *Surface Sci.*, **233**, 255, (1990)

LAWRENCE BERKELEY LABORATORY
UNIVERSITY OF CALIFORNIA
INFORMATION RESOURCES DEPARTMENT
BERKELEY, CALIFORNIA 94720